The Pennsylvania State University

The Graduate School

EXPERIMENTAL SCALING OF HOVERING ROTORCRAFT

AERODYNAMICS IN HYPERBARIC CONDITIONS

A Thesis in

Aerospace Engineering

by

Constantinos Stephanos Kandias

Submitted in Partial Fulfillment

of the Requirements

for the Degree of

Master of Science

August 2023

The thesis of Constantinos Stephanos Kandias was reviewed and approved by the following:

Mark A. Miller
Assistant Professor of Aerospace Engineering
Thesis Advisor

Eric Greenwood
Assistant Professor of Aerospace Engineering

Sven Schmitz
Professor of Aerospace Engineering
Boeing/A. D. Welliver Professor

Amy R. Pritchett
Professor of Aerospace Engineering
Department Head of Aerospace Engineering

Abstract

An experimental study was conducted to characterize the performance of a $1/8^{\text{th}}$ scale model of an Urban Air Mobility style rotor in hover over a range of Reynolds numbers and Mach numbers. The Reynolds number and Mach number could be varied individually through the use of compressed-air as a testing medium, allowing for precise control of the ambient density. Thrust and power coefficients were measured for a range of Reynolds numbers from approximately 2×10^5 to 6×10^5, and Mach numbers from 0.125 to 0.25. The ability to control Reynolds number separate from Mach number provides a mechanism to counteract the scaling effects which take place as a scale-model of a rotor is brought down in size to facilitate cost-effective experimental testing. Without altering the fluid properties in some way to account for this scale effect, the Reynolds and Mach numbers cannot both be matched simultaneously to the values that would be experienced at full-scale. This presents an issue as rotor performance characteristics such as the thrust and power coefficients are known to be dependent on both the Reynolds number and Mach number. By controlling the density and therefore the Reynolds number, the effective scale of the rotor model can be changed at will up to or even beyond the full-scale geometry of the rotor system of interest.

The results characterize the variation in rotor thrust and power as the effective scale increases from that of the model to the full-scale vehicle. Over the range of conditions tested, the thrust coefficient was found to increase by 1.7% for an increase in Reynolds number of 1×10^5, and the power coefficient by 0.85% per 1×10^5 increase in Reynolds number. In the process of scaling down a large rotor system to $1/8^{\text{th}}$ or less of its original scale for use in a low-cost experimental study, differences in Reynolds number on the rotor blades can be on the order of millions. This can result in unacceptably high deviations in performance between the model- and full-scale.

The use of compressed-air as a testing medium for rotorcraft performance experiments is a novel technique which can facilitate studies at a greatly reduced cost, and allow for much more rapid and thorough experimentation than was previously possible. By potentially reducing the scale of an entire rotary-wing aircraft by an order of magnitude or more, an experiment can be designed similarly to that which would be suitable for a typical small-scale wind tunnel. This can both reduce the dependence on large wind tunnel facilities capable of accommodating a full-scale vehicle and opens up the opportunity for experiments on a much lower budget than would previously have been possible.

Table of Contents

List of Figures

List of Tables

Nomenclature

List of Symbols

A Rotor disk area

a Sonic velocity

B Coefficients of real gas compressibility model

C_d Drag coefficient

C_l Lift coefficient

C_P Power coefficient

C_p Pressure coefficient

C_T Thrust coefficient

C_T/σ Blade Loading Coefficient

FM Figure of Merit

F_z Force in the Z direction, total rotor thrust

M Mach number

M_z Moment about the Z axis, motor shaft torque

N_b Blade number

P Total rotor power

p Static pressure

R Rotor radius

Re Reynolds number

R_u Universal gas constant

T Temperature

t Time

U Velocity

u_x Uncertainty of a measured value x

x_i Measured value used to calculate a quantity Y

Y Quantity subject to uncertainty analysis

Z Real gas compressibility factor

α Local blade element angle of attack

α_{tpp} Rotor disk tip path plane angle of attack

θ Local blade element pitch angle

θ_i Sensitivity of a calculated value to the uncertainty of a constituent measurement

μ Dynamic viscosity

μ_∞ Advance ratio

ρ Ambient air density

ϕ Local blade element inflow angle

ω Rotor angular speed

List of Abbreviations

BET   Blade Element Theory

BOS   Background-Oriented Schlieren

BVI   Blade-Vortex Interaction

CATS   Coaxial Acoustics Test System

CAWT   Compressed Air Wind Tunnel

DAQ   Data Acquisition Device

ESC   Electronic Speed Controller

eVTOL   Electric Vertical Takeoff and Landing

IEC	International Electromechanical Commission
LSB	Laminar Separation Bubble
PARTS-I	Pressurized-Air Rotor Testing System
PIV	Particle Image Velocimetry
PWM	Pulse Width Modulation
RTD	Resistance Temperature Detector
UAM	Urban Air Mobility
VTOL	Vertical Takeoff and Landing

Acknowledgments

Chapter 1 |
Introduction

This thesis outlines the aerodynamic behavior of a hovering rotor, operating in air at a range of ambient densities. The goal in this work is to demonstrate changes in a rotor's performance as the effective scale of the rotor varies, and the ability to replicate the aerodynamic conditions of a range of scales by adjusting the density of the air in which the rotor is operating. Experimental testing of a rotor in a compressed air environment is a novel area of study, for which little existing data is available. The main motivation behind this work is to make experimental studies of rotorcraft performance more practical, and cost effective. Small-scale models have been used for this purpose for decades, but there are limitations on how small the models can be made, as will be discussed later in this chapter [1–4]. Past studies have used alternate gasses to replicate conditions on a larger scale rotor system to achieve a similar increase in scale, but the use of compressed-air offers an attractive alternative for a number of reasons [5,6]. Before discussing the merits of testing rotors in compressed-air, a brief overview of rotary-wing aerodynamics will be presented to contextualize the present study, including a summary of experimental, analytical, and computational methods.

The aerodynamics of rotating wings is a complex subject which has been of interest to mankind for centuries; as early as the 15$^{\text{th}}$ century, Leonardo DaVinci theorized a device with rotating aerodynamic surfaces which could carry a person up to the skies was possible, though it wasn't until August of 1907 when two rotary-wing vehicle concepts, Louis Bréguet's Gyroplane and Paul Cornu's tandem rotor helicopter, made their first attempts at getting off the ground, albeit limited to brief hops rather than proper flight [7]. Great advancements have been made since then, including a wealth of information on theoretical analysis of rotorcraft performance, both from a design and analysis perspective. Many of the early analytical methods for rotor aerodynamics were adapted from those developed for propellers [8]. The simplest such method is one-dimensional actuator-disk

based momentum theory, which reduces the physical behavior of a rotor to a simple control-volume analysis on the streamtube of air associated with the rotor, modelling the rotor itself as an infinitely thin discontinuity across which a pressure differential can be imposed [9, 10]. To examine in more detail the design of the rotor system, Froude developed the Blade Element Theory (BET), which discretized a propeller into a series of spanwise elements, which could be analyzed individually [9–11].

BET allows the performance of a given rotor to be analyzed, but it lacks some elements, namely a method for predicting the inflow induced by the rotor, which is critical to obtaining an accurate result. The simple momentum theory can provide predictions of the inflow, with accuracy that is satisfactory in for many preliminary design purposes [8]. The combined use of BET with momentum theory to calculate the inflow distribution is referred to as Blade Element Momentum Theory and is commonly used for low to moderate fidelity performance predictions [9]. More sophisticated models to predict the inflow of a rotor have been developed, such as that by Mangler and Squire, which is designed to be applicable to helicopter rotors in forward-flight [12]. Such models are often restricted to a subset of a vehicle's operating envelope due to their inherent assumptions about the form of the inflow solution which may not be applicable in general. Higher fidelity still can be achieved by accounting for the effects of the rotor wake on the inflow distribution, as the induced inflow can be correlated to the action of the vorticity in the wake, by means of the Biot-Savart law [8]. Such a procedure has been made possible and increasingly attractive in recent decades by advancements in computational technology. Increased computing power and the availability of supercomputing infrastructure has allowed for great advances in this front. A simple BET solver coupled with an inflow model based on momentum theory can provide details of the performance of a rotor in seconds. Incorporating a higher-fidelity wake model improves the accuracy of the results, at the expense of more computational effort [13].

Despite all the advancements in both analytical and numerical methods, there are still a number of drawbacks. Any model will inherently contain some degree of approximation for the sake of simplicity or feasibility. A more simplified model may be quicker and less expensive to use in practice, but will provide less accurate results. A higher-fidelity model may provide the desired accuracy, but at a cost which may be on the same order, or even higher, than an equivalent experiment. Experimental studies can provide insight into the physics at play that an analytical or numerical model simply cannot, as knowledge of the relevant physics is a precondition for choosing an appropriate model. In addition, as new aerodynamic models are developed with ever-increasing complexity and fidelity,

experimental data will be necessary to validate these models, and outline the conditions to which they are applicable, and areas where they may struggle.

1.1 Rotary-Wing Aircraft

Rotorcraft exist in a variety of configurations beyond the traditional single-rotor helicopter. The earliest prototypes of rotorcraft were multicopters, with several rotors in tandem [7]. There has also been considerable development of other configurations including coaxial helicopters and tiltrotors [10]. A recent boom in the Urban Air Mobility (UAM) industry has led to the development of a variety of new vehicle concepts with Vertical Takeoff and Landing (VTOL) capability. While all these vehicle types share the common feature of one or more rotors, the specifics of their designs, operating conditions, and control mechanisms can vary greatly. A brief overview of some of these vehicle types will be presented here, along with any key qualities which may influence the aerodynamic behavior and the design of an experiment intended to accurately replicate such behavior.

1.1.1 Helicopters

The classic example of an aerial vehicle with rotating wings is the single-rotor helicopter. With the first production vehicle being the Sikorsky R-4 in 1942, it is the category of rotorcraft which has become most ubiquitous, and is the most well-developed, surpassing the popularity and utility of earlier vehicle concepts such as the autogyro [14]. It consists of a main rotor, which produces the lift necessary to keep the vehicle in the air as well as control forces in the forward and lateral directions, and pitch and roll moments by means of the collective and cyclic pitch control and blade flapping motion [9]. The main rotor also produces a torque, or yaw moment, which must be balanced by the tail rotor. This smaller tail rotor produces sideways thrust which results in a counter-torque, and provides a mechanism for the pilot to control the yawing motion of the vehicle.

1.1.2 Urban Air Mobility Vehicles

Many different UAM vehicle concepts are currently being developed. The common element of such vehicles lies not in their design, but in their end use: aerial transportation of passengers in urban environments. Many of these vehicles make use of rotors, typically due to the desire for VTOL capability. While not a defining characteristic, another common trait in the UAM industry is the use of a distributed electric powertrain, with

vehicles incorporating this type of mechanism being referred to as Electric Vertical Takeoff and Landing (eVTOL) aircraft. While rotors are a common feature in UAM aircraft, the function, and operational range of those rotors can vary considerably. Some such configurations are the traditional helicopter, multicopter, tiltrotor, tiltwing, and Lift+Cruise [15–19]. The collection of design concepts has resulted from the culmination of industry efforts by various companies developing their own vehicles and proprietary technology, and conceptual studies by academic and research institutions examining the feasibility of some such designs, and their potential use cases [19].

Multicopter aircraft are perhaps the simplest of the multirotor vehicle configurations, incorporating a number of rotors distributed around the fuselage of the aircraft, oriented such that their rotor planes remains nominally horizontal during flight. The rotors will typically have individual rotational speed, and possibly collective pitch control. In contrast to a helicopter, cyclic pitch control is not implemented, as the degrees of freedom required for adequate control authority can be obtained by means of varying only the thrust and torque produced by the individual rotors [17].

When multiple rotors are operating in close proximity to each other, there is ample opportunity for interactional aerodynamic effects to occur. Under certain flight conditions, the wake of one rotor may pass into the inflow of another, having a direct effect on its aerodynamic performance. Even if no rotor directly ingests the wake of another, there can still be influence on the inflow conditions [20]. The spacing between the rotors, as well as the details of the flight condition can strongly affect the nature of these effect, which make them difficult to model. One such example of a flight condition which results in unique aerodynamic interactions is ground-effect; as the wake produced by one rotor collides with that of an adjacent rotor near the ground, it results in different recirculation and upwash behavior than those seen by an isolated rotor, which can affect the resulting performance benefit known to occur for rotorcraft in ground-effect conditions [21].

Tiltrotor aircraft are a conceptual hybrid between the aforementioned multicopter vehicles and a traditional fixed-wing aircraft. A tiltrotor contains multiple rotors distributed around the airframe, much like a multicopter, with the added ability to tilt the entire rotor, to change the direction of the thrust force it produces. Tiltrotors also incorporate wings, which are used to produce lift while the vehicle is in a forward-flight configuration. Tiltrotors will often use their rotors to takeoff and land vertically as a multicopter would, before tilting the rotors forward mid-air into a propeller like configuration. This effectively allows the aircraft to achieve greater efficiency and range than a typical rotorcraft, while also retaining VTOL capabilities. Aerodynamically speaking,

4

tiltwing aircraft are similar to the tiltrotor concept. Though there are some mechanical differences which may impact the operation of the vehicle, there is much overlap in the configuration and behavior of the rotors. For the key flight conditions of interest, such as forward flight, and hover, many of the same interactional effects will be observed. The main difference will be how the wake of the rotor interacts with the wings, and fuselage.

In the forward-flight configuration, a tiltrotor is not unlike a propeller driven, fixed-wing aircraft, though typically with larger rotors, and often more of them. In the hover configuration a tiltrotor more closely resembles a mluticopter vehicle and much of the previous discussion on interactional effects also applies. In addition, recent work has demonstrated variations in ground-effect performance of a tiltrotor due to interactions between the downwash and nearby obstacles representative of a vehicle approaching a ship for landing [22]. A major part of the proposed use of many eVTOL concepts involves takeoff and landing in urban environments, where there may be the potential for similar obstacle interaction effects.

Lift+Cruise vehicles combine multiple lifting rotors, as in a multicopter vehicle, with one or more rotors dedicated to propulsion and wings to generate lift in forward flight. When hovering or using only the lifting rotors such vehicles are similar in configuration to a multicopter. During forward flight, Lift+Cruise vehicles will typically shut down their lifting rotors, orient them in a minimum-drag position, and fly like a fixed-wing aircraft [23]. During transition between hover and forward-flight, both the lifting and propulsive rotors are active and there is maximum potential for complicated interactional aerodynamic effects. The lifting and propulsive rotors are oriented perpendicularly to each other which increases the odds of one ingesting the wake of the other, or the wakes of the two interacting in complex ways depending on the specifics of the vehicle configuration.

All of the multirotor UAM concepts illustrated here have the potential for complex interactional effects, meaning the performance of all the rotors cannot be represented as the sum of multiple isolated rotors. An experimental test campaign which hopes to characterize the performance of any of these vehicle concepts needs to include multiple rotors and potentially other bodies such as a wing or fuselage. With regard to the design of an experimental model this means increased complexity, cost, and size, and the need for a facility which can accommodate such a test. With the recent increase in research and development in UAM vehicle technology the need for small-scale aerodynamic testing which can accurately replicate full-scale vehicle physics is greater than ever before.

1.2 Experimental Methods for Studying Rotorcraft Performance

Past experimental studies of rotorcraft performance have employed a variety of methods and test configurations in order to achieve a common goal: acquiring data describing the physical behavior of a rotary wing aerodynamic system which is representative of the real-world operating conditions of a vehicle. Such methods include full-scale tests either in a wind tunnel, whirl-tower, or a flight test or experiments using small-scale models in either atmospheric air or an alternate gas. The benefits and drawbacks of the aforementioned methods will be briefly examined along with some historical examples of their use, and the benefits and drawbacks of each. Ultimately there is no single testing method that can serve all purposes. Many studies, including some referenced in this work, involve a combination of flight tests, full-scale, and small-scale experiments [24–27].

1.2.1 Full-Scale Experimental Studies

The most direct way to obtain performance data for a rotor is to conduct a full-scale experiment. This can include flight testing of a vehicle, or testing in facilities such as wind tunnels, or whirl towers, which can replicate certain aerodynamic conditions the vehicle may experience in flight, while allowing for a greater degree of repeatability, and the potential for more instrumentation. Wind tunnel testing also avoids some of the risk associated with flight tests [25]; the possibility of a crash is eliminated by testing the prototype in a facility on the ground, which can allow for more rapid experimentation of new design concepts and technologies, which may not have a sufficient safety record to justify a flight test.

The testing of models in a more controlled environment also better facilitates the use of certain measurement or visualization techniques, including Background-Oriented Schlieren (BOS) [28], which is particularly useful in rotorcraft applications for visualizing blade tip vortices, as they are generated by the rotor. Although BOS is not used in the present study, it serves as a useful case study which outlines some of the benefits of wind tunnel testing. BOS typically involves the use of a fixed background image, allowing estimation of density gradients in a flowfield by measuring the refraction of the background image. The use of a fixed model in wind tunnel or similar facility simplifies the process, but testing can be done in more open environments on a vehicle in flight [29]. Reference-free BOS can allow for similar measurements without a static background,

6

extending this technique into the regime of flight testing, but not without caveats. The feasibility of the technique relies on the natural environment providing a background image of sufficient quality, an issue which can be avoided by testing with a specially designed background image in a dedicated facility [30]. Reference-free BOS requires careful planning of the flight trajectory and maneuvers, in order to ensure that suitable terrain will be positioned in the background of the image to facilitate the technique, which can somewhat limit the conditions for which data can be collected. In a wind tunnel, the camera position and background image can be tailored to the specific experiment, to more effectively image the phenomena of interest.

BOS has enabled detailed studies of rotor wakes, by providing a technique to track the motion and behavior of tip vortices [28–31]. Studies have used BOS along with Particle Image Velocimetry (PIV) to quantify the behavior of the wake in response to varying rotor operating conditions; in particular that the trajectory and behavior of the tip vortices in a rotor wake are highly dependent on the blade pitch, and consequently the lift produced by the blade [32]. BOS and PIV have also been used to quantify vortex behavior in situations where the rotor is in ground effect, where the impingement of the wake on the ground can strongly affect a rotor's performance [21, 29, 31]. Measurements on a BO-105 helicopter in ground effect displayed vortex pairing behavior which affected the trajectory of the tip vortices, and that vortex dynamics and perturbations leading to disintegration were affected by the flight condition [31]. In particular, a landing approach resulted in decreased vortex convection velocities, and an enhancement of perturbations [31].

More broadly, data of interest from an experimental study can include visualization of the behavior of the wake including the vortex structure and potential interactional effects, quantitative measurements of loads observed on a rotor or airframe, quantification of the inflow distribution along the rotor plane, and measurements of of the velocity field in the rotor wake [13]. Much of this data is more readily obtained in a wind tunnel than a flight test, due to the complexities associated with certain instrumentation techniques such as laser Doppler velocimetry, hot wire anemometer probes, as well as the aforementioned BOS and PIV.

1.2.2 Small-Scale Experimental Models

The use of small-scale experimental models in place of a full-scale vehicle or rotor system also comes with a unique set of benefits and drawbacks; the reduced scale can decrease the cost of an experiment dramatically, at the expense of deviation from the operating

conditions of the system of interest. One of the major drawbacks of full-scale experimental testing is the cost of such a campaign, driven by the sheer scale of rotorcraft systems. Few facilities exist that can are large enough to accommodate a full-scale helicopter or UAM vehicle, and which are capable of providing a gamut of operating conditions including hover and forward flight. Such large-scale wind tunnel facilities come at a greater operating cost than a smaller facility, due to staffing and operating costs, as well as the power required to run the necessary equipment. Larger experimental models are also more expensive to fabricate than a reduced-scale model, adding further to the cost of an experiment. In addition, smaller models tend to produce loads of lesser magnitude, which can reduce the requirements of instrumentation equipment.

With a reduced cost of experimentation, the use of small-scale models can facilitate more in-depth and rapid studies, involving a more iterative process, and a wider design space and test matrix. When used during the design of a new vehicle, this allows experimentation to occur earlier, and more frequently in the development cycle, providing more concrete data to justify design decisions. When used in a more academic or research-oriented context, such cost savings can enable more thorough studies, or even allow a study to be possible at all, particularly when budgets may be limited. Work to develop scaled rotor models for use in wind tunnels, and to translate the results to the equivalent full-scale geometry has already been an active area of research [1, 5, 26]. Such efforts have involved a variety of methods, including altering the rotor geometry or structural properties, or controlling the properties of the working fluid the rotor is operating in, as will be discussed in more detail in § 1.5.

Another notable example of a small-scale rotorcraft experiment is the HART test, which examined the use of higher-harmonic control on the cyclic pitch of helicopter rotors, the impacts on the vortices in the wake, and the resulting noise produced by the rotor [2]. Years later, the HART II test was conducted as a follow up involving more detailed wake measurements using stereoscopic Particle Image Velocimetry (PIV), in order to provide additional data about the rotor wake and vortex behavior, among other improvements [3]. Both HART and HART II made use of a 40% geometrically scale model of the BO-105 helicopter rotor, which was dynamically scaled as well [2, 3]. The 40% relative scale is a reduction relative to the full-scale rotor, although it is not as dramatic a difference as the experiments discussed in this thesis. Greater differences in scale will bring about larger deviations from full-scale vehicle performance; conversely, the closer the model is to the full-scale geometry, the better it will represent the relevant aerodynamic phenomena.

Experiments have also been conducted on rotors or propellers for which the full-scale

size is much smaller than a typical aircraft. Examples of such small-scale vehicles include small unmanned aerial vehicles, micro aerial vehicles and remote-controlled aircraft which can have rotor diameters of 0.2 m or less [33]. The Reynolds numbers typically achieved on these vehicles can be less than 1.0×10^5. A study investigating the performance of rotors on this scale determined that increases in Reynolds for this operational regime number typically result in increases in thrust coefficient, and decreases in the power coefficient [33]. In this study, the Reynolds number was varied by changing the scale of the models used, from 5.7 cm to 23 cm in diameter.

1.3 Comparisons Between Full- and Small-Scale Rotor Performance

A number of studies have directly compared performance data from a full-scale test to that of a small-scale model, and evaluated the ability to predict a vehicle's performance using a small-scale model. One such study examined the performance of two rotor designs; the Boeing CH-47D, and YUH-61A [26]. The CH-47D model was a dynamically-scaled model, $1/6^{th}$ of the full rotor scale. In hover, the small-scale rotor saw an increase in power coefficient, when operating at the same thrust coefficient as the full-scale rotor. This was attributed to profile power effects, resulting from the Reynolds number being $1/6^{th}$ of that on the full-scale rotor, when operating at the same tip-Mach number [26]. The same study also examined the YUH-61A rotor at full, and $1/5^{th}$ scale, also using a dynamically-scaled model. One of the key differences in the design of the YUH-61A rotor over that of the CH-47D is the tapering of the blade chord near the tips. Rotors with tapered and untapered tips were tested at full-scale, and $1/5^{th}$ scale. This tapering led to further decreases in the Reynolds number near the blade tips, causing the model-scale blades to stall near the tips at much lower thrust coefficients than the full-scale rotor [26]. While the full-scale rotor also would have experienced a reduction in tip Reynolds number over an untapered rotor, the Reynolds numbers observed in the typical operating range of the rotor remained high enough to avoid any performance penalty. The figure of merit is a common performance metric for a helicopter which represents the ratio of power required to hover according to momentum theory P_{ideal}, to the power required by a real rotor P_{actual}, as defined in Eqn. 1.1. At full-scale, the tapered rotor maintained a greater figure of merit than the untapered rotor over the entire range of thrust coefficients tested. The small-scale tapered rotor also displayed an increased figure of merit over the

untapered rotor for low thrust coefficients. However, for higher thrust coefficients, the figure of merit of the tapered rotor eventually became worse than that of the untapered rotor, an effect which was attributed to stall near the blade tips [26].

$$FM = \frac{P_{ideal}}{P_{actual}} \tag{1.1}$$

Another study, involving a helicopter rotor developed by Sikorsky with swept and tapered geometry near the tips, drew similar conclusions on the variation of performance with scale. The study compared a full-scale rotor system to a $1/5^{th}$ scale model. The results indicate an overall increase in power consumption by up to 20% in the small-scale rotor, which was attributed to Reynolds number effects on the profile drag [27].

The HART and HART-II studies focused on the ability to reduce noise and vibration through the use of higher-harmonic control, but also provided data for a baseline case without any higher-harmonic control and include a variety of aerodynamic data, including PIV measurements of the tip vortices in the wake [2,3,34]. Later studies have compared their results to the datasets and examined the feasibility of predicting full-scale acoustic data using a small-scale model, including one which used a computational model of a full-scale rotor. The results showed good agreement between the datasets [34]. The main data of interest are the Blade-Vortex Interaction (BVI) events, and the acoustic emissions resulting from them. There were differences observed in the amplitude of the pressure spikes resulting from BVI events, as well as the azimuthal location where the events occurred, which were attributed to slight differences in trim between the small- and full-scale rotors [34]. The noise measured at the specified observer locations differed at most by 2 dB, which represents a good match between the aeroacoustic behavior [34]. This indicates that good agreement in the acoustic emissions can be achieved between a full-scale helicopter rotor, and a 40% scale model, implying the scaling effects are not yet strong enough to cause significant deviations in the aerodynamic behavior, and resulting acoustics.

In addition to acoustics, the vortices in the wake play an important role in the aerodynamics of the rotor by influencing the inflow and loading distribution along the rotor blades. A study comparing experimental measurements to the results of computational performance prediction using the lifting-surface method found thrust was over predicted by 20% when using a prescribed wake model, but accuracy was improved to within 5% when incorporating wake geometry from experimental measurements [35].

Measurements of the wakes produced by small-scale rotors have shown key differences in the wake vortex dynamics, particularly much greater stability at longer wake ages. In

a study using a model helicopter in ground effect operating at tip Reynolds numbers of 2.8×10^5, tip vortices were detected at wake ages up to 1260° [36]. A follow up study involving BOS and PIV measurements on a full-scale BO-105 helicopter operating at tip Reynolds numbers on the order of 4×10^6 was only able to detect tip vortices at wake ages of up to 630°. Although the rotor geometry is not identical between the two studies, both rotors have rectangular tips and operated at the same thrust coefficient of 0.0094, as defined in Eqn. 1.2. The thrust coefficient, defined in terms of the thrust F_z, air density ρ, rotational speed ω, rotor disk area A and radius R is a commonly used dimensionless metric for rotor performance, which will be used for later analysis in this study [1]. The analogous power coefficient, defined in terms of the rotor power P rather than thrust, is also defined in Eqn. 1.3. The thrust coefficient of a rotor has been shown to be an important factor that influences the wake geometry [37].

$$C_T = \frac{F_z}{\rho A \omega^2 R^2} \tag{1.2}$$

$$C_P = \frac{P}{\rho A \omega^3 R^3} \tag{1.3}$$

1.4 Comparisons Between Full- and Small-Scale Rotor Acoustics

BVI is a phenomenon which presents both aerodynamic and acoustic issues, and has therefore been studied in much detail. The specifics of a BVI event are highly dependent on the aerodynamic behavior of a rotor, and the vortices in its wake. Two of the important parameters influencing the occurrence of BVI events are the advance ratio, and the descent rate of the helicopter. The advance ratio is defined in Eqn. 1.4 in terms of the forward speed of the helicopter U_∞, and the tip-path plane angle of attack α_{tpp}.

$$\mu_\infty = \frac{U_\infty cos(\alpha)}{\omega R} \tag{1.4}$$

Data are available comparing the BVI noise from a $1/7^{\text{th}}$ scale model of an AH-1 helicopter rotor to a flight test of a full-scale rotor [38]. The study examined the characteristics of BVI noise on the rotor for varying advance ratios, and rates of descent. Good agreement was achieved for advance ratios of less than 0.224, but at greater advance ratios, more significant differences were seen in the widths, and amplitudes of the BVI

pulses [38]. The widths of the BVI pulses in the full-scale data tend to be shorter than in the small-scale data; this indicates the tip vortices shed from the full-scale rotor are smaller in diameter than those from the small-scale rotor [38]. The $1/7^{\text{th}}$ scale rotor therefore does not perfectly replicate the flow physics in the full-scale, though it exhibits similar behavior over part of its operating envelope.

1.5 Practical Considerations for Scale-Model Rotor Testing

While the use of small-scale models for experimental investigation of rotorcraft presents a number of attractive benefits, care must be taken in designing the experiment, and analysing the results to ensure meaningful correlations can be drawn between the experiments and the full-scale system. Due to the difference in scale, the raw performance measurements will obviously not correlate one-to-one, though with proper post-processing of the data, meaningful insights can be extracted. The most simple method is to focus the analysis on trends in the results with variations in the design or operating conditions, ignoring the absolute performance values. If the performance of the full-scale rotor system is known for a given operating condition, it can be assumed with some caution that incremental changes in performance in a small-scale model due to a change in the design or operating point will translate to the full-scale geometry [26]. Thus an incremental improvement in performance of a small-scale model for a given design change will likely result in a similar improvement in the full-scale vehicle, though the relative magnitude of the improvement may not be the same.

Although the absolute performance data will not agree, more detailed analysis of the data can provide insight into the absolute performance of a full-scale system based on the data from a small-scale experiment, provided all the relevant physics are replicated in the small-scale model. Concepts such as dynamic similarity and scaling laws allow an experimentalist to ensure their models accurately reflect the physics of the full-scale system of interest, and provide a way to correlate results obtained from small-scale models to the behavior of a larger system [1, 26, 39, 40]. Dimensionless parameters such as the Reynolds number allow quantification of the physical regime an aerodynamic system is operating in without dependence on any one specific parameter; so long as the dimensionless parameters relevant to a phenomenon are sufficiently similar to the system of interest, the principles of dynamic similarity state that behavior will be accurately

replicated in a geometrically similar model with different physical properties [1, 40]. Parameters of interest for rotorcraft applications include the Reynolds number, which is important for phenomena which are dependent on viscosity and turbulence, and the Mach number, which is an indicator of flow-related compressibility effects [1, 40]. The Reynolds number of an airfoil is defined in Eqn. 1.5 in terms of the relative velocity U, chord length c, air density ρ and dynamic viscosity μ. The Mach number is defined in Eqn. 1.6 in terms of the relative flow velocity U and sonic velocity a.

$$Re = \frac{\rho U c}{\mu} \tag{1.5}$$

$$M = \frac{U}{a} \tag{1.6}$$

While a Reynolds number could be defined at any point along the span of the rotor blades, one of two conventions are typically used, depending on the rotor geometry. For rotor blades without a substantial amount of taper, the nominal Reynolds number is usually defined by the parameters at the tip of the blade, as this results in the largest value. For rotors which taper down to a smaller chord length at the tip, the 75% radial station is typically used. The Mach number is always defined at the blade tip, as this results in the largest value. Other parameters may be relevant as well, such as the Lock number which is associated with aeroelastic effects [1, 26]. Aeroelasticity will be neglected for the purposes of this study, which focuses solely on aerodynamic effects on a rotor that is assumed to be rigid.

For a small-scale rotor, matching both Reynolds and Mach numbers exactly to the full-scale geometry is normally impossible. By combining Eqn. 1.6 and Eqn. 1.5, Eqn. 1.7 can be obtained which outlines the coupling of the Reynolds number, Mach number, and rotor scale, represented here by the chord length c.

$$Re = M \left(\frac{\rho a}{\mu} \right) c \tag{1.7}$$

As the scale of the rotor decreases, the Reynolds and Mach numbers necessarily deviate from their full-scale values. If one is held constant, for example by adjusting the rotational speed, the other cannot also remain constant. For less severe reductions in rotor scale such that the Reynolds and Mach numbers can be kept close to their full-scale values, the difference may be acceptable. For greater reductions in scale, the difference can become large enough to cause unacceptable deviations in performance, as will be discussed in the results presented in chapter 4.

The thrust and power coefficients are dimensionless values which are commonly used to characterize the performance of a rotor. They serve as metrics of a rotor's performance which are independent of any dimensional parameter of the rotor. The numerical values of C_T and C_P should remain constant with variations in any of their constituent variables so long as the aerodynamic conditions remain similar. The overall aerodynamic state of a rotor can be generally quantified by the Reynolds number and tip Mach number, though other factors such as aeroelasticity may play a role depending on the details of the rotor in question. If the thrust coefficient remains constant for variations in the rotational speed ω, then from Eqn. 1.2 it can be easily deduced that the thrust F_z produced by the rotor must increase quadratically with rotational speed. Likewise for the power coefficient, Eqn. 1.3 implies a cubic dependence of power consumption on rotational speed. These dependencies of rotational speed on performance are an unavoidable feature of rotor performance inherent to the physics at play with a rotating wing.

The only way to be able to match both Reynolds and Mach numbers simultaneously with a small-scale model is to manipulate one or more of the fluid properties, ρ, μ, and a. Several studies in the past have taken advantage of this concept by various means, including the use of alternative gasses. One such option is dichlorodifluoromethane, known commonly as Freon-12 or R-12, which has a density approximately four times that of air. The speed of sound in R-12 is also approximately half that in air, which facilitates transonic wind tunnel testing with much lower power requirements [1,5,6]. In the case of small-scale rotor testing, the decreased speed of sound is counterproductive to the goal of matching full-scale Reynolds and Mach numbers simultaneously. The increase in density results in a Reynolds number four times as large as that in air for a given velocity, and the decreased speed of sound results in a doubling of the Mach number. As the viscosity of R-12 is approximately the same as air, the Reynolds number can be effectively doubled for a given Mach number [6]. In contrast, compressed-air at four times ambient density would result in a Reynolds number four times as large for a given Mach number, rather than the doubling obtained with R-12. The use of R-12 presents some experimental challenges, including a difference in the ratio of specific heats compared to air which can alter compressibility effects, though below Mach numbers of 1.4, any discrepancies are typically small [5,6,41].

Compressed-air presents an attractive option compared to the use of alternate gasses, as it allows for continuous changes in density to suit the needs of any given experiment. The use of compressed-air also avoids the additional costs associated with purchasing and recovery after use of specialized gasses, and any safety hazards which may be present

such as suffocation or toxicity. In addition, the speed of sound remains relatively constant in compressed air for a wide range of pressures [42]. If desired, a facility capable of experiments using compressed-air as a testing medium could be retrofitted to be able to operate with alternate gasses as well, possibly even at varying pressures to allow for an even wider range of test conditions. In contrast, upgrading a facility which was not designed from the onset to be able to contain compressed gasses would likely not be possible, and require a complete rebuild. Any such facility would be classified as some form of pressure vessel, and be subject to the relevant codes and standards.

1.5.1   Airfoil Performance Trends

The overall performance characteristics of an airfoil can be a strong, and often nonlinear function of Reynolds number. For certain regimes there may be little to no variation, while in others a strong correlation may exist. While there are often three-dimensional effects which play a role in rotorcraft aerodynamics, a simple analysis based on two-dimensional airfoil theory can often provide a good approximation to the overall behavior and characteristics of a vehicle or rotor system [26]. Airfoil theory can therefore provide a basis upon which to analyze and draw conclusions about rotor performance trends.

The detailed aerodynamics of a rotor and the airfoils that it consists of can depends highly on the Reynolds numbers at which they are operating. Much of these effects can be linked to the behavior of the boundary layers on the blades; of particular interest is the presence of turbulence and/or boundary layer separation. When studying rotorcraft aerodynamics, fully turbulent conditions are typically observed in vehicles such as helicopters, which tend to operate at Reynolds numbers on the order of 10^7, whereas Reynolds numbers on the order of 10^6 or below tend to display more transitional behavior [43].

The boundary layer on an airfoil refers to the thin region next to the surface in which viscous effects are significant. The particles of air in contact with a surface are assumed to remain in place, and have zero velocity relative to it. This assumption is known as the no-slip condition [44–46]. With the imposition of zero velocity along a surface, and the necessity for nonzero velocity away from it, there must exist an intermediary region where a strong velocity gradient is present. The boundary condition of a solid impermeable surface also requires that there be no flow through the surface of the airfoil, resulting in the normal component of velocity being negligible in the vicinity of the surface. These conditions form the basis of the assumptions of boundary layer theory [44]. The behavior of the boundary layer on an airfoil is sensitive to a number of conditions, including

the pressure distribution along the surface, and the presence of turbulence. A typical pressure distribution on the upper surface of an airfoil displays several characteristics: a rise in pressure relative to the free-stream at the stagnation point near the leading edge, a subsequent drop in pressure along the upper surface to below free-stream conditions, known as the suction peak, and a subsequent rise to return to free-stream pressure as the air approaches the trailing edge, known as the pressure recovery region [47–49].

The pressure recovery region presents a challenge for the boundary layer, as an adverse pressure gradient has the potential to cause separation to occur. If the flow remains laminar past the suction peak on the upper surface of the airfoil, and the adverse pressure gradient in the recovery region is sufficiently strong, the boundary layer may detach from the surface, creating a region of trapped, recirculating air next to the airfoil; if the boundary layer later reattaches, it is deemed a Laminar Separation Bubble (LSB) [47, 50]. Within an LSB is a volume of recirculating air which remains near the surface of the airfoil. The air near the front of the bubble remains nearly static, forming a region of constant pressure [50]. The separation of the boundary layer from the airfoil can induce transition to turbulence, which significantly alters the characteristics and behavior of the boundary layer. The presence of turbulence brings about increased mixing, which results in a decrease in the momentum deficit in the boundary layer as higher momentum fluid is drawn in from the surroundings; this can provide the boundary layer with the energy it needs to reattach, forming the separation bubble [47, 51]. For high Reynolds numbers, the boundary layer more readily transitions to turbulence and is therefore able to better resist separation, or reattach more quickly, leading to smaller separation bubbles [47, 48, 50, 51].

Fundamentally, an LSB is the reversal of flow near the surface of the airfoil due to a sufficiently strong adverse pressure gradient over a section of the surface, after which the flow continues to follow the surface of the airfoil. If this region of recirculating flow is sufficiently large, it can have a significant effect on the overall pressure distribution along the surface of the airfoil, and the LSB is referred to as a *long bubble*. In contrast, a *short bubble* is one which does not have a considerable effect on the surface pressure distribution along the airfoil, and therefore lift is not strongly affected [47, 48]. The length of a separation bubble is dependent on a number of factors, including the Reynolds number, typically getting longer as Reynolds number decreases. Short bubbles, which span no more than a few percent of the total chord, are common for higher Reynolds numbers on the order of 1×10^6, whereas long bubbles covering a substantial portion of the airfoil surface can be present for lower Reynolds numbers, on the order of 1×10^5 or

below [47–49]. For an airfoil over which the boundary layer remains attached, potential flow theory provides the result that the lift coefficient C_l is a linear function of the angle of attack, α [52]. As the boundary layer begins to separate, C_l deviates from this linear trend, and reduces in magnitude.

In addition to variations in airfoil performance with changes in Reynolds number, some evidence exists that the maximum achievable lift coefficient before an airfoil stalls may depend on Mach number, even for Mach numbers as low as 0.15 [4]. For Mach numbers below this, variations in Reynolds number appear to be relatively more important, implying that compressibility effects are negligible [53]. As the Mach number increases further beyond 0.15, Reynolds number effects become less dominant [54]. The dependence of the maximum lift coefficient on Mach number also has some correlation with the roughness of the airfoil surface; airfoils with roughness at the leading-edge did not display any changes in the stall behavior of the airfoil, and that stall occurred gradually as opposed to a sharp drop off in lift [55]. This suggests that compressibility effects are more pronounced when the boundary layers on an airfoil are laminar for Mach numbers ranging from 0.1 to 0.5.

1.5.2   Blade Element Theory Analysis

The differences in performance observed as a function of Reynolds number are often most strongly linked to the profile drag produced by the rotor blades [39]. Some theoretical justification for this based on a BET analysis will be presented here. Such an analysis will prove to be useful later when analyzing the results in chapter 4. BET allows for convenient application of the concepts of airfoil theory to a rotating wing, in which a number of parameters can vary along the span due to the rotational nature of its operation. The airfoil profile of which the rotor blade is composed, the angle of attack, and relative flow velocity can all be functions of the radial location [9].

The key feature of BET is that a blade can be discretized into a number of individual airfoil sections, which can then be treated as a series of quasi-2D airfoils of some finite spanwise width, known as blade elements. One such element is shown in Fig. 1.1, with relevant quantities labelled. This implies a key assumption, that spanwise aerodynamic effects can be neglected such that the performance of any given blade element is independent of those adjacent to it. The velocity observed by each blade element can be determined by the motion of the rotor through the air, both rotational and translational, and a component of velocity induced by the rotor. The local angle of attack is then determined, and lift and drag forces can be computed. The aerodynamic forces for a

given blade element can then be transformed to the global rotor frame and summed with the remaining elements to calculate overall forces and moments produced by the rotor, as well as the total power required to sustain operation. BET alone does not account for the ability of a rotor to induce flow through it, which changes the velocity seen by the airfoil sections. For the purposes of the argumentative analysis presented in this thesis, reasoning based on BET alone will suffice with the caveat that a distribution of induced velocity exists on the rotor disk, and is small relative to the in-plane component of velocity seen by a given airfoil section. The details of the inflow distribution will be ignored as BET is not being used here to quantify rotor performance. It serves this discussion merely as a logical tool to make hypotheses about the blade-level aerodynamics of the rotor from the global performance parameters such as total thrust and power. Despite the lack of any quantification of the inflow distribution, the theory behind BET and the resulting equations discussed hereafter provide insight into the general trends in rotor performance as the aerodynamic conditions vary.
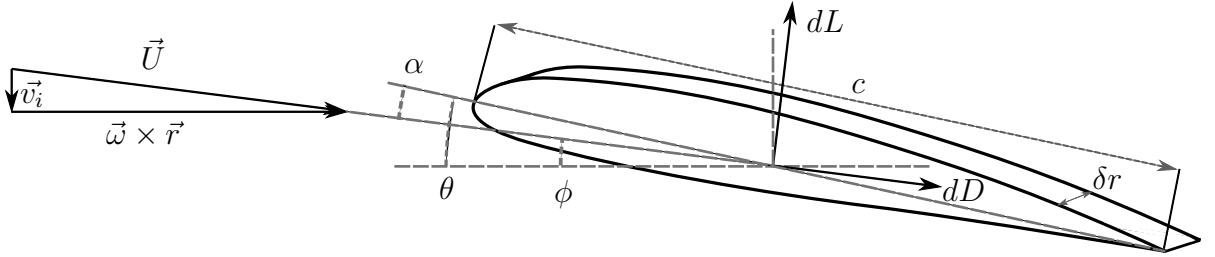
Figure 1.1. Schematic of a single blade element, showing the relevant dimensions, velocity components, and angles.

From the principles of BET and the schematic shown in Fig. 1.1, some basic equations can be written to describe the performance of the rotor in terms of the individual blade sections. The lift produced by airfoil section of width δr is determined by Eqn. 1.8.

$$dL = \frac{1}{2}C_l\rho U^2 c\delta r \tag{1.8}$$

Likewise, the drag produced by the same section can also be defined, as in Eqn. 1.9.

$$dD = \frac{1}{2}C_d\rho U^2 c\delta r \tag{1.9}$$

The lift and drag as defined above represent the total force produced by a single blade element, decomposed into two orthogonal components defined relative to the relative flow direction, indicated in Fig. 1.1 by the inflow angle ϕ. In general, these components do not align with the directions of interest for evaluating rotor performance, namely the

thrust direction which is perpendicular to the rotor plane, and an orthogonal direction which is locally opposed to the tangential motion of the rotating blade element, relevant for computing the power consumed by the rotor. Assuming that the rotor is rigid, and there are no hinges for flap or lead-lag motion as in a helicopter such that the only degree of freedom for blade motion is rotation about the shaft axis, the local lift and drag components can be transformed into global rotor thrust using the inflow angle as in Eqn. 1.10.

$$dT = \frac{1}{2}(C_l cos\phi - C_d sin\phi)\rho U^2 c \delta r \tag{1.10}$$

Thus both lift and drag have an effect on the thrust produced by the rotor, as well as the power, defined in Eqn. 1.11.

$$dP = \frac{\omega r}{2}(C_l sin\phi + C_d cos\phi)\rho U^2 c \delta r \tag{1.11}$$

Eqn. 1.10 and Eqn. 1.11 represent the thrust and power respectively produced by a single blade element. The total thrust produced by the rotor, as well as power consumed by the rotor must take into account the entire blade span, and each of the individual blades. Assuming the rotor is operating in hover and that the conditions seen by a blade do not vary around the rotor azimuth, the total thrust produced by the rotor can be represented by summing over all n blade elements, and multiplying by the number of blades N_b, as in Eqn. 1.12.

$$F_z = N_b \sum_{i=1}^{n} \frac{1}{2}(C_{l_i} cos\phi_i - C_{d_i} sin\phi_i)\rho U_i^2 c_i \delta r \tag{1.12}$$

Likewise, total rotor power can be described by Eqn. 1.13.

$$P = N_b \sum_{i=1}^{n} \frac{\omega r_i}{2}(C_{l_i} sin\phi_i + C_{d_i} cos\phi_i)\rho U_i^2 c_i \delta r \tag{1.13}$$

For a rotor operating in hover, the component of relative velocity observed by a blade element due to the rotor's rotational motion is typically much larger than the inflow velocity. This results in ϕ being a small, positive angle, such that $cos\phi \approx 1$, and $sin\phi \approx \phi$. In order to comment on the dependence of thrust and power on lift and drag respectively, an analysis of the glide ratio, or the ratio of lift to drag produced by an airfoil, is required. As an example, airfoil data for the profile at the 75% radial station of the rotor used in the present study will be examined. Lift and drag data was generated for a range of angles of attack, and Reynolds numbers using the airfoil analysis program

XFOIL.

Fig. 1.2 shows a plot of the glide ratio for over this operating space. Typical values for the lift coefficient of the airfoil are on the order of 40 to 60 times greater than the drag coefficient, though there is a nonlinear dependence on both angle of attack, and Reynolds number. By looking at similar plots for the individual lift and drag coefficients, some insight into this behavior can be gained. As the angle of attack increases for a given Reynolds number, the lift coefficient increases linearly up to the point that separation effects begin to dominate. At lower Reynolds numbers, there is a gradual decrease in the slope of the lift curve over a small range of angles of attack. It is hypothesized that this is due to the presence of a LSB, which increases in size as the pressure gradient on the suction side of the airfoil becomes more adverse. Eventually, the boundary layer on the suction side of the airfoil stalls, causing a sharp drop off in lift. As the Reynolds number increases, the worsening of the LSB is delayed and extended, allowing it to grow larger before the boundary layer stalls completely. This results in a more gradual drop in the lift curve, as seen in Fig. 1.3(a) for the higher Reynolds number cases.
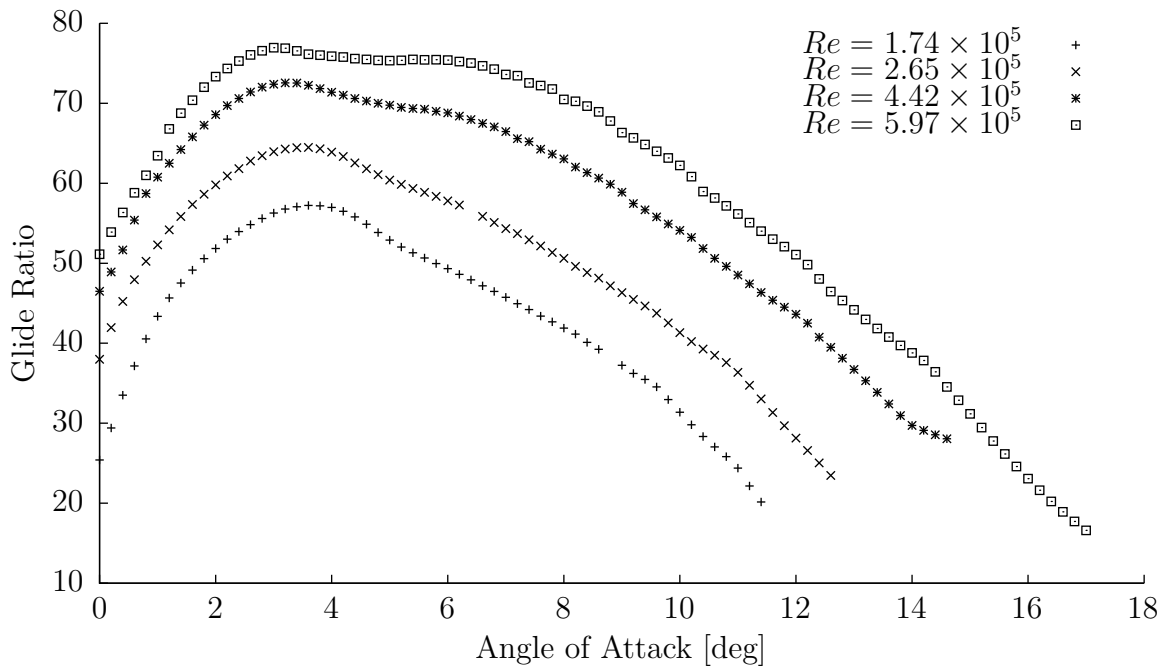
Figure 1.2. Glide ratio of the airfoil at the 75% radial station as a function of angle of attack and Reynolds number.

Due to the same evolution of the LSB, variation in the drag coefficient, shown in Fig. 1.3(b) was also observed. As the LSB grows with increasing angle of attack, the drag coefficient increases slowly at first, then more rapidly as the airfoil approaches stall.
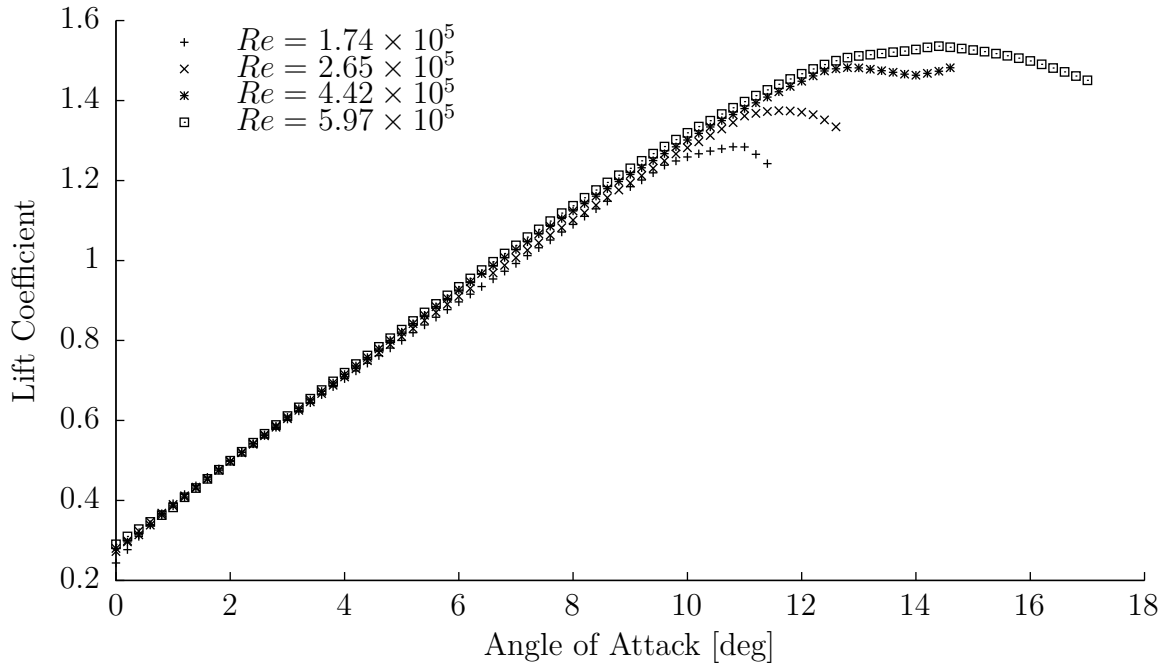
(a) Coefficient of lift vs angle of attack and Reynolds number.
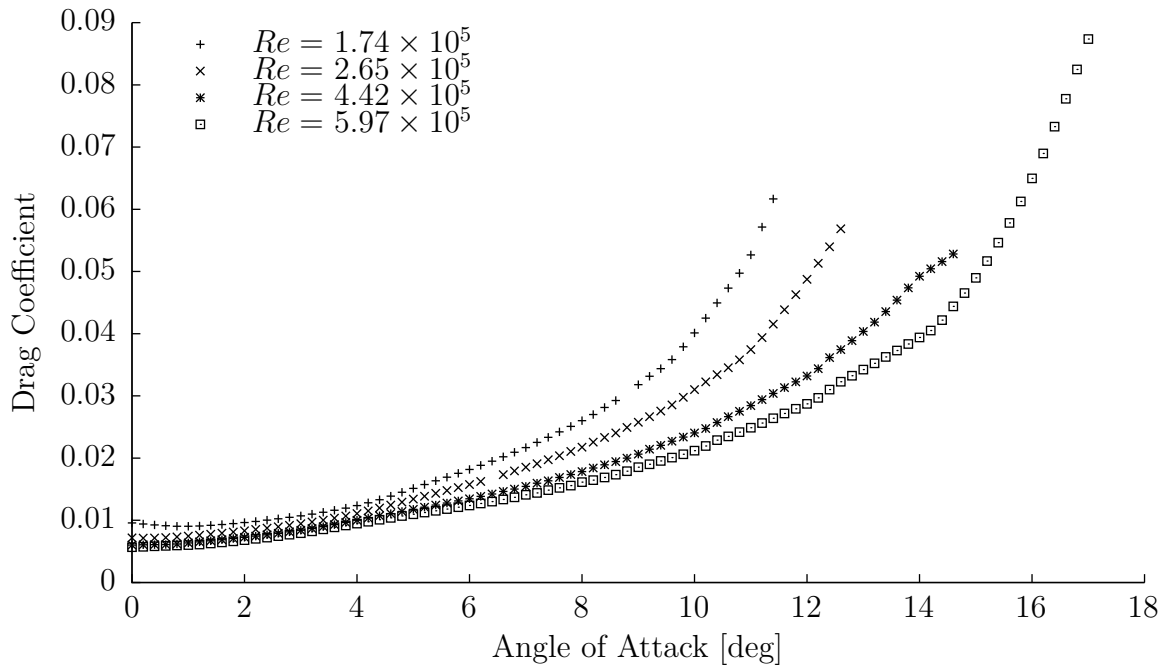
(b) Coefficient of drag vs angle of attack and Reynolds number.

Figure 1.3. Lift (a) and drag (b) polars for the airfoil at the 75% radial station, as a function of Reynolds number, from angles of attack of 0° to the point of stall.

This explains the behavior seen in Fig. 1.2; for smaller angles of attack, the increase in lift with angle of attack dominates the increase in drag, but the trend reverses for larger

angles as the airfoil approaches stall. As a conservative lower bound, the glide ratio can be assumed to be greater than 10 for the majority of the rotor's operating range, though larger values will be observed for greater Reynolds numbers.

Assuming all else remains constant, the effect that an increase in Reynolds number will have on the overall rotor performance depends on the state of the rotor, and the boundary layers on its surfaces. If the boundary layers are attached and no strong effects from an LSB are present, the airfoil will be operating somewhere in the linear region of the lift curve. In this case, an incremental change in Reynolds number will not affect the lift coefficient, as changes only occur in the vicinity of the stall point. Conversely, changes in Reynolds number will affect the drag coefficient regardless of the particular condition at which the airfoil is operating. As shown in Fig. 1.3(b), increasing the Reynolds number leads to a reduction in drag across the entire range of operation.

Since ϕ is presumed to be small, and C_l is typically at least an order of magnitude greater than C_d, it can be shown from Eqn. 1.12 that the rotor thrust is most strongly dependent on the lift coefficient of its constituent airfoil sections, and minimally dependent on drag. From Eqn. 1.13, the power consumed by the rotor is in general dependent on both C_l and C_d. For glide ratios of 10, and values of ϕ on the order of 0.1, or roughly 6°, the lift and drag terms in Eqn. 1.13 will be approximately equal, and the consumption of rotor power will be evenly split between induced power and profile power. From Fig. 1.2, if the glide ratio is greater than 10 over the majority of the operating space, induced power dominates over profile power. While this simplified reasoning is by no means a comprehensive analysis of the performance of a rotor, it provides some insight into the mechanism behind changes in the overall performance of the rotor with Reynolds number.

The trends in airfoil performance will vary from one airfoil to the next, and will in general change for different Reynolds number regimes. As discussed previously, the performance of an airfoil is tied strongly to the behavior of the boundary layers on its surfaces, and the presence and intensity of turbulence. One study examined small-scale wind turbine models in a compressed-air environment, and quantified changes in performance with Reynolds number; it was shown that the high-Reynolds number performance characteristics could be obtained at much lower Reynolds numbers by tripping the boundary layers by adding roughness to the leading edge of the blades [56].

The dependence of airfoil behavior on Reynolds number can have a considerable effect on the performance of a rotor, potentially impacting both the thrust produced by, and power consumed by, a rotor. This further outlines the need to properly replicate the

aerodynamic conditions at which a rotor operates in an experiment in order to accurately quantify its performance. The theoretical discussion on rotor aerodynamics using BET will be useful later in chapter 4 when analyzing the experimental results and making conclusions about the aerodynamic behavior of the rotor.

Chapter 2 |
Experimental Facilities

Using compressed air to achieve dynamic similarity on small-scale model rotorcraft blades is a task which requires a suite of specialized equipment, both to conduct the experiments themselves, and to provide supporting data to ensure the accuracy and quality of the data. This chapter outlines the equipment used, including off the shelf components, and any custom hardware or devices which were developed for this purpose.

2.1 The Compressed Air Wind Tunnel

In order to replicate full-scale Reynolds and Mach numbers simultaneously with small-scale experimental models, one or more of the air's physical properties must be manipulated. The Pennsylvania State University's new Compressed Air Wind Tunnel (CAWT) was designed with this purpose in mind, providing an environment in which the internal pressure of the air can be raised to 500 psi, or 34 atm above atmospheric conditions. This results in a corresponding increase in air density, which can be used to control the Reynolds number at which the models operate independent of the scale and velocity. The relationship between density and Reynolds number is effectively linear, as the dependence of viscosity on pressure or density is very weak [57]. The Mach numbers observed on the models will not be affected, as the speed of sound in air is also not a strong function of pressure over the range of pressures obtainable in the CAWT [42].

The CAWT, shown below in Fig. 2.1, consists of a large pressure vessel of circular cross section. Additional hardware will be installed within the pressure vessel to construct a closed-loop, low-speed wind tunnel, including a fan, a series of turning vanes in each corner, a flow conditioning section to reduce turbulence, and ductwork to form the test section, diffusers, and contraction nozzle. The present study examines the performance of a rotor in hover with the rotor operating in stagnant air, and so the CAWT is being
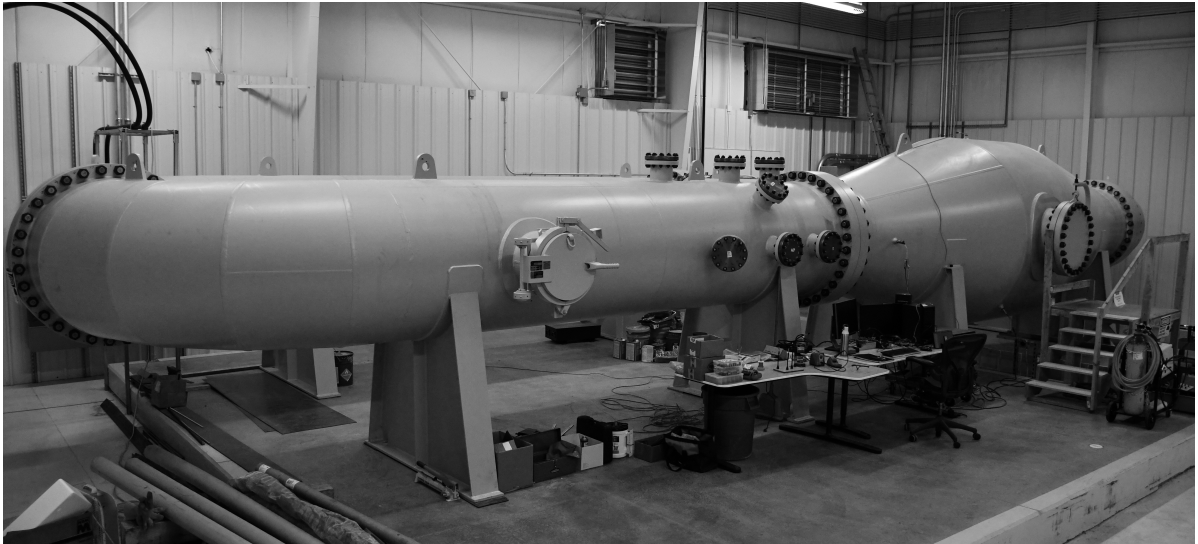
Figure 2.1. The Pennsylvania State University's new Compressed-Air Wind Tunnel facility: a closed-loop wind tunnel constructed inside of a large pressure vessel designed to enable experiments at high Reynolds numbers using small-scale models.

used solely as a pressure vessel with no mean flow being produced by the facility. To better take advantage of the available space, the experiments were conducted in the larger-diameter section of the tunnel which will later be used as the flow conditioning chamber, as indicated in Fig. 2.3. In future studies, the full capabilities of the wind tunnel will be used to replicate a wider range of operating conditions, including flight conditions at a variety of incidence angles in which more complex aerodynamic interactions are likely to occur. The CAWT is outfitted with a series of high-pressure electrical compression seal feedthroughs from Conax Technologies, including a PL-14-4 which contains four 14-gauge wires used for power transmission, and two TG-24T series feedthroughs for the instrumentation hardware. The power feedthrough is outfitted with Anderson Powerpole connectors on both the inside and outside of the CAWT, to ensure the system is as modular and reconfigurable as possible. The instrumentation feedthroughs make use of D-sub connectors for the same reason. Male and female connectors were installed on the cabling and feedthroughs such that the hardware internal to the CAWT can connect directly to the external hardware without the feedthrough in between without the need for any sort of adapter, in order to simplify assembly, testing, and debugging.

2.1.1 The Pressurized-Air Rotor Testing System

The Pressurized-Air Rotor Testing System (PARTS-I) was developed to be able to mount a rotor inside the CAWT, drive it to the desired operating conditions, and instrument it in such a way that the relevant loads could be measured. The test-stand consists of a structure fabricated out of aluminum extrusions, which is mounted to the internal walls of the CAWT. A schematic of the setup is is shown in Fig. 2.3, displaying the mounting configuration within the CAWT.

Attached to the end of this structure is the so called measurement stack, the equipment used to drive and instrument the rotor, shown in Fig. 2.2. The main element of the measurement stack is an ATI Delta six-axis load cell which is capable of measuring all six components of force and torque produced by the rotor during operation. The design of the measurement stack incorporates thermal isolation in the mounting hardware connecting the motor to the load cell, to prevent heat generated during operation from conducting into the load cell. While load cells of this type compensate for variations in temperature, this compensation is only effective if the entire device is at a uniform temperature. When a heat generating device like a motor is connected to a load cell, it can induce temperature gradients through the sensing element of the device, which can affect the accuracy of measurements as the temperature compensation cannot account for such variations [58]. To reduce heat transfer from the motor to the load cell, a nylon buffer plate was included in the interface between them. This avoids a continuous metal structure between the motor and the load cell, which would act as a heat-pipe. A second nylon buffer plate is used to mount the load cell to the frame of the PARTS-I.

The rotational speed of the rotor is measured using an off the shelf infrared proximity sensor, the HiLetgo HW-201, which detects the passage of each blade. The sensor is mounted on the outer-diameter of the interface plate between the load cell and motor, and is aimed at the inboard section of the blade, upon which a patch of white paint was applied to facilitate proper reflection of the emitted infrared signal back to the sensor. The sensor outputs an analog voltage proportional to the distance between it and the nearest object in its line of sight. When aimed at the inboard section of the rotating blade, the sensor outputs a signal consisting of square pulses as each blade passes in front of it. The signal is read into LabVIEW as an analog waveform, and the time interval between adjacent blade passages is calculated, and used to determine the rotational speed.
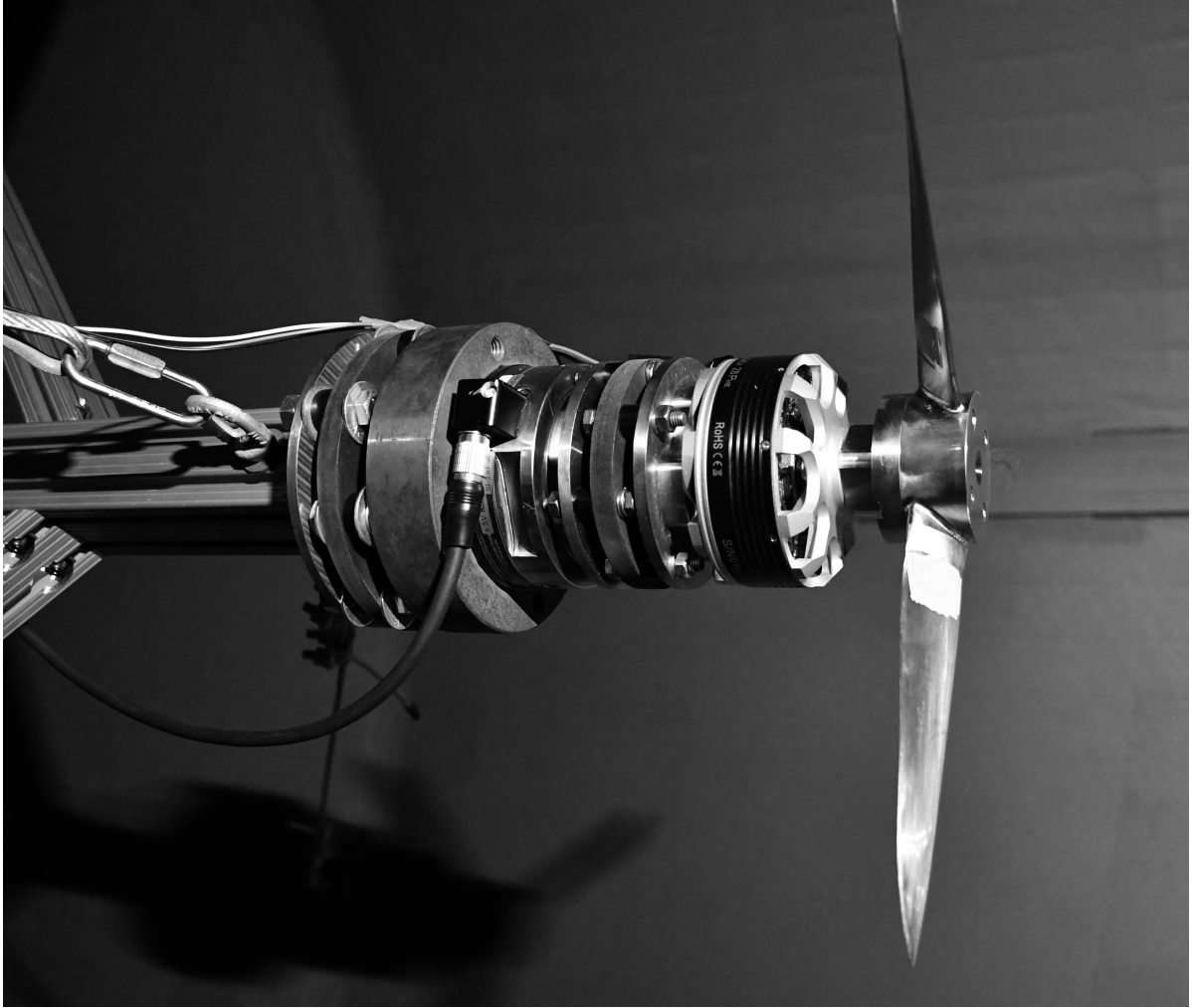
Figure 2.2. The PARTS-I installed in the CAWT, showing the load cell, motor and stainless-steel rotor.

2.1.2 Computer Interface for Data Acquisition and Control

The measurements from the load cell are read in to LabVIEW using a dedicated NI PCI-6220 data acquisition card, whereas the rest of the sensor data is acquired through an NI cDAQ-9178 C-Series Data Acquisition (DAQ) chassis with various input modules including an NI-9215 analog input module for the proximity sensor used for rotational speed measurements. The motor is driven by a KDE-UAS95HVC 95A+HV Electronic Speed Controller (ESC), which was in turn controlled via a Pulse Width Modulated (PWM) signal provided by an Arduino Mega 2560. Arduino code was developed to gradually ramp up the rotor speed in response to operator commands for a defined set-point, to prevent the ESC from reaching its maximum allowable current, upon which

it would shut down to avoid damage. The stainless-steel rotor caused excessive torque requirements during acceleration, as it has a greater mass moment of inertia than the plastic or composite rotors it is designed to be used with. The data acquisition was handled using LabVIEW. All the data acquisition hardware are listed in table 2.1. A full list of the transducers used, along with their measurement uncertainty values, is provided in § 2.4.

Model Name	Data Acquired	Bit Depth	Sample Rate (Per Channel)
NI PCI-6220	Load Cell Data	16 Bit	40 kHz
NI 9215	Blade Passage	16 Bit	100 kHz

Table 2.1. Data acquisition hardware used in conjunction with the transducers in the PARTS-I.
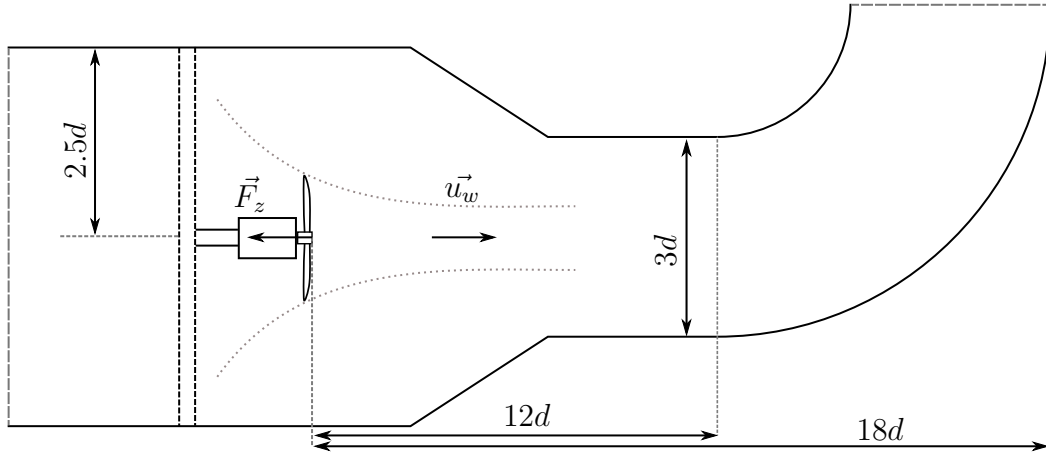
Figure 2.3. Schematic of a cross sectional view of the CAWT, showing the PARTS-I mounted inside, along with relevant dimensions specified in terms of the rotor diameter d, including the test chamber diameter, and the distance from the rotor plane to the elbow. Schematic is not to scale.

2.2 Coaxial Acoustics Test System

The Coaxial Acoustics Test System (CATS) is an existing facility at The Pennsylvania State University, designed to be able to test small rotor models in hover and forward-flight at varying angles of incidence. It can accommodate single rotors, as well as rotors in a coaxial configuration. In addition to a six-axis load cell which can quantify the performance of the rotor, there is an array of microphones to characterize the noise produced by a rotor over a range of directivity angles. The rotor stand in the CATS

consists of a similar set of hardware as the PARTS-I, but is situated within the test section of an open-jet, anechoic wind tunnel. It was built to accommodated rotors of approximately 0.38 m in diameter, a limit set in part by the details of the included microphone array [58]. While not a part of the main experimental campaign, this facility was used as part of a verification study to examine the performance of the PARTS-I, discussed in more detail in § 3.1.2.

2.3 Rotor Models

The rotor used in this study is composed of a generic blade geometry provided to The Pennsylvania State University by Joby Aviation, which is typical of the style of rotor that may be used on an eVTOL or UAM vehicle, but differs from the proprietary designs used on Joby's vehicles. The rotors fabricated for testing consist of three blades, set to a fixed collective pitch angle for each experiment. No cyclic pitch control mechanism was incorporated into the rotors, as UAM vehicles tend not to implement cyclic pitch as a control strategy. The geometry is based on a full scale rotor diameter of 2.9 m, and was scaled down to a model diameter of 0.36 m. Two rotor models were fabricated for testing purposes. First, a model with 3D-printed blades mounted on a variable-pitch hub was fabricated for preliminary testing. This rotor allowed the collective pitch to be manually changed prior to testing, but did not incorporate actuators to allow pitch control during operation. The variable-pitch rotor, shown in Fig. 2.4, allowed a wide range of operating conditions to be examined quickly at atmospheric pressure, in order to narrow down a more focused test matrix for the compressed-air study. This rotor was also used for a facility verification study which will be further discussed in § 4.3. For the experiments conducted in compressed-air, a rotor was machined out of stainless-steel in order to be able to withstand the increased loads which would result from the higher density. The stainless-steel rotor is shown mounted to the PARTS-I in Fig. 2.2. In order to simplify the design of the rotor for ease of manufacturing, the rotor was designed with a fixed collective pitch of 15°, defined by the pitch angle of the airfoil at the 75% radial station. The fixed-pitch design also allowed the rotor to be machined from a solid piece of stainless-steel, which offers improved strength over a multi-component assembly.

The geometry of the rotor blades varies along the span of the blade, with thicker airfoil sections being used at the root compared to the more outboard sections. The twist distribution of the blade is approximately linear, with 34° of twist from root to tip. The chord distribution varies nonlinearly, with the chord tapering off near the blade root

Figure 2.4. The 3D printed rotor blades mounted on a variable-pitch hub machined out of aluminum.

and tip. More details of the rotor geometry are provided in appendix B, including airfoil section geometry at select radial stations, the chord and twist distributions along the blade span, and the details of the rotor hubs used in the study.

2.4 Uncertainty Analysis

In order to be able to perform any meaningful analysis on the data, an uncertainty analysis must be done to quantify the experimental errors in the measurements. The

analysis in this section will allow for a discussion on the accuracy of the results which will be presented in chapter 4. Here, a summary of all the sources of error in the various measurements will be outlined, along with estimates of their magnitude, and discussion of some caveats and additional considerations.

2.4.1 Measurement Uncertainty

The main metrics used to quantify rotor performance in this study are the thrust and power coefficients, and their variations with Reynolds number and Mach number. The thrust coefficient is calculated from the measured values of thrust, density, and rotational speed. The power coefficient on the other hand, uses the measured torque, density, and rotational speed, with power being calculated as the product of torque and rotational speed. The density is also a calculated quantity, based on measurements of pressure and temperature, using an empirical model which accounts for real-gas compressibility effects as discussed in more detail in appendix C.1.

The error associated with the measurements from the load cell is quantified by the manufacturer by a series of tests which subject the load cell to varying magnitudes, and combinations of forces and moments. The result is a characterization of the expected measurement error over a wide range of conditions, which can be used to estimate an expected error magnitude. For all six measurement axes, most of the test cases provided in the calibration data sheet resulted in a measurement error at or below 0.1% of the maximum rated load for that particular measurement axis. The maximum rated loads are 990 N for the thrust axis, 330 N for the lateral force axes, and 30 N m for the torque and moment axes. The corresponding estimate of measurement uncertainty for the load measurements is therefore ± 0.99 N for the thrust axis, ± 0.33 N for the lateral force axes, and ± 0.03 N m for the torque and moment axes.

The uncertainty estimates are based on testing done by the load cell's manufacturer, which involved only static loading conditions, and does not account for any variation in accuracy due to dynamic loading or vibration. There is no data available on whether the measurement error changes under dynamic loads. Due to imbalances or asymmetries in the system, the forces and moments measured by the load cell are oscillatory in nature, and do not necessarily reflect the conditions under which the measurement error was quantified. The worst-case scenarios from the manufacturer's error testing in which the largest measurement errors were observed involve strong multi-axis load coupling. In these test points, loads of large magnitude were applied to multiple axes at the same time. For the present experiments, the largest load observed at a given test point was

the force along the thrust axis with all other forces and moments being much smaller in magnitude. Due to the relatively weak cross coupling of loads, it is hypothesized that the error for many of the test cases was less than the previously mentioned estimate of 0.1%. This value was still used in order to provide a conservative estimate of the error while simplifying the error analysis somewhat. The full details of the error quantification done by the manufacturer are presented in appendix A.

The temperature and pressure transducers are both off the shelf components, with their accuracy specified by the manufacturer and verified in an accompanying data sheet. The details of their range and accuracy are listed in table 2.2. The temperature probe is a Resistance Temperature Detector (RTD), and has class A accuracy defined by the International Electromechanical Commission (IEC) 60751 standard, meaning the uncertainty on a temperature measurement falls within $\pm(0.15 + 0.002T)°C$ where T is the temperature in degrees Celsius [59].

2.4.2 Rotor Manufacturing Tolerances

In addition to the uncertainty due to the measurement equipment, there rotor model itself can only be manufactured to a certain level of precision. The chord length along the rotor was used to calculate the Reynolds number, and the radius was used to determine the tip mach number, as well as the rotor disk area. The tolerances on these dimensions, given in table 2.3, are sufficiently small that their effects on the overall uncertainty of a given calculated value can be neglected relative to the other sources of error, as will be discussed in the following section.

The rotational speed of the rotor was determined by measuring the time interval between blade passages using the infrared proximity sensor. The signal from the sensor was sampled at a rate of 100 kHz using LabVIEW, which corresponds to an effective margin of error of $\pm 5 \times 10^{-6}$ s on the blade passage period. The resulting uncertainty on the rotational speed measurements varies with the rotational speed itself, due to the inverse relationship between rotation rate and period. The uncertainty can be represented as a function of rotational speed using Eqn. 2.1.

$$u_{rpm} = 60 * \left(\frac{\omega}{2\pi} - \frac{1}{\frac{2\pi}{\omega} + u_p * N_b} \right)$$
(2.1)

This results in an uncertainty of $\pm$ 0.02% at a speed of 1000 rpm, and $\pm$ 0.124% at 5000 rpm.

2.4.3 Propagated Uncertainty in Calculated Values

For a given measurement which may contain several sources of error e, the overall uncertainty of that measurement u_x can be estimated with the root-sum-squares method, which accounts for the likelihood that different sources of error may not all act to shift the measurement in the same direction simultaneously, or the magnitude of a given error may be less than its estimated maximum for any particular measurement, the so called probable bias [60]. The root-sum-squares method of estimating uncertainty is defined in Eqn. 2.2.

$$u_x = \pm \sqrt{\sum_i e_i^2} \tag{2.2}$$

Calculated quantities such as the thrust and power coefficients incorporate values obtained from a number of independent measurements, each with their own values of uncertainty u_{x_i}. The concept of uncertainty propagation can be used to quantify the cumulative uncertainty of a calculated value [60]. By taking a Taylor series expansion about the mean value of a quantity Y, Eqn. 2.3 can be obtained for the total uncertainty based on the values of the individual uncertainties of the measured values used to calculate it. Given that the values of uncertainty are typically small relative to the mean value, a linear approximation can be obtained by discarding terms of second order or higher from the Taylor series. This provides an approximation for the uncertainty in a calculated value due to the propagated uncertainty of one of its components, defined in Eqn. 2.4.

$$Y = \bar{Y}(\vec{x}) \pm \sum_{i=1}^{n} \left[\left(\frac{\partial Y}{\partial x_i} \right)_{x_i = \bar{x}_i} u_{x_i} + \frac{1}{2} \left(\frac{\partial^2 Y}{\partial x_i^2} \right)_{x_i = \bar{x}_i} u_{x_i}^2 + \cdots \right] \tag{2.3}$$

$$u_{Y_{x_i}} = \left(\frac{\partial Y}{\partial x_i} \right)_{x_i = \bar{x}_i} u_{x_i} \tag{2.4}$$

The partial derivative term in Eqn. 2.4 is referred to as a sensitivity index, θ_i. For quantities which depend on multiple different measured values with their own individual uncertainties, Eqn. 2.4 can be combined with the root-sum-squares method of quantifying the total effect of a number of error sources on a single value, yielding an equation for the total uncertainty of a calculated result, defined in Eqn. 2.5.

$$u_x = \pm \sqrt{\sum_i (\theta_i u_{x_i})^2} \tag{2.5}$$

The task of quantifying the propagated uncertainty on a calculated value then reduces to determining the error in the individual measured values, and computing the sensitivity based on the definition of the parameter of interest.

In the discussion of the experimental results in chapter 4, the thrust and power coefficients defined previously in Eqn. 1.2 and Eqn. 1.3 respectively, will be used to quantify the performance of the rotor over a range of Reynolds numbers and Mach numbers. In order to draw conclusions from these data, the experimental uncertainty of the values must be quantified, a task which this section aims to accomplish. Each of the aforementioned performance coefficients is calculated from a series of individual measured values, each of which has an associated measurement error. The method of uncertainty propagation can be used to account for the cumulative effect of all of all the constituent errors [60].

Since the rotor disk area is defined based on the radius, $A = \pi R^2$, the thrust coefficient can be rewritten as in Eqn. 2.6. The power consumed by the rotor is calculated as the product of torque and rotational speed, so the power coefficient can also be rewritten as Eqn. 2.7, to simplify the uncertainty calculations.

$$C_T = \frac{F_z}{\pi \rho \omega^2 R^4} \tag{2.6}$$

$$C_P = \frac{M_z}{\pi \rho \omega^2 R^5} \tag{2.7}$$

The thrust and power coefficients then each depend on four values: the measured load, either thrust or torque, the rotational speed, the ambient density, and the rotor radius. The sensitivity values can then be determined by differentiating Eqn. 2.6 and Eqn. 2.7 with respect to each variable. The resulting sensitivity values are presented in table 2.4.

Results will also be presented in the form of the figure of merit, which is calculated as in Eqn. 2.8.

$$FM = \frac{F_z^{\frac{3}{2}}/\sqrt{2\rho A}}{M_z \omega} \tag{2.8}$$

As with the thrust and power coefficients, sensitivity values to error in the constituent measured values are presented in table 2.5.

2.5 Convergence of Measured Statistics

In order to determine an appropriate sample length for the data acquisition, an analysis of the statistical convergence of the measurements has been conducted. A summary of this data is presented here along with some justification for the methodology and discussion of the implications of the statistical results.

The raw measured performance data consists of forces and moments in all three axes, as well as rotational speed, both as a function of time. The performance plots shown in this chapter contain the mean of the data from each test point, as the measurements fluctuate in time. In order to calculate a sufficiently accurate mean value, a large enough sample to converge the mean to within a margin of error deemed acceptable is required. In order to evaluate the convergence of the data, Fig. 2.5 displays a running mean of the thrust measurement for a series of rotational speeds at a given ambient pressure, plotted in terms of the number of rotations of the rotor from the start of the sample acquisition. Likewise, Fig. 2.6 shows similar data for the torque measurements which were used to calculate power. The running mean is defined as the mean of a subset of the data from the beginning of the sample to a given point in time, or corresponding number of rotations. The data presented in Fig. 2.5 and Fig. 2.6 are a subset of the entire dataset at a single ambient pressure, though they are representative samples of the general behavior seen across all the data collected. The mean of both thrust and power consistently converge to within $\pm 3\%$ of their final mean after 500 rotations from the start of data collection. Since each sample consisted of a fixed length in time of $20\,\mathrm{s}$, the total number of rotations recorded varies with the rotational speed of the rotor. Some of the data at lower rotational speeds consists of fewer than 500 rotor revolutions, and may not have had time to adequately converge within the sample window. These data were deemed unsuitable for other reasons, based on the measurement error of the load cell, as will be discussed in § 4.4. Beyond 500 rotations, the means continue to converge to within a narrower margin, which indicates running each rotational speed case for at least 1000 rotations would provide better accuracy.

In addition to the running means, the running variance of the thrust and torque values are also plotted. The running variance is defined as the variance of a subset of the available data from the beginning of the sample to the specified number of rotations. The variance, being the square of the standard deviation, represents the overall spread of the dataset about its mean. All of the load measurements were oscillatory in nature, due to vibrations of the system during testing. The running variance plots do not converge

Figure 2.5. Running mean of rotor thrust for each rotational speed measurement at an ambient pressure of 8 atm, normalized as a fraction of the mean of the entire sample.

as quickly as the means, indicating the amplitude of vibration is often a function of time.

Analysing the convergence of the mean throughout a sample is one way to quantify the adequacy of the sample size to provide representative data, but it does not tell the entire story. Examining the higher order statistics, such as the variance, can provide insight into dynamic or oscillatory effects which may not be apparent when analyzing the mean. The variance should also stabilize for a sufficiently long sample, and thus its convergence can serve as another criterion for the sufficience of a sample size. Plots of the running variance for the thrust and torque measurements are shown in Fig. 2.7 and Fig. 2.8. The variance of the thrust and torque data do not appear to be as well converged as the mean, particularly for conditions which contain harmonic content at or near certain frequencies, which are hypothesized to be resonant frequencies of the test stand.

The PARTS-I can be thought of conceptually as a stiff but still elastic structure with some inherent damping and is being excited by a source of vibrational energy spanning a range of frequencies. In the case of a pure excitation of a resonant mode, the expected response would be a vibration amplitude that increases over time before leveling off to a maximum value. This peak amplitude will be determined by the proximity of the excitation frequency to the resonant frequency, and amount of damping in the system.

36
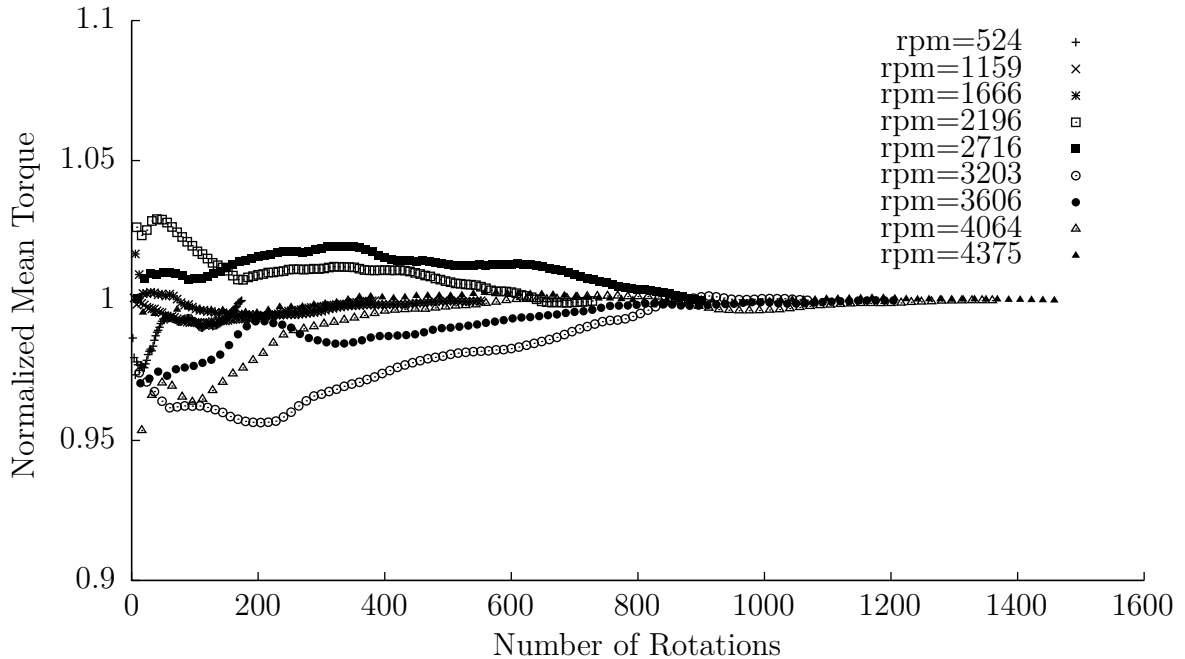
Figure 2.6. Running mean of torque power for each rotational speed measurement at an ambient pressure of 8 atm, normalized as a fraction of the mean of the entire sample.

The time it takes to reach this maximum, is related to the rate of energy being coupled into the system, which again depends on the difference between the excitation frequency and the natural frequency. If the frequency content, or the amplitude of the excitation source changes with time, the rate of energy input to the system will also vary with time, potentially changing sign as well.

Although the load cell is not an accelerometer and therefore cannot directly be used to measure the motion or vibration of the test equipment, it will still respond to the vibrational behavior of the PARTS-I, as it will be subjected to the oscillatory loads. The load cell is mounted near the middle of the test stand. The motor, rotor, and associated mounting brackets and hardware are mounted to the other end of the load cell and are otherwise unsupported. As a first order approximation, the load cell can be represented as a stiff spring, which deflects under an applied load. The rotor hardware, and the remaining frame of the test stand can be represented by lumped masses. With this simplistic model of the system in mind, it is easy to understand that excitation of any vibrational mode would result in oscillatory inertial forces or moments being generated between the rotor hardware and the rest of the test stand, adding harmonic content to the measured loads.

If the variance exhibits strongly non-monotonic behavior, this indicates time varying
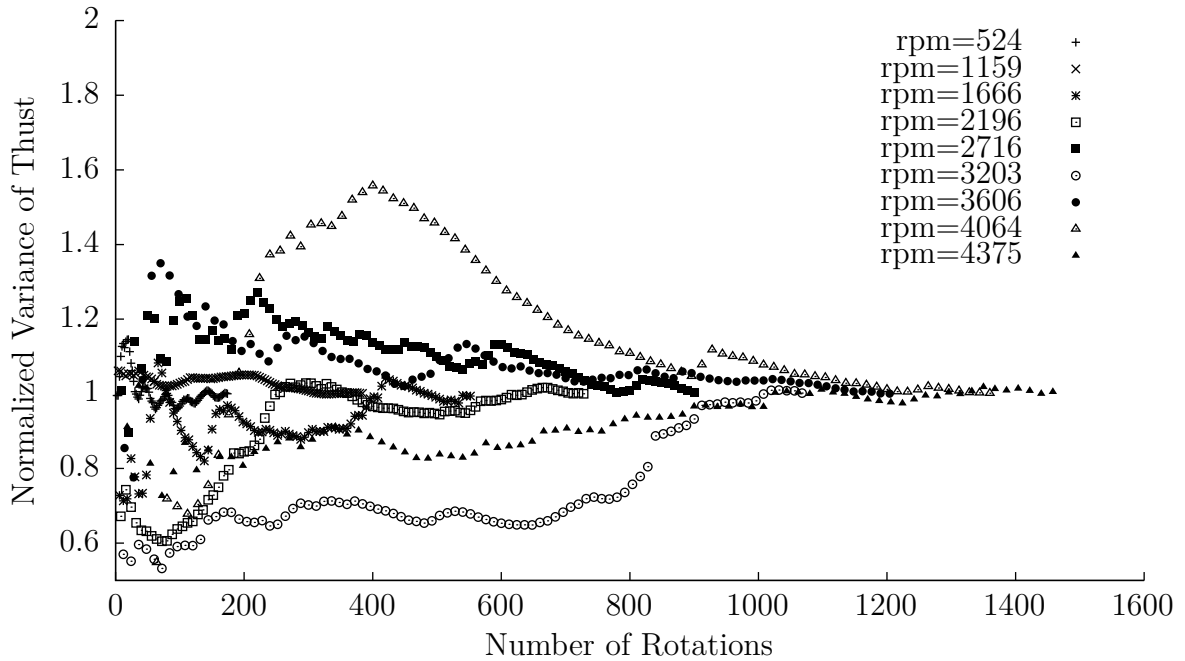
Figure 2.7. Running variance of rotor thrust for each rotational speed measurement at an ambient pressure of 8 atm, normalized as a fraction of the variance of the entire sample.

excitation of the system close to one of the resonant modes. Given that the sources of vibration are the motor, potential imbalances in the rotating mass, and aerodynamic effects on the rotor, this suggests that the time-varying nature of the loads are the result of changes in the rotational speed of the rotor, or unsteadiness in the aerodynamics.
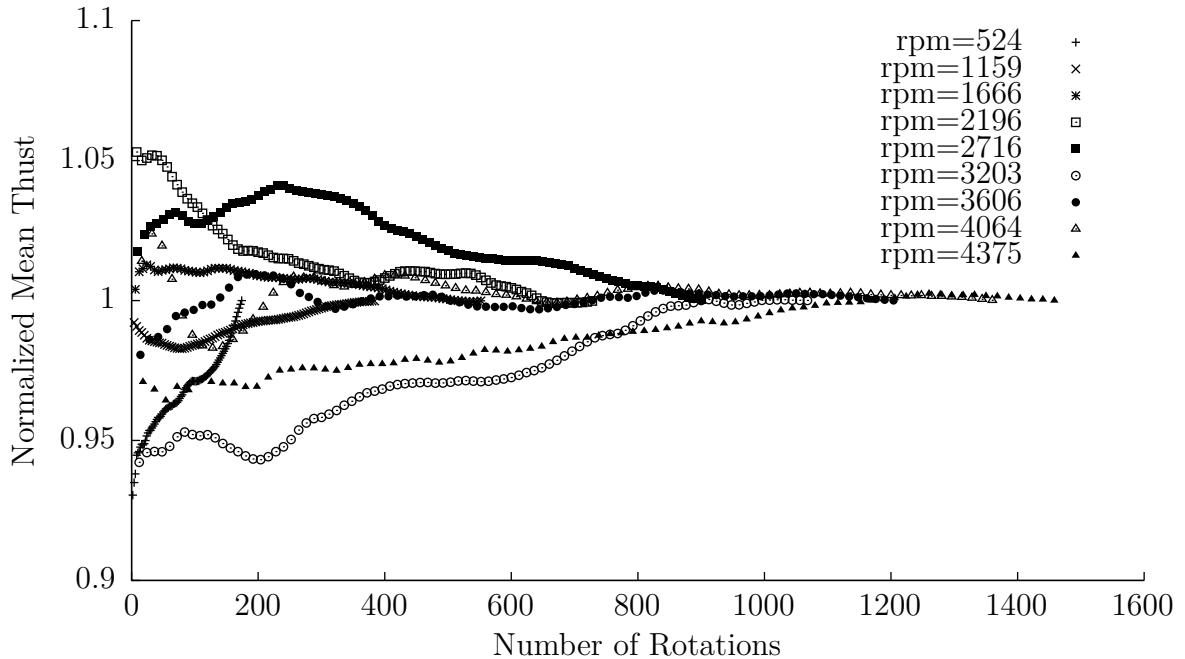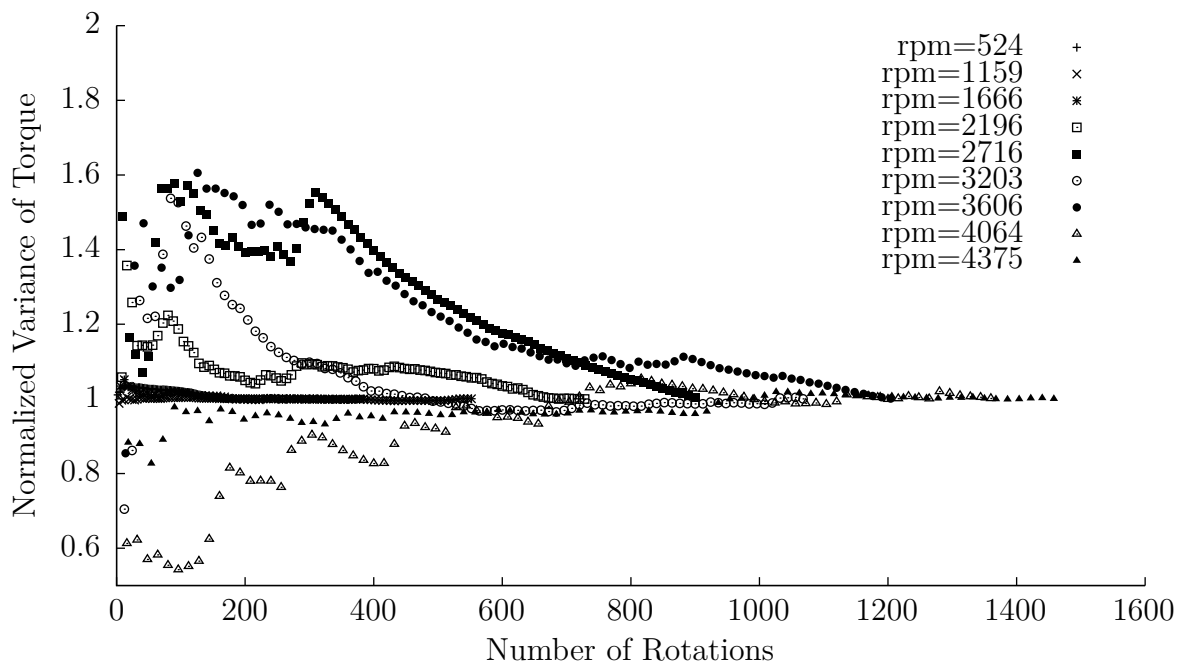
Figure 2.8. Running variance of rotor torque for each rotational speed measurement at an ambient pressure of 8 atm, normalized as a fraction of the variance of the entire sample.

Transducer Model	Measurements	Range	Measurement Error
ATI Delta SI-330-30	Thrust	$-990\,\text{N}$ to $990\,\text{N}$	$\pm 0.99\,\text{N}^*$
	Lateral forces	$-330\,\text{N}$ to $330\,\text{N}$	$\pm 0.33\,\text{N}^*$
	Torque and moments	$-30\,\text{N\,m}$ to $30\,\text{N\,m}$	$\pm 0.03\,\text{N\,m}^*$
Omega PX419-750G10V	Static pressure	$0\,\text{psi}$ to $750\,\text{psi}$	$\pm 0.6\,\text{psi}$
Omega RTD-NPT-72-2-1/8-MTP	Temperature	$0\,°\text{C}$ to $100\,°\text{C}$	$\pm(0.15 + 0.002T)\,°\text{C}^\dagger$
HiLetgo HW-201	Blade passage period		$\pm 5 \times 10^{-6}\,\text{s}$
	Rotational speed		$\pm 60 * \left(\frac{\omega}{2\pi} - \left(\frac{2\pi}{\omega} + u_p N_b \right)^{-1} \right)\,\text{rpm}$

Table 2.2. List of transducers used in the PARTS-I, and their associated measurement uncertainties. Details of the uncertainty analysis are provided in § 2.4.

*The measurement error values of the load cell are a function of the applied loading condition. The values listed here represent conservative estimates based on the available calibration data.

$^\dagger T$ is the true temperature in $°\text{C}$.

Dimension	Symbol	Tolerance ($\pm$)
Blade Chord	c	$1 \times 10^{-4}\,\mathrm{m}$
Rotor Radius	R	$5 \times 10^{-5}\,\mathrm{m}$

Table 2.3. Dimensional tolerances on the rotor geometry due to the manufacturing process.

Variable	Sensitivity of C_T	Sensitivity of C_P
F_z	$\frac{\pi}{2}\rho\omega^2 R^4$	
M_z		$\frac{\pi}{2}\rho\omega^2 R^5$
R	$-4F_z/\left(\frac{\pi}{2}\rho\omega^2 R^5\right)$	$-5M_z/\left(\frac{\pi}{2}\rho\omega^2 R^6\right)$
ρ	$-F_z/\left(\frac{\pi}{2}\rho^2\omega^2 R^4\right)$	$-M_z/\left(\frac{\pi}{2}\rho^2\omega^2 R^5\right)$
ω	$-2F_z/\left(\frac{\pi}{2}\rho\omega^3 R^4\right)$	$-2M_z/\left(\frac{\pi}{2}\rho\omega^3 R^5\right)$

Table 2.4. Sensitivity of the thrust and power coefficients to each of the quantities used to calculate them.

Variable	Sensitivity of FM
F_z	$3\sqrt{F_z}/\left(2Q\omega\sqrt{2\pi\rho R^2}\right)$
M_z	$-F_z^{\frac{3}{2}}/\left(M_z^2\omega\sqrt{2\pi\rho R^2}\right)$
R	$-F_z^{\frac{3}{2}}/\left(2^{\frac{3}{2}}Q\omega R^{\frac{3}{2}}\sqrt{\pi\rho}\right)$
ρ	$-F_z^{\frac{3}{2}}/\left(M_z\omega\rho^{\frac{3}{2}}\sqrt{2\pi R^2}\right)$
ω	$-F_z^{\frac{3}{2}}/\left(M_z\omega^2\sqrt{2\pi\rho R^2}\right)$

Table 2.5. Sensitivity of the figure of merit to each of the quantities used to calculate it.

Chapter 3 |
Procedure

This chapter outlines the methodology used to conduct the experiments, and to collect and process any relevant data used for analysis in chapter 4. This includes information on general procedures, data sampling, and post-processing steps.

3.1 Experimental Methodology

The procedure used to conduct the experiments will be explained here. Details of the setup, calibration and testing for the various phases of the experiment are provided. The main experimental study of a rotor operating in a range of ambient pressures will be described, along with several complimentary experiments which serve to improve the confidence in the results. A check of the accuracy of the load cell used in the rotor experiments was conducted, along with a comparison between data from the PARTS-I and another similar rotor testing facility at The Pennsylvania State University.

3.1.1 Load Cell Verification

Prior to assembling the PARTS-I, the accuracy of the axial force measurement of the load cell, corresponding to the rotor thrust axis, was verified. The load cell was first positioned flat on a level surface, the calibration file was loaded into the data acquisition software, and the device was tared using the LabVIEW acquisition code provided by the manufacturer. Weights were then placed on top of the load cell, in order to load it in compression along the z axis, normal to the surface of the interface plate. The corresponding force measurements were recorded an compared to their actual weights, as determined by a digital balance which was accurate to within $\pm$ 0.1 g. The load cell was then fixed to a rigid surface and loaded in tension. A steel bar was bolted to the

load cell's measurement plate, from which a strap could be attached. This strap was fed around a pulley, such that the tensile load was applied directly along the z axis, and weights could be hung from the other end without interfering with the mechanical setup. Force measurements were then recorded as before.

3.1.2 Verification Study

Since the rotor testing stand used in this study was newly developed, a verification study was done to ensure accuracy and repeatability of the data. The study involved comparing data from the PARTS-I against the existing CATS facility, which was designed to investigate both performance and noise on small-scale coaxial rotor systems [58]. The CATS stand serves as a reference against which to compare data from the PARTS-I to ensure the accuracy of our measurements. Since the CATS stand can only operate with ambient air conditions, all comparison data from the PARTS-I was also taken with the rotor operating in ambient air. All experiments in this study involve the rotor operating in a hover conditions; the rotor was driven by a motor in otherwise stagnant air, with no mean flow being produced by any of the wind tunnel facilities being used. The hardware used on the PARTS-I was then removed from the CAWT, and mounted in the open to rule out potential effects relating to confinement of the rotor's inflow or wake, and recirculation issues. Within the CAWT, the direction of the rotor wake was also switched, in order to rule out any effects of the structural elements of the rotor stand affecting the wake or inflow, as outlined in Fig. 3.1. The normal wake configuration shown in Fig. 3.1(a) was used for the compressed air testing outlined in § 3.1.3. In addition, comparisons

(a) Normal wake configuration.   (b) Flipped wake configuration.
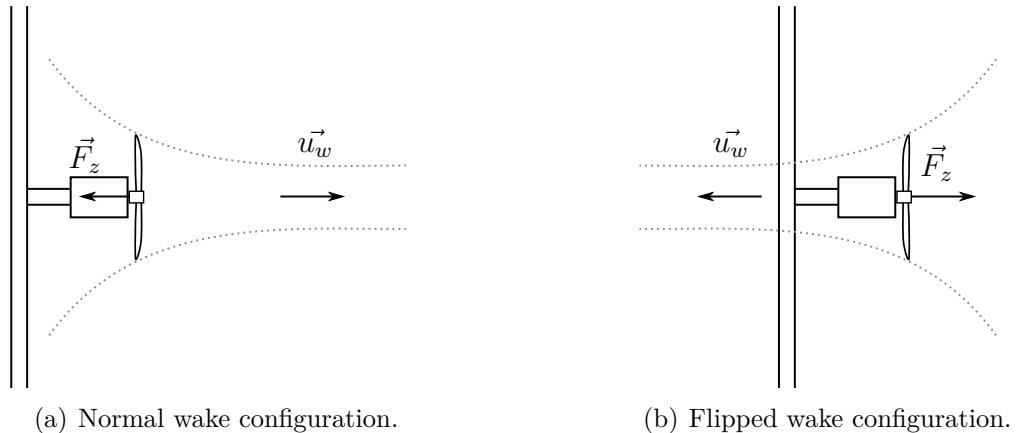
Figure 3.1. Illustration of the different rotor configurations examined in the verification study, indicating the orientation of the streamtube, and the direction of the wake velocity and thrust vector.

were made between the 3D-printed and stainless-steel rotor models on the PARTS-I, to ensure any differences in geometry did not significantly influence performance. For the duration of the verification study, the 3D-printed rotors were set to a collective pitch of 15°, as defined by the airfoil pitch angle at the 75% radial station, in order to match the geometry of the stainless-steel rotor. The 3D-printed rotor was used for the majority of the testing, and was the only rotor tested on all facilities.

The 3D-printed rotor was then tested in the PARTS-I, with the rotor oriented such that its wake was blowing away from the frame of the test stand, as shown in Fig. 3.1(a). This configuration most closely resembled that of the CATS from a geometric perspective, with the wake of the rotor blowing away from the measurement equipment, and being as unobstructed as possible given the available space. The same rotor was also tested facing the other direction in the PARTS-I, to quantify any changes in performance that might arise due to the test stand obstructing the rotor's wake or inflow. The 3D-printed rotor was then tested on the open-air rotor stand, in order to rule out any recirculation or wake confinement effects due to the enclosed aerodynamic environment within the CAWT in which the rotor was operating during the high-pressure tests. The open-air rotor stand allowed the rotor to operate in a much larger space than either the CATS or the PARTS-I, reducing the likelihood of the rotor's wake affecting its own inflow, or the wake being obstructed by a wall or other surface. Finally, the stainless-steel rotor was tested in the PARTS-I, exactly replicating one of the configurations in which the 3D-printed rotor was tested which allowed for a direct comparison between the two rotors.

3.1.3 Compressed Air Rotor Testing

The compressed air rotor tests exclusively used the stainless-steel rotor on the PARTS-I mounted within the CAWT. The rotor was oriented such that all of the test stand hardware were on the inflow-side, and nothing was obstructing the wake, as in Fig. 3.1(a). The test stand was positioned within the CAWT such that the distance to the beginning of the nearest elbow was approximately 12 rotor diameters, as shown in Fig. 2.3, providing ample room for the wake to avoid wake blockage or constriction effects as will be shown in the results of the verification study in § 4.3. After being mounted on the PARTS-I, the rotor blades were wiped with a lint-free rag soaked in a brake-cleaner solution to remove any contaminants or oils which may be on the surface. The CAWT's access port was then closed to prepare for pressurization.

The compressor system was activated to increase the static pressure to 8.5 atm gage pressure, in order to increase the density to be able to control the Reynolds number. After

reaching the target pressure, all valves were closed and the compressor was disengaged to allow the tank to maintain it's pressure. The load cell was then tared while the rotor was still, to account for the effects of the weight of the rotor, motor, and any other hardware mounted to the load cell. The rotor was then swept through a range of speeds, from approximately 1000 rpm to 5000 rpm. At each speed, a 20 s sample of all 6 force and torque components was collected at a rate of 40 kHz per channel. At the same time, data from the rotor speed sensor was sampled at 100 kHz. These datasets were displayed on the data-acquisition computer to monitor rotor performance in real time, and recorded to files for later processing. The on-screen display was used by the operator to visually determine when unsteady effects due to the ramping from one rotational speed to the next had subsided. Once the time series plot of load data looked sufficiently steady, acquisition was started, which automatically collected sample of the specified length. No closed-loop control of the rotational speed was available. The ESC was cycled through a number of preset command points, and the corresponding rotor rpm was measured, and displayed on screen along with the rest of the measurements.

Measurements of the ambient pressure and temperature in the CAWT were taken at the beginning and end of each rotational speed sweep and recorded to be able to precisely calculate the air density. Once a sweep of rotor speed at a particular pressure had been completed, the bleed valve on the CAWT was opened to allow the pressure inside to drop to the next point on the test matrix. Data was collected for pressure increments of 0.5 atm, from 2.5 atm to 8.5 atm, with one additional test at 1 atm. Data at pressures of 1.5 atm and 2.0 atm are not available, due to time constraints on the experiments.

3.2 Data Post-Processing

After the measurements were read in through the DAQ device, various computations were done to produce more meaningful representations of the data to analyze trends in the rotor performance. Some such calculations were done in real-time in the LabVIEW program used to collect the data in order to provide feedback to the experimenter, and others took place after the experiments were complete.

3.2.1 Rotor Performance Measurements

The raw data from the load cell consists of voltage measurements from the internal strain gauges. A LabVIEW Virtual Instrument provided by the load cell manufacturer was

used to convert these voltage values to force and torque measurements using the supplied calibration data. Each dataset spanned 20 s of measurement and was averaged to produce a single load value for each rotational speed. The averaged values of thrust and torque, which each aligned with one of the load cell axes of measurement, were used to calculate the thrust and power coefficient data discussed in § 4.5. The data are interpolated in order to obtain groups of data at constant Mach numbers, to facilitate analysis of any potential trends in rotor performance with variations in Mach number separate from changes in Reynolds number. More details of the interpolation process are provided in appendix C.

In addition to the measured performance data, estimates of the measurement uncertainty were also calculated for each data point, in order to produce the error bars and other uncertainty data discussed along with the experimental results. Details of the uncertainty analysis and the procedure for estimating the uncertainty can be found in § 2.4, with additional discussion of the load cell's measurement error given in appendix A.

The rotor speed measurement data is effectively a time series of single-bit digital data, the high and low states of which corresponded to whether or not a blade was detected in front of the sensor as each blade rotated through its field of view. This data was read in to LabVIEW as an analog voltage signal, and an edge detection algorithm was developed to calculate the rotational speed of the rotor real time. The calculated rotor speed data was also saved alongside the load cell measurements for later use in analyzing the data and generating plots.

Chapter 4 | Results

4.1 Overview of Results

This chapter includes a summary of the results of all the experiments conducted as a part of this study, including the verification of a new rotor testing facility at The Pennsylvania State University, the PARTS-I, and performance measurements on an isolated UAM rotor in hover over a range of ambient air densities. The results hereafter are divided into two sections; § 4.3 presents a verification study at atmospheric pressure outlining the ability of the PARTS-I to accurately quantify a rotor's performance, and § 4.5 outlines variations in a UAM rotor's performance with changes in the equivalent scale of the rotor. The latter experiments span an equivalent scale range from the model diameter of $0.36\,\mathrm{m}$ to the effective full-scale of a UAM vehicle rotor of $2.9\,\mathrm{m}$ in diameter.

4.2 Load Cell Accuracy Test

The ATI-Delta load cell is one of the main sensing elements in the PARTS-I; given its age and unknown history, it was decided to check the accuracy of its calibration. As discussed in § 3.1.1, the load cell's calibration was partially verified by loading it in both tension and compression to evaluate the response of the linear force axis used to measure thrust. Due to the limitations of the available testing equipment, accurate torque loading conditions could not be achieved, nor could combined loading conditions in which forces or moments are applied simultaneously on multiple axes. These sorts of multi-axis loading conditions typically lead to larger errors in measurement due to the coupling between measurement axes inherent in the design of the load cell, as was discussed in § 2.4, along with an explanation of how the measurement uncertainty values were determined. The

load cell was calibrated by the manufacturer using static loads of known magnitude, whereas in use for testing rotors the load cell is subjected to time-varying oscillatory loads over a wide range of frequencies. The dynamic response of the load cell was not considered during the calibration checks, and no data is available from the manufacturer on the transducer's response to oscillatory or time varying loading conditions.

With these caveats in mind, the testing that was accomplished with the load cell yielded good results; the measured loads correlated well with the reference weights used for calibration, and the load cell produced a linear response over a range from $-80\,\mathrm{N}$ to $80\,\mathrm{N}$, as shown in Fig. 4.1. The measured load along the z axis is plotted against the weight of the masses used in the test. A linear fit of the data gives a slope 0.989, with an intercept on the vertical axis of $-0.158\,\mathrm{N}$, with an RMS residual of $0.163\,\mathrm{N}$. This is almost an order of magnitude less than the nominal measurement uncertainty of the z axis load measurement of $\pm 0.99\,\mathrm{N}$. This apparent improvement accuracy is due to the loads being applied directly along a single axis, a condition for which the load cell's calibration data indicate a high degree of accuracy. The nominal value of $0.99\,\mathrm{N}$ is based on a condition where the load cell experiences loads of large magnitudes in multiple axes simultaneously, making it a very conservative estimate for this calibration test. The full details of the load cell's calibration data are provided in appendix A.

The load cell was mounted on the PARTS-I such that positive rotor thrust produced a negative reading for the force component along the z axis when the rotor was oriented with its wake blowing away from the rotor stand, as in Fig. 3.1(a). With the wake blowing towards the stand as shown in Fig. 3.1(b), the raw thrust measurement was positive. The latter configuration was only used in one of the test cases in the verification study. All of the data at varying pressures, which will be discussed in § 4.5, were acquired with the wake blowing away from the stand. All data presented in this thesis will be normalized such that both thrust and torque are positive, regardless of the sign of the actual load-cell measurements.

4.3 Rotor Stand Verification Study

The PARTS-I rotor stand was developed from the ground up to be able to test small-scale hovering rotors in the CAWT for this study. The verification study was designed to evaluate the accuracy and repeatability with which it could characterize the performance of a rotor. The details of this study and the test matrix involved are outlined in § 3.1.2. This section provides a comparison between data from the PARTS-I and the CATS
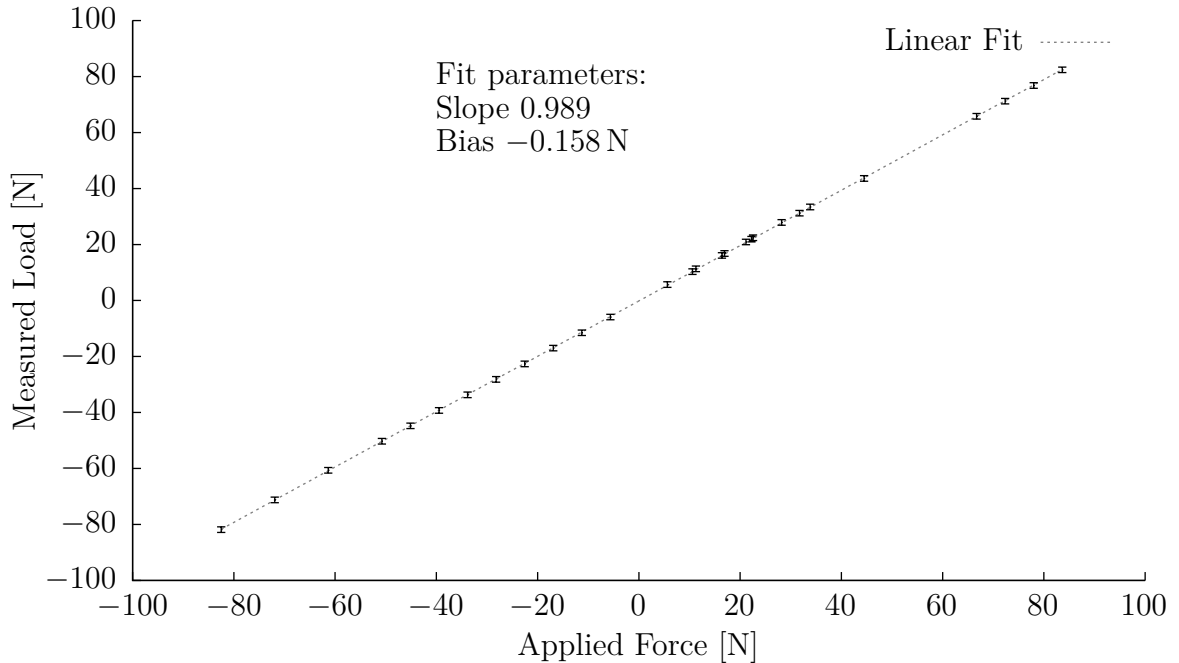
Figure 4.1. Force measured by the load cell for a series of static loading conditions along the F_z axis, which was used to measure the thrust produced by the rotor.

facility which will serve as a reference. It was chosen as a reference as it had been used for previous experimental studies involving rotors of approximately the same scale as the UAM rotor used in the current study [58]. A series of tests were conducted with the 3D-printed rotor, and the machined stainless-steel rotor on both the PARTS-I and the CATS. The raw performance data from the various configurations are plotted in Fig. 4.2, directly comparing all the test cases. The performance curves from the 3D-printed rotor operating in the CATS was then used as a reference to calculate deviation values for each of the other configurations, by simply interpolating the results from another test to the same set of rotational speeds as the CATS data, taking the difference between the two performance curves, and normalizing the result relative to the value observed in the CATS data for that particular test condition. These curves are plotted in Fig. 4.3, in order to more easily visualize the difference between the datasets as a function of rotational speed.

The thrust data shown in Fig. 4.2(a) aligns with the CATS facility to within the margins of experimental error. There is some overlap between the error bars of the data from the CATS stand, and the PARTS-I in each of its configurations. The open-air facility was the closest match to the CATS data, showing the smallest deviation across the range of rotor speeds tested. This can more clearly be seen in Fig. 4.3(a). The
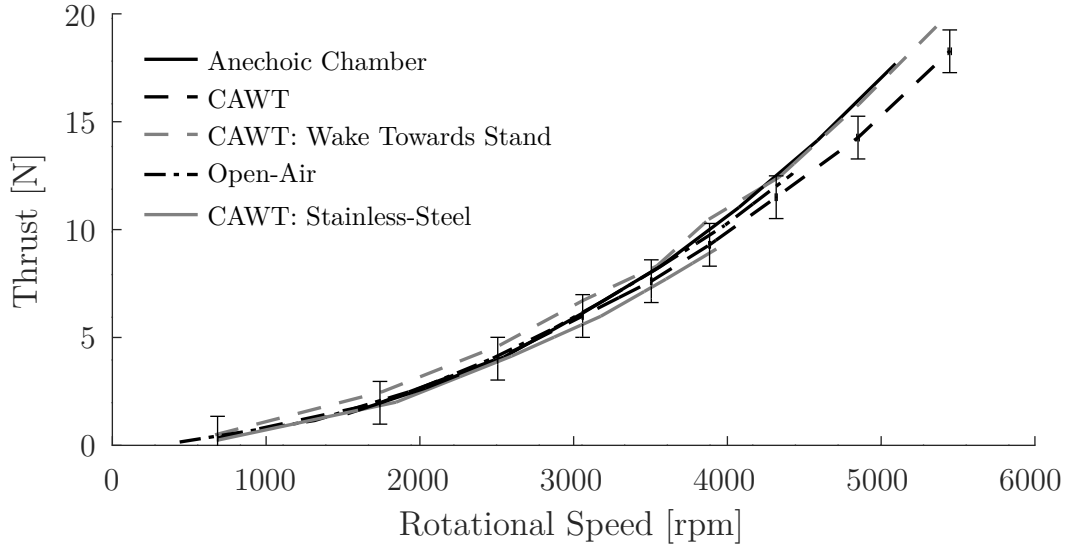
(a) Thrust profile for each of the configurations tested in the facility verification study.
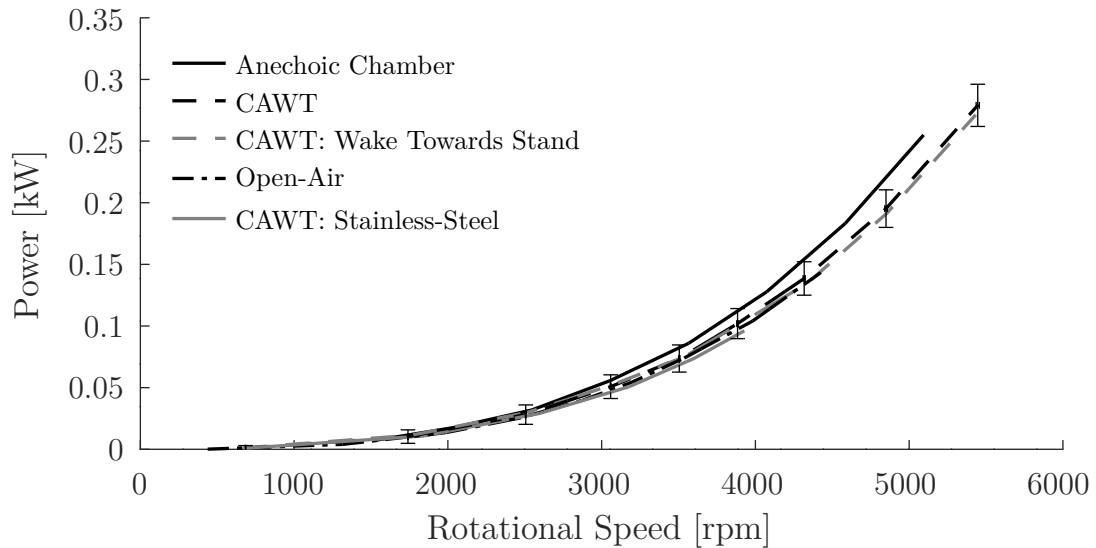
(b) Power profile for each of the configurations tested in the facility verification study.

Figure 4.2. Performance results from the facility verification study, including both thrust (a) and power (b), comparing the PARTS-I, the CATS, and the open-air rotor stand, as well as both the 3D printed and stainless-steel rotors.

power data, shown in Fig. 4.2(b), shows a different variation between the test cases than was observed in the thrust data, with less relative scatter between the new facility configurations. Fig. 4.3(b) shows that the power measurements from all the new facility and rotor configurations deviate from the CATS in a very similar way, and the differences between the power measured in the various new facility configurations is small relative
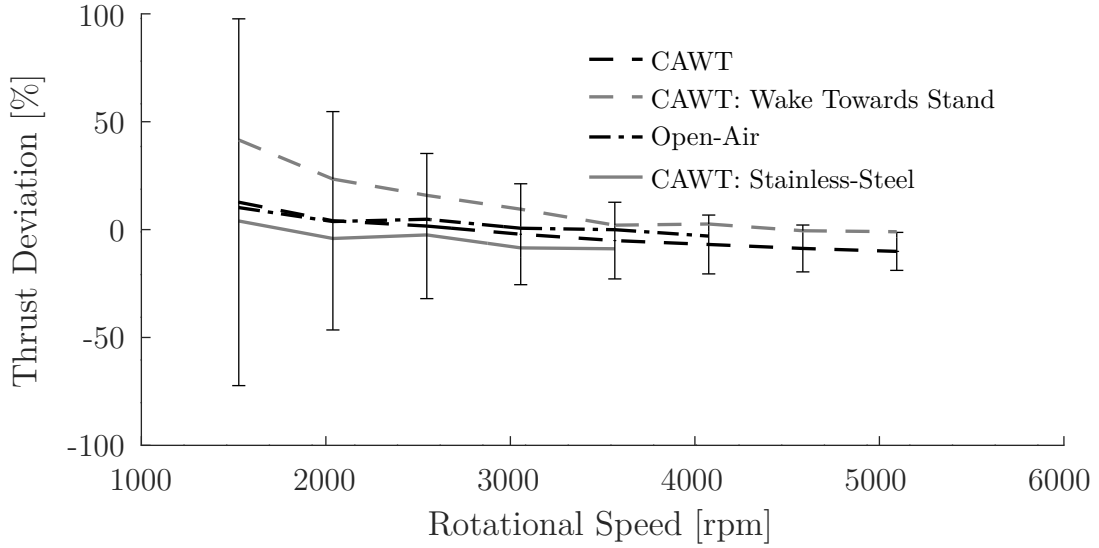
(a) Thrust measurements for each of the test cases in the verification study, expressed as a percent deviation from the magnitude of the data collected in the CATS facility.
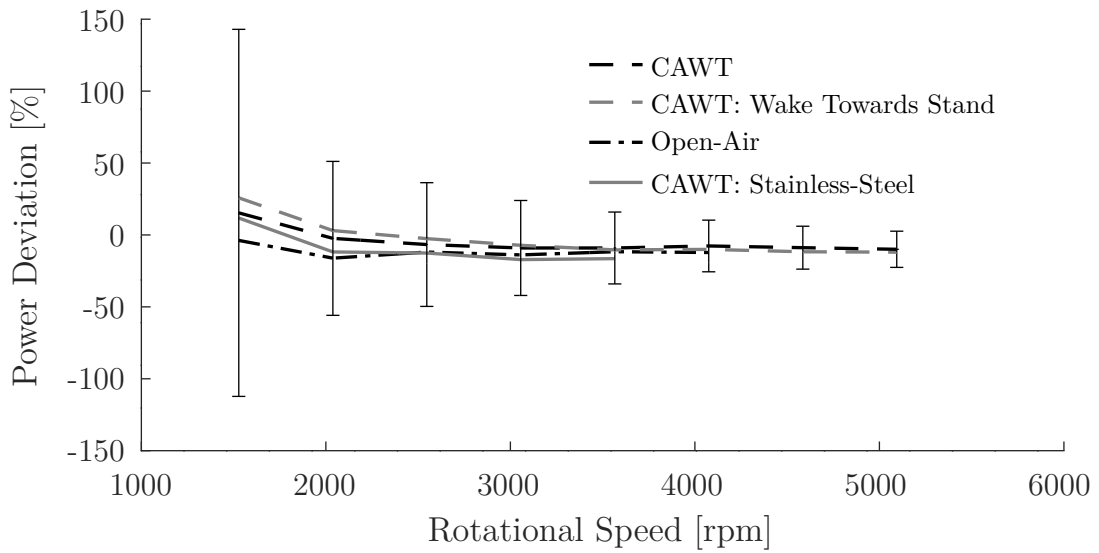
(b) Power measurements for each of the test cases in the verification study, expressed as a percent deviation from the magnitude of the data collected in the CATS facility.

Figure 4.3. Deviation of performance values for each case in the verification study, relative to the values from the CATS, showing both thrust (a) and power (b).

to the average deviation from the CATS stand, particularly for higher rotational speeds. The power measurements from the PARTS-I and the open-air stand deviate from each other by no more than 2.3%, which indicates good repeatability of the results. There is a wider spread in the thrust measurements, with the various configurations of the

PARTS-I deviating from each other by as much as 10%, although any differences are within the error bars associated with the measurement uncertainty of the load cell. The uncertainties present in this dataset are large in comparison to the magnitude of the loads being measured, with the measurements of thrust at lower rotational speeds being on the order of $1\,\mathrm{N}$, the same order of magnitude of the uncertainty on that measurement, of $\pm 0.99\,\mathrm{N}$. As density increases in the experiments described in § 4.5, the magnitude of the loads also increases while the absolute uncertainty remains the same. This results in much smaller relative error percentages of as low as 0.98% for thrust and 1.2% for power.

The fact that all the results from the verification study align within the margins of experimental uncertainty suggests that any possible aerodynamic confinement effects caused by the pressure vessel do not have a significant effect on the overall performance of the rotor. The open-air rotor stand provided a minimally-confined environment, with the rotor operating in a large indoor space containing otherwise stagnant air. It is hypothesized that the room was sufficiently large that any recirculation of the rotor wake back into its own inflow would be negligible, and so the space could be considered quasi-infinite. The CAWT, being a closed-loop wind tunnel by design, presents a more restricted environment, through which the wake produced by the rotor will circulate, potentially affecting its own inflow. Given that there is no significant difference between rotor power measurements in the open-air rotor stand and the PARTS-I mounted within the CAWT, it can be concluded that the effects of aerodynamic confinement are no greater than the error bars associated with these data. Quantitative data on the influence of the rotor's wake on its own inflow is not available, which is a shortcoming that will be discussed further in chapter 5.

The structural elements and instrumentation equipment included in the PARTS-I also have the potential to impose a blockage on the rotor's inflow or wake, which if severe enough, could affect the performance measurements. Such blockage effects should result in an increase in the spread of performance values between the different configurations. The blockage of the test stand would affect each of the configurations in a different way, and blockage effects should become more severe as the inflow or wake velocities increase. Such an effect was not observed, rather the opposite trend was seen. As rotational speed increased, the different configurations trend towards each other as seen in Fig. 4.3.

In addition to examining the repeatability of the experimental setups, the verification study data also provided some preliminary results to outline the behavior of the rotor in general. The thrust profile shown in Fig. 4.2(a) has a quadratic dependence on rotor speed, and the power profile in Fig. 4.2(b) has a cubic dependence on rotor speed. These

trends generally hold true for rotorcraft performance data, a trend which manifests itself in the definitions of the nondimensionalized thrust and power coefficients. These data show that the rotor is performing in accordance with typical theoretical predictions for rotorcraft behavior. This serves as another indicator that the PARTS-I is suitable for measuring the performance of a rotor, as it does not interfere with any important physical effects, and is able to characterize the resulting operational characteristics of the rotor.

4.4 Propagated Uncertainty in Thrust and Power Coefficient Data

After verification of the testing facility had been completed, performance data from the stainless-steel rotor operating in a range of ambient pressures from 1 atm to 8.5 atm, was analyzed. The densities observed correspond to a range of equivalent rotor scales from the physical size of the model, 0.36 m in diameter, up to 2.9 m, the size of the full-scale rotor after which the model was designed. Before attempting to analyze the data, however, an uncertainty analysis was performed to quantify the errors in the values of the thrust and power coefficients. The absolute thrust and power measurements are displayed over a range of rotational speeds and ambient pressure in Fig. 4.4. The error bars on these plots represent estimates of the uncertainty associated with the thrust and power data, the magnitude of which corresponds to the uncertainty estimates based on the predicted measurement error of the load cell as discussed in § 2.4.

For the smaller load magnitudes observed at lower ambient pressures and/or rotational speeds, the relative error expressed as a percentage of the measured load is on the order of magnitude of the load measurements themselves. As the ambient pressure or rotational speed increase, the measured loads increase, causing the relative errors to decrease. Each measurement of thrust and power was used to calculate a corresponding thrust coefficient and power coefficient, and the errors associated with the measurements were used to calculate a propagated uncertainty in the performance coefficient values. The resulting relative uncertainties are outlined in Fig. 4.5, expressed as a percentage of the magnitude of the respective performance coefficient for that particular measurement. The data are plotted in terms of the Reynolds and Mach numbers at which data was collected. The greyscale shade represents the relative uncertainty of a particular data point, and each set of points along a dotted line corresponds to a sweep of rotational speeds at a given ambient density. It was decided to restrict any further analysis to a subset of
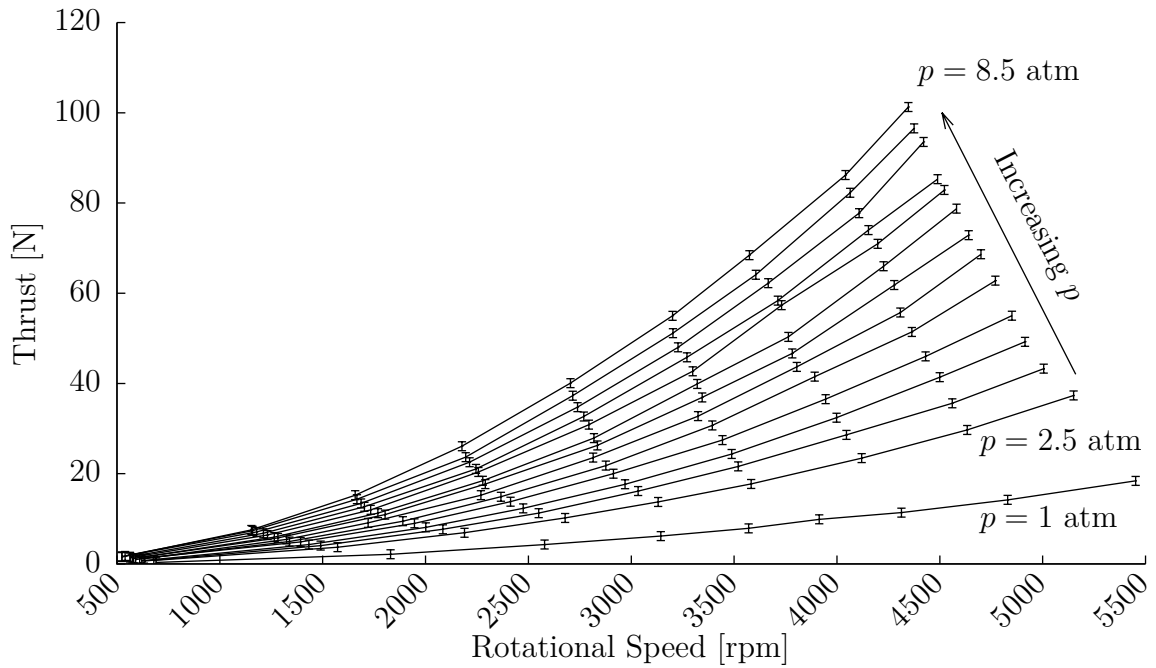
(a) Thrust profile.
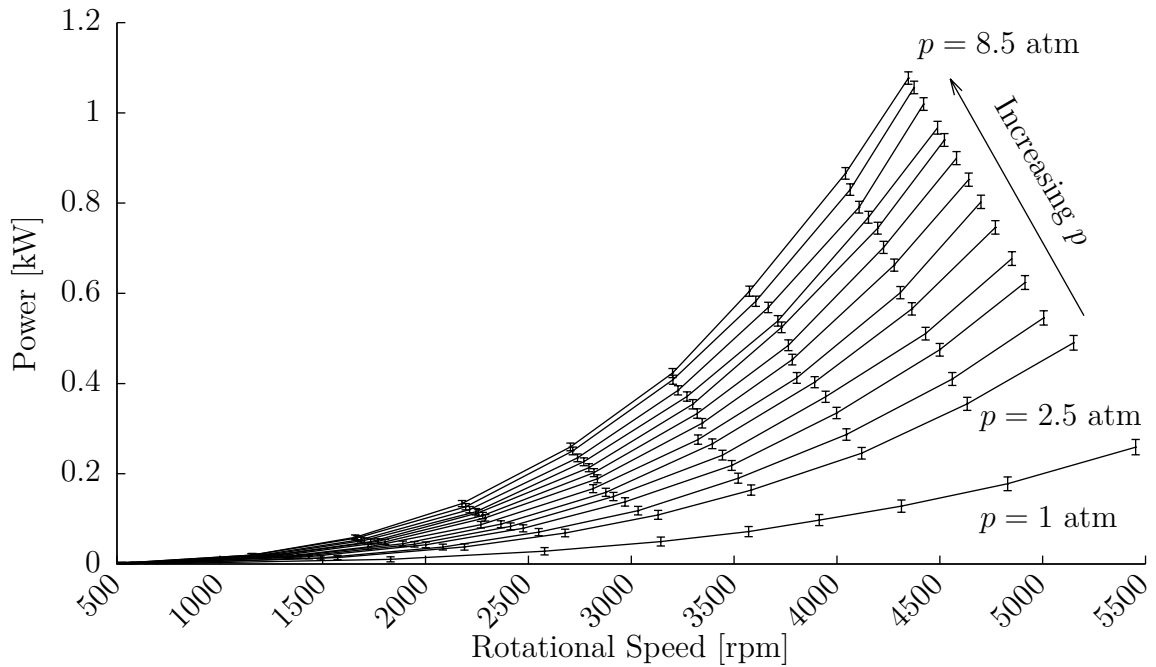
(b) Power profile.

Figure 4.4. Time-averaged performance data including thrust (a), and power (b) from the stainless-steel rotor tested under a range of rotational speeds and ambient pressures, with each line representing a constant ambient pressure, and therefore density.

the data for which the relative error was less than 10%, in order to ensure a greater degree of confidence in the results, and therefore the conclusions drawn from them. The data points for which the propagated error is less than 10% of the calculated thrust coefficient values are indicated in Fig. 4.5(a), and likewise for the power coefficient data in Fig. 4.5(b). The data points for which the uncertainty on the thrust and power coefficients are less than 10% are subsets of the available experimental data, with the latter being a more restrictive subset of the former. The data for which the uncertainty on the power coefficient was deemed acceptable will be used for any further analysis. This decision was made to ensure consistency between the different results and plots displayed, and focus on single set of data while maintaining acceptable uncertainty margins. As a consequence of this, the maximum error in the power coefficient data presented is larger in magnitude than that for the thrust coefficient data.

During the experiments, precise control of the rotational speed of the rotor, and therefore the tip Mach number, was not possible. In order to be able to quantify potential trends in the data with varying Mach number, the data needed to be interpolated to a series of constant Mach numbers. This was another factor that went into selecting the particular subset of data to use. It was desired that the interpolated data points maintain a relative error less than the specified value of 10%. Since the data was interpolated in Mach number, the upper Mach number bound was chosen to avoid extrapolating beyond the range of available data. The lower Mach number bound was chosen such that it was above the minimum Mach number for which data with an acceptable uncertainty was available, to ensure each resulting point was interpolated between two points with satisfactory uncertainty values. Based on the uncertainty data in Fig. 4.5(b), a subset of the data was selected including Mach numbers from 0.16 to 0.23, and Reynolds numbers from 1.75×10^5 to 5.75×10^5.

4.5 Performance Scaling

The raw performance results shown in Fig. 4.4 display the expected quadratic and cubic dependence of rotor thrust and power on rotational speed, but with the overall magnitude of the curves increasing with ambient density. This increase in magnitude with density is to be expected from a simple scaling analysis. Based on the BET analysis in chapter 1, thrust and power were shown to be dependent on the lift and drag coefficients of the airfoils which constitute the blades, as in Eqn. 1.12 and Eqn. 1.13. The lift and drag coefficients of a blade-element, defined in Eqn. 4.1 and Eqn. 4.2, normalize the lift and
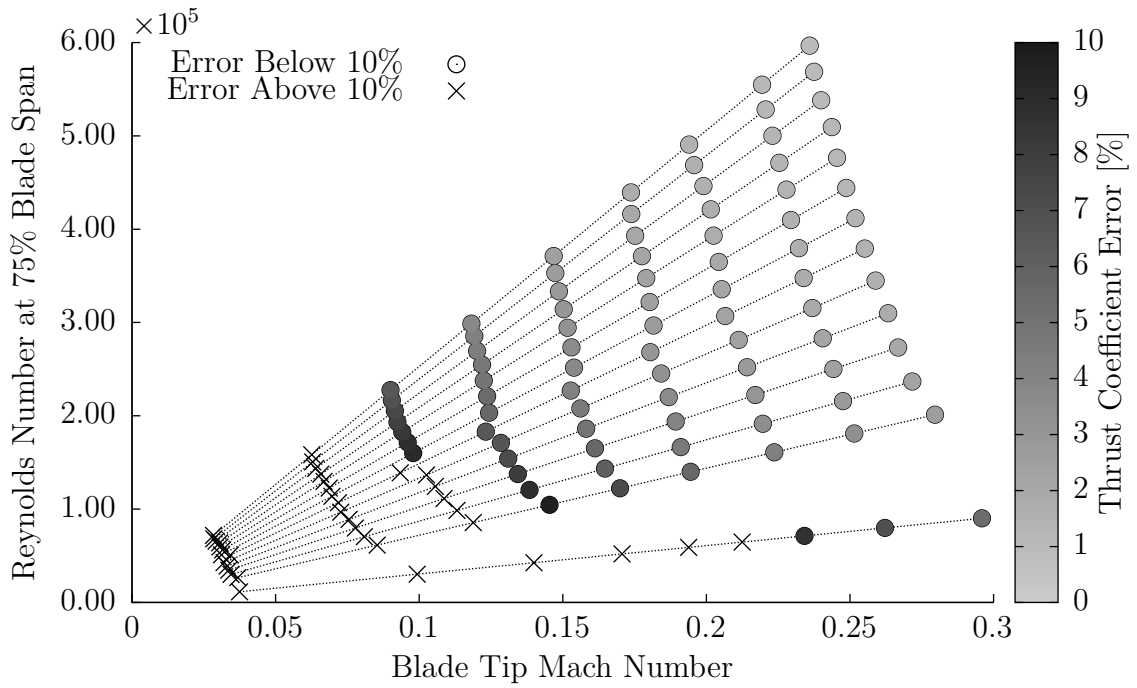
(a) Propagated uncertainty in the thrust coefficient.
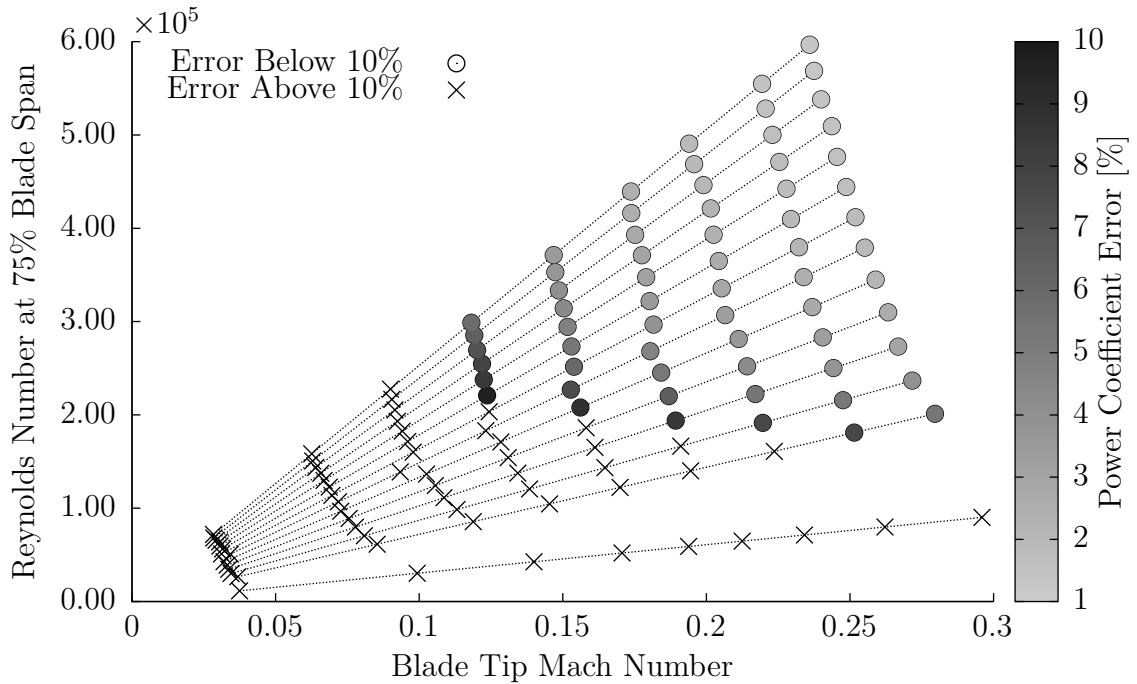
(b) Propagated uncertainty in the power coefficient.

Figure 4.5. A graphical representation of all the data points in the experimental test matrix, displaying the relative propagated uncertainty in the thrust (a) and power (b) coefficient values, expressed as a percentage of the magnitude of the respective performance coefficient.

drag produced by an airfoil in terms of a number of quantities, including the density.

$$C_l = \frac{L}{\frac{1}{2}\rho U^2 c \delta r} \tag{4.1}$$

$$C_d = \frac{D}{\frac{1}{2}\rho U^2 c \delta r} \tag{4.2}$$

As the ambient density increases, if the lift and drag coefficients do not vary significantly, the magnitude of the lift and drag forces will increase. As discussed in § 1.5.2, this assumption does not hold for large variations in Reynolds number. However, the variations in the lift and drag coefficients with Reynolds number would not typically be greater than a variation in density that caused a change in Reynolds number [26, 46]; a doubling of Reynolds number would not typically cause a doubling, or halving, of the lift or drag coefficient.

In order to more effectively analyze the variation in rotor performance as a function of Reynolds number, the data were then normalized into thrust and power coefficients, plotted in Fig. 4.6. The Reynolds number varies along the blade span due to the changing velocity and chord length, so the Reynolds number based on the properties at the 75% radial station was used as a reference value to identify each test point. This corresponds to the approximate spanwise location at which the Reynolds number reaches its maximum, due to the chord distribution of the particular rotor used. The data displayed are interpolated from that presented in Fig. 4.4 to create a series of datasets at constant rotational speeds, and therefore tip Mach numbers. In this case, the variation in Reynolds number within a constant-Mach number dataset is solely the effect of the change in density of the air in which the rotor is operating, as the relative velocity observed by the blade elements is proportional to the Mach number. These plots allow for visualization of the effects of Mach number and Reynolds number independently of one another. More detail on the interpolation and data reduction scheme is given in appendix C.2.

For the sake of improving legibility of the data in Fig. 4.6 and Fig. 4.7, some error bars were omitted from the plots. The error bars which are shown are representative of the predicted margins of error for the data in their immediate vicinity.

The plot of the rotor thrust coefficient in Fig. 4.6(a) displays a general increasing trend with Reynolds number, the linear fit results in a sensitivity of 1.7% increase in thrust coefficient for an increase of 1×10^5 in Reynolds number. This increase in thrust coefficient represents an improvement in the rotor's ability to produce thrust as the Reynolds number along the blade span increases. From this plot, there does not appear
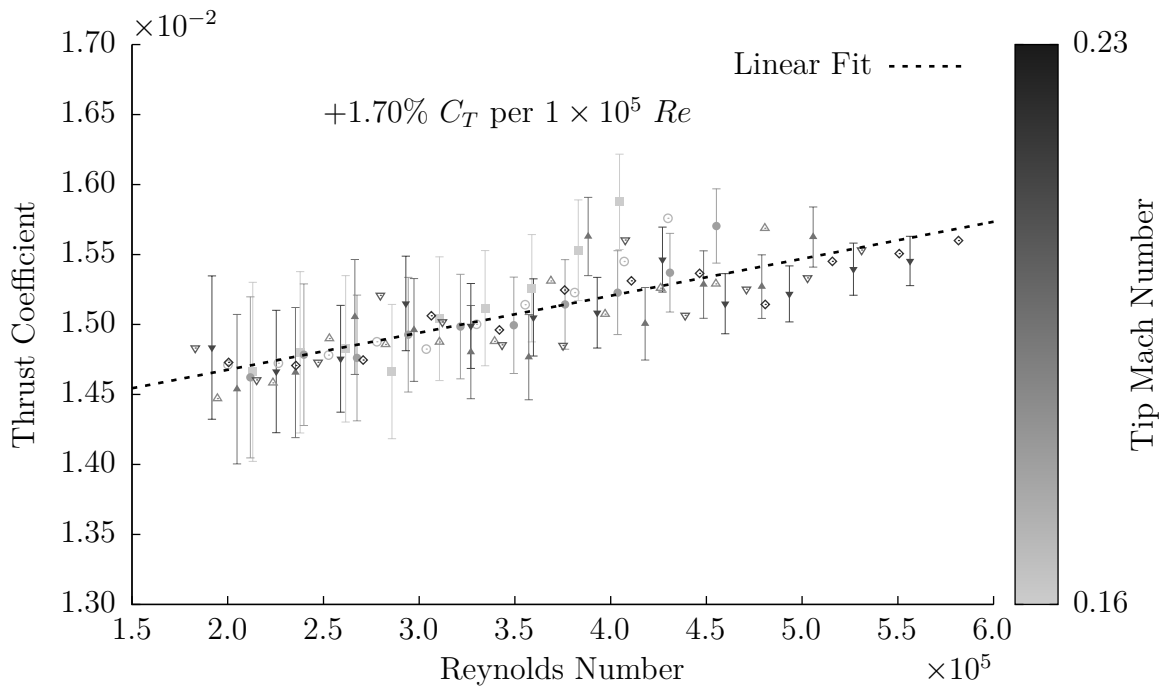
(a) Thrust coefficient.
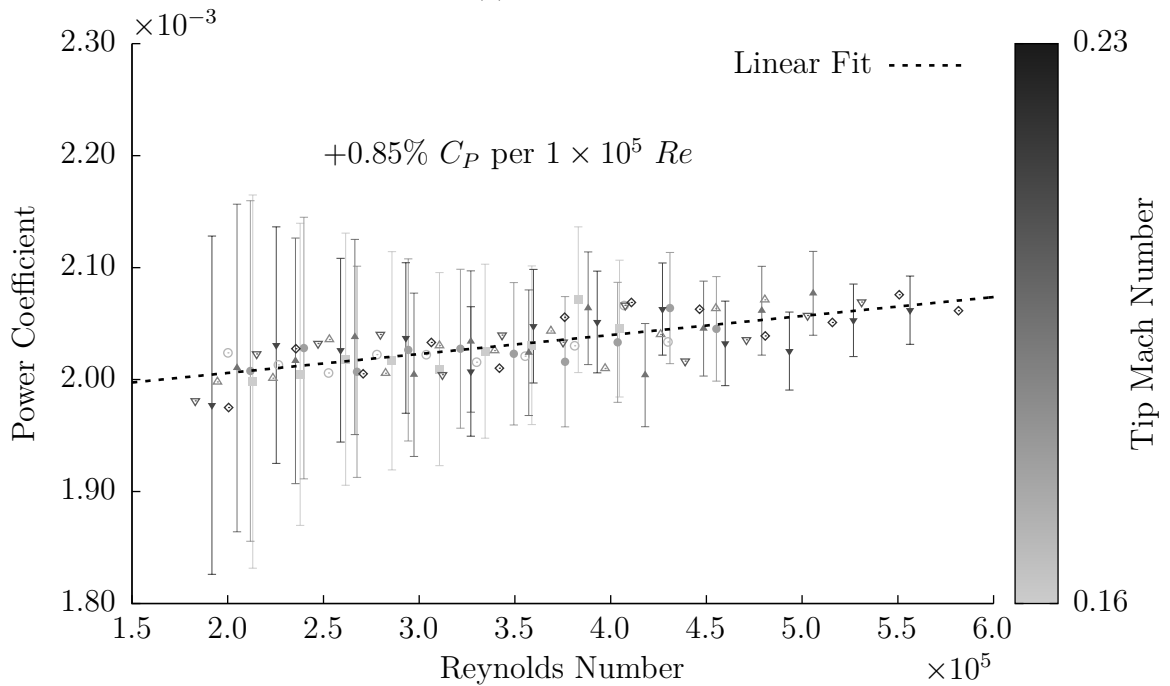
(b) Power coefficient.

Figure 4.6. Coefficients of thrust (a), and power (b) plotted as a function of Reynolds number, with each set of points corresponding to a fixed tip Mach number such that variations in Reynolds number along a given line are purely a function of ambient density.

to be a consistent trend of variation with the Mach number. Some of the lines at lower Mach numbers appear to spike upwards as the Reynolds number increases, but it is hypothesized that this is simply an artefact of the experimental uncertainty.

A similar plot for the power coefficient is shown in Fig. 4.6(b). This plot also displays an increasing trend with Reynolds number, albeit with a lower sensitivity of 0.85% per 1×10^5 Reynolds number. In addition, the error bars on this data are larger relative to the trends observed. This is due to the choice to use a fixed subset of the data for these plots, as described in § 4.4, which resulted in a larger maximum uncertainty in the power coefficient data than the thrust coefficient data. Despite the larger error margins, the data does suggest a general increasing trend in power coefficient with Reynolds number. This indicates the rotor is consuming more power relative to its effective scale as the density of the air increases. Because of the lack of more detailed data on the rotor aerodynamics, the exact source of the power increase cannot be determined conclusively. The induced drag, and therefore power must increase somewhat due to the rotor producing more thrust, although this effect would likely scale in proportion to the increase in density, producing no net change in the power coefficient. There may also be other effects at play including changes in the pressure drag caused by separated boundary layers, and skin friction drag due to turbulence, as will be discussed further in § 4.5.1.

Fig. 4.7 shows a plot of the ratio of the thrust and power coefficients, which can
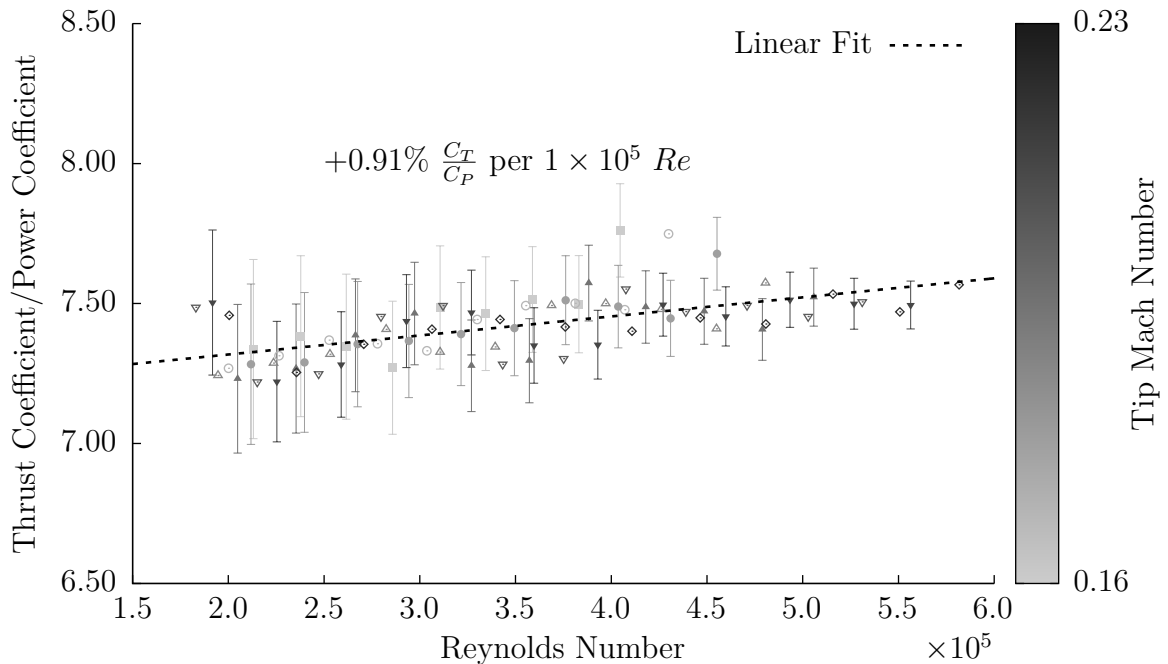
Figure 4.7. Ratio of thrust coefficient to power coefficient.

be interpreted as a metric for the overall efficiency of the rotor. Like the individual performance coefficient plots, an increasing trend is also observed, with an increase of 0.91% per 1×10^5 Reynolds number, indicating the efficiency of the rotor improves with increasing Reynolds number. This was to be expected from the data in Fig. 4.6(a) and Fig. 4.6(b), as the increase in the thrust coefficient was stronger than that in the power coefficient.

The figure of merit is a common metric for the hover efficiency of a rotor compared to ideal conditions. Fig. 4.8 displays the figure of merit for varying blade loading coefficients and Reynolds numbers. These data were interpolated from the experimental results to achieve groups at constant Reynolds numbers in order to attempt to highlight Reynolds number effects on rotor efficiency. Each data point for a given Reynolds number was interpolated from a dataset at a different ambient pressure, such that the product of rotational speed and ambient density was held constant. Variation in the figure of merit with changes in the thrust coefficient is expected, and indeed seen in these data, with increases as great as 25% for a 10% increase in the blade loading coefficient. The magnitude of the error bars on C_T/σ is on the same order as the variation in C_T/σ observed in the data.

Due to the relative scale of these error bars it is difficult to conclusively attribute the
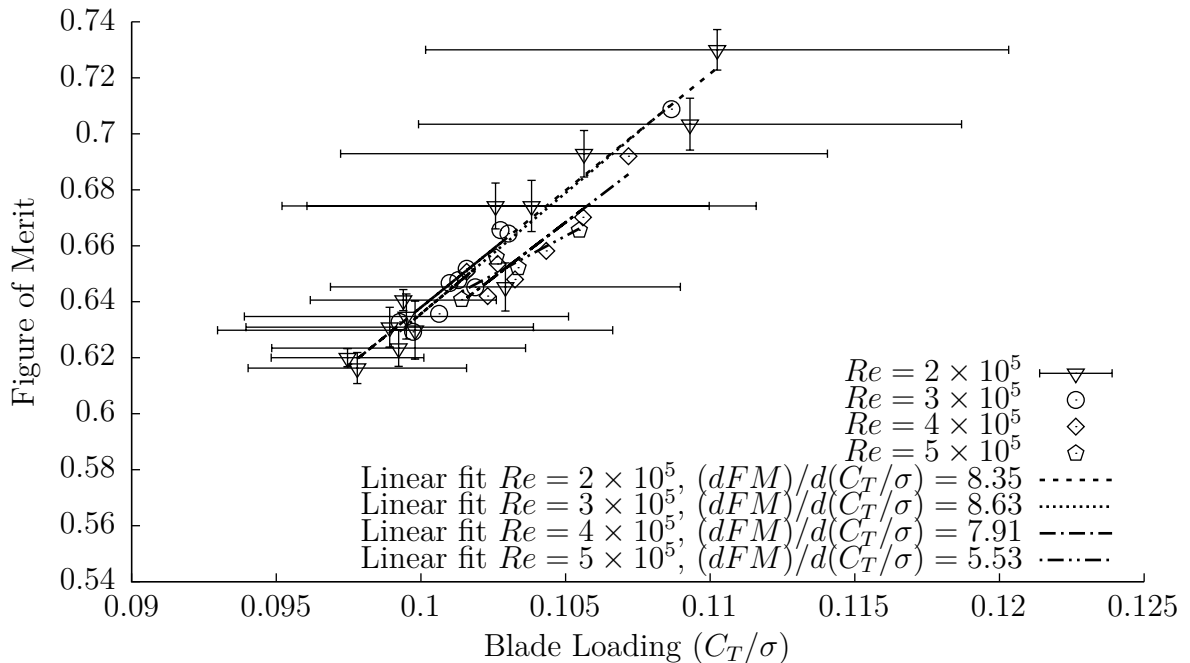
Figure 4.8. Figure of merit of the rotor over a range of blade loading coefficients, for various Reynolds numbers.

variation in FM to the change in C_T/σ, or to account for any difference as Reynolds number varies. Linear fits of the data are plotted for each Reynolds number, which appears to show a slight decrease in the figure of merit with increasing Reynolds number, though it is difficult to quantify from this plot. In addition, the datasets interpolated at the higher Reynolds numbers of 4×10^5 and 5×10^5 contain fewer points than those at lower Reynolds numbers. More data points in this range would help improve the confidence on the accuracy of the curve fits.

In an attempt to show the scaling trends more explicitly, the figure of merit data is also plotted as a function of the Reynolds number for various blade loading coefficients in Fig. 4.9. When represented in this way, the decreasing trend in figure of merit with Reynolds number becomes more clear. A linear fit of the data shows a 0.81% decrease in figure of merit for an increase of 1×10^5 in Reynolds number. This decrease in figure of merit appears at odds with the increase in the ratio of the thrust coefficient to power coefficient shown in Fig. 4.7, as both metrics effectively represent the efficiency of the rotor.
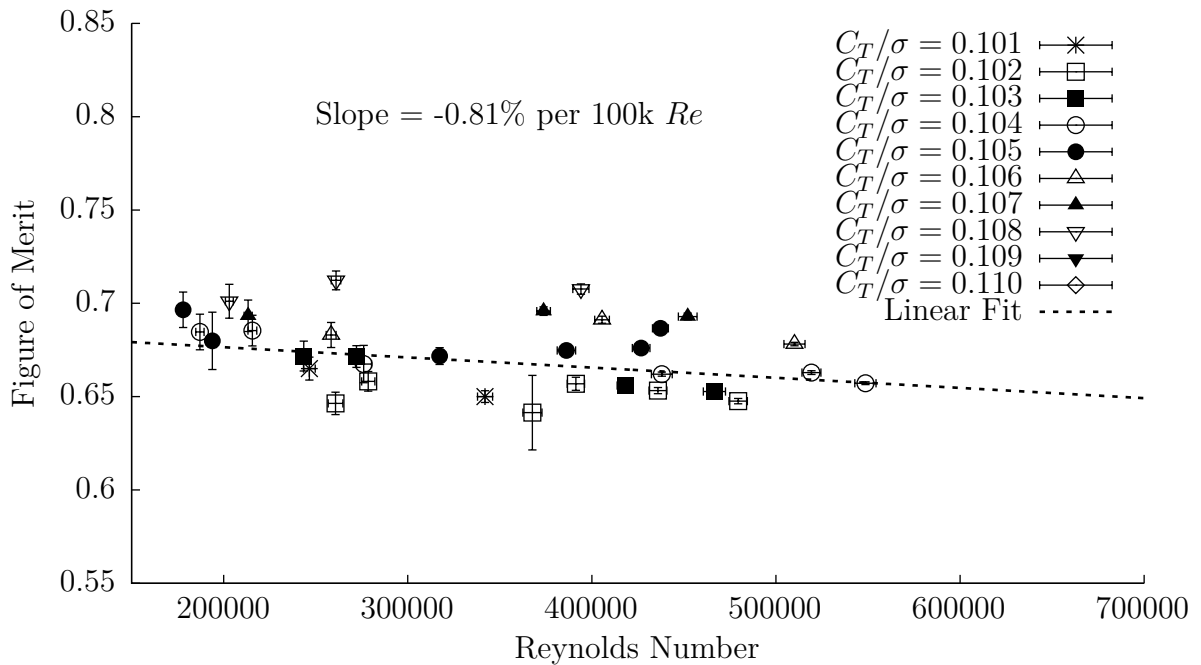
Figure 4.9. Figure of merit of the rotor over a range of Reynolds numbers, for various blade loading coefficients.

61

4.5.1 Predictions of Airfoil Boundary Layer Behavior

The only experimental data available to quantify the performance of the rotor are the force and torque measurements, and the rotational speed data. Detailed aerodynamic data along the blades and in the inflow and wake are not available, but predictions can be made for some of the more detailed phenomena based on analysis of the available data in combination with analytical tools such as airfoil theory and BET. Variations in the normalized rotor performance were observed as the Reynolds number changed. This indicates the performance of the rotor is linked to one or more aerodynamic phenomena with a dependence on Reynolds number, which vary in such a way that the rotor performance improves as the Reynolds number increases, at least over the range of conditions tested. Based on the discussion of § 1.5.2, this performance gain indicates an overall improvement in the average glide ratio of the airfoils along the blade span. The increase in thrust coefficient for a given Mach number indicates the rotor airfoils are producing more lift, and therefore the lift coefficient must be increasing. It is hypothesized that the increase in power is linked to the induced power increasing faster than the profile power is decreasing.

One possible explanation for this behavior is the behavior of the boundary layers on the blades, and the possibility of separated flow, either fully stalled or in the form of an LSB. LSBs can have strong effects on the aerodynamic behavior of an airfoil, especially at chord Reynolds numbers of less than one million [47]. For more aggressive angles of attack, or lower Reynolds numbers, the size of an LSB will increase, covering a larger portion of the chord [46]. A short bubble does not have a significant effect on the pressure distribution along the surface of the airfoil, with the exception of a small region local to the position of the bubble. The presence of a short bubble should not result in a significant loss of lift relative to an unseparated boundary layer [47, 48, 61]. Longer bubbles, or completely separated flow which does not reattach, can have a more significant effect on lift, drastically altering the pressure distribution along the upper surface [48, 61]. It is hypothesized that the improvement in performance of the rotor with increasing Reynolds number can be attributed to shortening of LSBs which are present along the rotor blade, or reattachment of completely separated flow. As the boundary layers begin to reattach and the severity of LSBs decrease, the lift penalty associated with these effects is reduced, causing the thrust coefficient to increase.

As discussed in § 1.5.2, the increase in power can be tied to an increase in the drag coefficient, an increase in the lift coefficient, or some combination of the two. The increase in thrust coefficient implies the lift coefficient of the rotor airfoils is improving, but what

cannot be determined conclusively is the relative influence of lift and drag on the overall power increase. The airfoil data presented in § 1.5.2 would suggest that the profile drag should decrease with increasing Reynolds number, at least in the vicinity of the 75% radial station where data was presented. However, the airfoil data shown is the result of a simulation using XFOIL, and may not perfectly represent the phenomena at play on the physical rotor model used in the experiments. Several factors which may not have been perfectly represented in the XFOIL simulations, such as the surface roughness, inflow conditions, and three-dimensional effects such as tip losses, could have caused the performance of the rotor to deviate from the simulation results.

The rotor's inflow can affect its performance in a number of ways. The turbulence intensity of the incoming free-stream air can have a considerable effect on the performance of an airfoil section, and the rotor as a whole. XFOIL accounts for this by means of the e^N transition prediction method, for which a single parameter, N_{crit}, is used to specify the rate of amplification of instabilities which result in transition to turbulence [62]. The simulations presented here used a value of 9 for N_{crit}, which is common though not necessarily correct in all cases. Smaller values of N_{crit} correspond to more incoming turbulence, and faster transition, while greater values correspond to flow which is like to remain laminar longer. An inappropriate choice of this value would produce a shift in the resulting airfoil stall characteristics similar to a change in Reynolds number as observed in Fig. 1.2 and Fig. 1.3. In addition, the inflow may contain larger-scale unsteady flow structures resulting from aerodynamic interactions with the hardware supporting the rotor, or the rotor ingesting the remnants of its own wake which may have recirculated around the loop of the wind tunnel. XFOIL simulations are by nature two-dimensional and steady ant thus could not account directly for unsteady effects, which often involve three-dimensional vortex structures as well. There is no data available to quantify unsteadiness or turbulence intensity in the rotor inflow, though it is hypothesized from the results of the verification study presented in § 4.3 that any such effects would not affect the rotor performance significantly.

The increase in power coefficient observed in the experimental data could also be explained by other aerodynamic effects. As the Reynolds number increases, the boundary layer becomes more prone to transition, leading to the onset of turbulence sooner after separation occurs, or even before the boundary layer separates in the first place. This increase in turbulence in the boundary layer leads to an increase in skin friction drag [46]. Short separation bubbles will affect the drag and consequently the power consumed by the rotor by causing the boundary layer to transition from laminar to turbulent, after the

initial separation point [47,48,61]. An increase in the Reynolds number has the potential to shift the point of transition towards the leading edge, by one of two main mechanisms. Higher Reynolds numbers typically result in the location of an LSB moving closer to the leading edge of an airfoil [47], and can also cause the boundary layer to transition before an LSB has the chance to form [44,46]. A shift in the transition location to a point further upstream will result in an increase in skin-friction drag, but potentially a reduction in pressure drag due to less severe boundary layer separation effects. The observed increase in power suggests that any affects causing drag to increase dominate those which work to decrease drag. It is possible such an interaction between the decreased severity of pressure drag from LSBs along the blade, and increased skin-friction drag could be responsible for the increase in power.

While useful for providing some insight into the physical phenomena at play, the simulated airfoil data cannot conclusively prove the aerodynamic behavior of the rotor. Ultimately, more detailed information on the aerodynamics at play will be required to draw any definitive conclusions about the cause of the increase in the thrust and power coefficients of the rotor. Even data on the rotor inflow and an accurate characterization of the roughness of the airfoil surface could better inform a series of simulations which could characterize the rotor behavior with greater confidence, and provide more insight into the source of the changes in rotor performance. Some characteristics of airfoil performance are likely to remain similar, at least over a portion of the operating space, such as the existence of an LSB, and the general changes in its behavior with Reynolds number.

The pressure distribution on the surface of an airfoil can provide information about the presence and characteristics of an LSB. Fig. 4.10 and Fig. 4.11 displays the variation in surface pressure coefficient distribution along the airfoil at the 75% radial station, for a range of Reynolds numbers from 2×10^5, to 5.6×10^5, at selected angles of attack. The pressure coefficient, defined in Eqn. 4.3 is often used as a means to describe the variation in pressure along the surface of an airfoil relative to the free stream static pressure The subscript ∞ denotes the specified quantity is in reference to the undisturbed free-stream medium. Some of the data show a prominent plateau in the pressure coefficient plots, which indicates the presence of an LSB [47]. The sharp increase in pressure after the plateau indicates the location of turbulent reattachment. While not necessarily an exact representation of the behavior of the boundary layer on the rotor in these experiments, the simulation data provides insight into the general trends and physical phenomena which may affect the performance of the rotor.
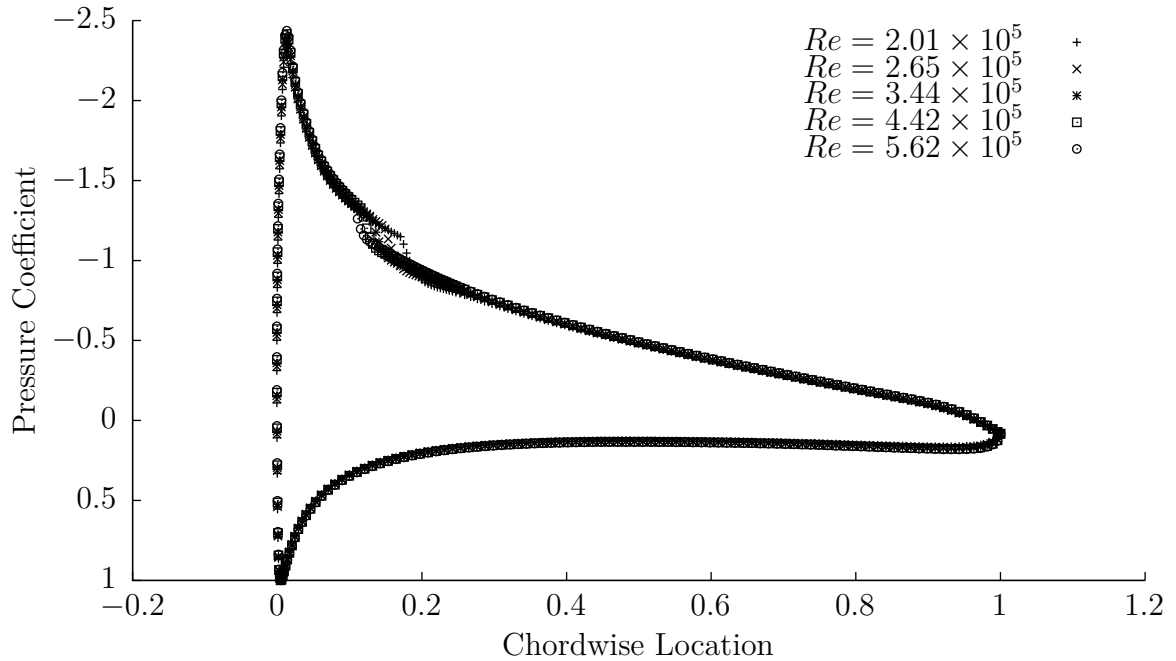
Figure 4.10. Surface pressure coefficient distribution for the airfoil at the 75% radial station, at an angle of attack of 5°.

$$C_p = \frac{p - p_\infty}{\frac{1}{2}\rho_\infty V_\infty^2} \tag{4.3}$$

The plots of the pressure coefficient along the airfoil surface indicate that at low Reynolds numbers, an LSB may be present on the rotor even at angles of attack of 5°. Given the collective pitch setting of the rotor blades at 15° and the linear twist variation of 34° from root to tip, it is hypothesized that the resulting angles of attack on the blade are such that LSBs are present over a portion of the blade span.
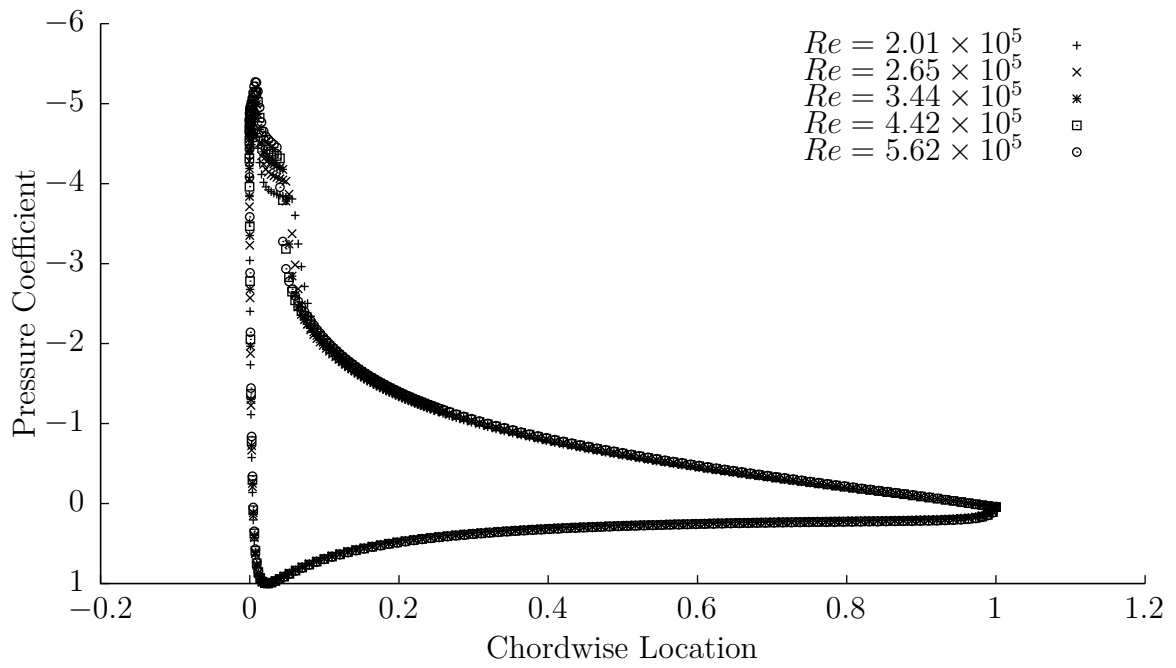
Figure 4.11. Surface pressure coefficient distribution for the airfoil at the 75% radial station, at an angle of attack of 10°.

66

Chapter 5
Conclusion

This chapter will provide a brief summary of the results presented in chapter 4, outlining the overall scaling behavior seen in the experimental data. Some discussion will also be presented on the broader implications of this work, and its potential impacts in academia and the rotorcraft industry. Lastly, recommendations for improvement to the present experiments will be given, as well as some suggestion of next steps to be taken.

5.1 Summary of Rotor Scaling Trends

The results presented in chapter 4 clearly demonstrate that the performance characteristics of a rotor can be a function of the Reynolds number at which the rotor is operating. Due to the relative changes in Reynolds number and Mach number when attempting to study the performance of a rotor using a small-scale experimental model, they cannot both be replicated simultaneously while testing in ambient air. This will ultimately lead to differences between the model-scale and full-scale aerodynamic behavior. By conducting experiments with a rotor inside a compressed-air environment, the density can be adjusted in order to more closely match both the Reynolds and Mach numbers to the desired full-scale conditions, leading to more accurate replication of the physical phenomena of interest.

The data in this study displays variations in performance which could have a meaningful impact on the accuracy of an experiment, and the validity of the results derived from it. For the rotor geometry and conditions tested, an increase in Reynolds number of 1.0×10^5 resulted in an increase in the thrust coefficient of 1.7%, and an increase in the power coefficient of 0.85%, corresponding to an overall improvement of efficiency, as quantified by the ratio of C_T/C_P. When considering the design of a vehicle, a difference in thrust as seemingly small as 1.7% can be detrimental to its ability to perform its task

or mission. A 1.7% decrease in thrust can limit the gross takeoff weight of a vehicle, reducing its capacity to carry passengers or cargo. Likewise, an under prediction of power during the design stage can result in the finished vehicle underperforming in terms of efficiency, range, or maneuverability. If the difference in Reynolds number between the experimental model and full-scale vehicle is greater, an even stronger impact on the performance would be observed. If a faulty experiment leads to an inaccurate estimate of a vehicle's performance early on in the design process, it can result in increased costs as preventable design iteration is required, or even outright rejection of a design candidate which may have been feasible. Worse still, if the performance of the system is over-predicted by an experiment, it may lead to a vehicle being put into production or use which cannot achieve the performance characteristics expected of it, which could pose a significant safety risk to those in or around the vehicle during flight.

Conversely, the ability to more accurately characterize the performance of a vehicle based on testing of small-scale models in compressed air could revolutionize the design process of rotary wing aircraft. This is especially true for new or unusual design concepts for which there may not be enough representative full-scale experimental data available to validate analytical or numerical models. Compressed-air scale-model testing is a novel experimental technique in the context of rotary wing aerodynamics. Further development of this method has the potential to facilitate more rapid and cost effective innovation in this industry, as well as unlocking new experimental capabilities from an academic research perspective. In order to reach this stage, more experimentation and validation is required. The work discussed in this thesis represents an important first step in the ability to more accurately replicate full-scale aerodynamic effects on a small-scale model.

On rotors for which the flow can safely be assumed to be incompressible, the Reynolds number is one of the dominant factors influencing rotor performance, and rotors of different scales have been shown to exhibit the same performance at the same Reynolds numbers. The stainless-steel rotor which was used to collect the main experimental data was designed not only to be able to withstand the increased loading due to the high density, but to do so with minimal bending or deflection. The rigidity of this rotor allows for the ruling out of any aeroelastic effects on performance, and puts the focus on pure aerodynamic changes with Reynolds number.

5.2 Future Work

The results presented in chapter 4 display a definite trend of rotor performance with Reynolds number, but there is still room for improvements to be made. Such improvements include the accuracy of the instrumentation equipment used, improvements to the rotor models and/or additional testing hardware, and adding the capability for more types of measurements to the system.

5.2.1 Improvements to Experimental Setup

The large error margins on the performance data discussed in chapter 4 outline the need for better experimental accuracy in order to conclusively analyze trends in the data, particularly for the cases of low Reynolds and Mach numbers where the relative effects of the uncertainty are much more significant. A new load cell has been acquired which will enable measurements with lower absolute error, allowing more accurate data to be collected for conditions of lower thrust and power. No single load cell will be able to achieve the accuracy required for use over such a large range of ambient densities, so the test equipment must be somewhat modular to allow for the most appropriate transducer to be used under any given condition. In addition to using more accurate sensors, the relative uncertainty can be reduced by increasing the magnitude of the loads being measured. Future experiments will involve ambient densities even greater than those achieved in the present study, making full use of the CAWT's 34 atm pressure capability. This will lead to larger Reynolds numbers, but also increased forces and moments on the load cell.

Larger load magnitudes could also be achieved by using a larger diameter rotor, which would have the effect of increasing the thrust produced for a given test point, defined by a fixed Reynolds and Mach number. By rearranging the equation for the thrust coefficient, as defined by Eqn. 1.2, and substituting in the definition of the Mach number $M = \omega R/c$, Eqn. 5.1 can be obtained.

$$F_z = \frac{\pi}{2} C_T M^2 c^2 \rho R^2 \tag{5.1}$$

If the Reynolds number is held constant as the rotor radius R increases, the density must change with inverse proportionality to the change in radius, leading to a linear dependence of thrust on the rotor radius, as Reynolds and Mach numbers are held constant, assuming the thrust coefficient does not change appreciably. In this case, the

true thrust coefficient should remain constant, as the geometry of the rotor and the Reynolds number at which it is operating are being held fixed. Any apparent changes from such an experiment would be due to the increased accuracy of measurement. The same logic applies when considering the power coefficient, but with an even greater effect. By using substituting the definition of the Mach number into Eqn. 1.3 as done before with the thrust coefficient, and using the definition of power, $P = M_z\omega$, Eqn. 5.2 can be obtained, which describes a similar expression for the shaft torque as a function of rotor scale.

$$M_z = \frac{\pi}{2}C_P M^2 c^3 \rho R^3 \tag{5.2}$$

The difference here being the effective quadratic dependence of torque on rotor scale, due to the aforementioned inverse relationship between density and rotor scale in order to maintain a constant Reynolds number. The error margins on the power coefficient data were considerably worse than that of the thrust coefficient data, so this quadratic dependence of torque on rotor scale provides a strong incentive to increase the scale of the rotor used in an experimental study.

The suggestion of increasing the scale of the experimental models may seem to contradict the purpose of this work, but the author believes it simply outlines the need for careful design of an experimental study to ensure the experiments being conducted can provide sufficient data to analyze the desired phenomena. The uncertainty on the load measurements in this study is higher than would be desired, partly due to the sub-optimal choice of measurement equipment. The load cell used had a larger measurement range than was necessary, and as is often the case with transducers, a trade-off must be made between range and resolution. A load cell with a finer resolution could improve the accuracy of measurements significantly. In order to further improve the accuracy of the data, of future studies, the author suggests the use of multiple load cells with different ranges, and therefore resolutions, to acquire sufficiently accurate data over the entire desired range of operating conditions. The conditions for which the uncertainty will likely continue to be unacceptably high represent the operational edge-cases of a realistic rotor design. Vehicles are unlikely to operate with Reynolds numbers and Mach numbers in the low range of these data, as typical in-flight Reynolds numbers for helicopters tend to be on the order of several million. For UAM configurations with smaller rotor diameters and chord lengths, Reynolds numbers may drop to below one million but will still be considerably higher than those observed on the small-scale models in atmospheric air.

As discussed in chapter 4, the mean values of the measurements converged well within

the samples of data available, but some of the variances did not, alluding to potential issues with resonance, or aerodynamic unsteadiness. Additional analysis of the testing equipment can be performed to better quantify its resonant modes and frequencies, and the data can be sampled for longer periods of time to improve the ability for the statistics to converge. Further study into the optimal design of the PARTS-I, as well as testing methodology to ensure sufficient data is recorded in real time is warranted. More detailed aerodynamic data, such as measurements of the inflow or wake profile and the flow induced by the rotor which then recirculates through the loop of the wind tunnel, may also be helpful in diagnosing the cause of the issues.

5.2.2 Future Validation Experiments

In order to better quantify the scaling behavior of the performance of the rotor, and the ability to achieve accurate scaling by matching the Mach and Reynolds numbers, accurate full-scale performance data will be required for validation purposes. A full-scale rotor 2.9 m in diameter has been tested in a wind tunnel in hover as well as forward flight over a range of velocities and incidence angles. Once available, this data will be used for comparison against the data from the CAWT, at ambient densities which produce Reynolds numbers equivalent to the full-scale operation.

In addition to experimental data, a numerical Blade Element Momentum Theory solver is being developed to provide numerical performance predictions, and compare the scaling behavior seen experimentally to that from the computational results. In order to account for the differences in rotor scale, airfoil polar data will be required at a range of Reynolds and Mach numbers, to form a lookup-table that can be used to interpolate airfoil data based on the actual conditions computed by the solver.

5.2.3 Additional Scaling Behavior of Interest

The structure and behavior of the rotor's wake can have a significant influence on it's overall performance, as the vortex structure can affect the inflow and bringing about the potential for interactional effects. The vortex dynamics in the wake are the main mechanism for coupling the aerodynamics between multiple rotors, or a rotor and some other body such as a wing or fuselage, or the ground. More detailed data on the behavior of the wake over a wide range of Reynolds numbers would provide insight into more complex scaling behavior which performance measurements alone cannot.

Given that analytical models to quantify interactional aerodynamic effects involving

multiple rotors are not as well established as models for isolated rotors, building on the current study to include multirotor configurations could provide valuable data to future model designers and experimentalists alike.

5.3 Concluding Remarks

One of the major benefits of small-scale testing is that the vastly reduced cost of experiments can be taken advantage of to investigate complex systems earlier on in the design phase. Accurate and meaningful experimental data can be collected to inform design choices with greater confidence and lower risk. The current boom in multirotor aircraft development brought on by the eVTOL and UAM markets represents one possible use of this new testing method, as it would allow for more rapid and ambitious innovation. The results of this study have added to the wealth of information available establishing a link between a rotor's performance and the Reynolds number at which it is operating, outlining the need to accurately replicate full-scale physical behavior in an experimental model. In addition, this thesis provides a proof of concept for a new experimental method for quantifying rotor performance which has great potential for utility in future studies.

Appendix A
Load Cell Measurement Error Data and Experimental Uncertainty Estimation

This appendix will provide a quantitative characterization of the load cell's measurement error resulting from testing done by the manufacturer, along with information about how these data were used to estimate the uncertainty associated with the rotor performance data discussed in the results of this study.

A.1 Quantification of Measurement Error

Load cell: talk about calibration data, dependence of uncertainty on loading conditions, validity of assumption that it's constant.

The load cell's manufacturer conducted a detailed calibration of the transducer, by subjecting it to a series of single-axis and multi-axis loading conditions. This allowed the accuracy of the device to be evaluated over a range of conditions the device may encounter during what the manufacturer anticipates to be normal use. The uncertainty data is specified as a percentage of the maximum rated load for each axis of the transducer. These maximum loads are given for reference in table A.1.

F_x	F_y	F_z	M_x	M_y	M_z
330 N	330 N	990 N	30 N m	30 N m	30 N m

Table A.1. Maximum rated loads for each force and moment axis of the load cell used in this study.

The measurement error is defined as the difference between the actual load applied to

the transducer and the reported measurement. This difference depends on the specific loading condition being applied, due to the coupling between the different measurement axes inherent to the design of this type of transducer. The manufacturer specifies a measurement uncertainty of 1.25% of the maximum rated load of each axis, with a 95% confidence level. The rotor loads measured in this study involve magnitudes much less than the rated limits of the load cell, and are so comparatively small that the load cell manufacturer's nominal uncertainty values are unacceptably large. 1.25% of the z axis force measurement is 12.4 N. This would result in a relative uncertainty of between approximately 12% to 150% for the range of thrust values observed in the present study. The full test matrix of loading conditions evaluated is provided in table A.2, and the resulting measurement errors are provided in table A.3. By examining these data in more detail, it can be observed that the actual measurement errors seen over much of the calibration were far smaller than 1.25%, often on the order of 0.05%.

The manufacturer includes a note stating that the actual uncertainty in a given application is likely to fall somewhere between the data listed in table A.3 and the nominal value of 1.25%. In addition to this disclaimer, a number of other factors may influence the accuracy of the provided calibration data. The loads applied during the manufacturer's testing are static loads, while the present experiments by nature subjected the load cell to oscillatory loads with harmonic content over a range of frequencies. The validity of the calibration under these conditions is not known, as no data is provided for the load cell's behavior under vibrational loads. It is assumed that the influence of vibration is small, due to the oscillatory component of the loads typically being smaller than the mean values. In addition, none of the calibration test cases outlined in table A.2 involve simultaneous loading on the two main axes of interest for this study, F_z which was used to measure thrust, and M_z which was used to measure torque. However, the relative influence of these axes on one another does not appear to be large from the data in table A.3. The maximum thrust measured is on the order of 100 N, and the maximum torque 0.3 N m. These values are considerably smaller than the 889 N and 19.8 N m applied to the F_z and M_z axes respectively during calibration. Any effect on the error due to cross coupling of these axes is therefore hypothesized to be at most equal to the values available in table A.3.

A.2 Estimating the Load Cell's Measurement Error

The measurement error values reported in table A.3 range in magnitude from $0.00\,\%$ to $0.39\,\%$, depending on the applied loading conditions. In order to estimate a more appropriate value for the measurement error, reasoning was used based on the particular loading conditions seen during experiments, and the caveats discussed in § A.1. The largest force observed during experiments was the rotor thrust, a force along the F_z axis which ranged from approximately $1\,\mathrm{N}$ to $100\,\mathrm{N}$. Likewise, the largest moment was the rotor torque on the M_z axis, which was at most $2.5\,\mathrm{N\,m}$. Examining test cases $9\,\mathrm{w}$ to 26 with applied force and moment along the z axis, the magnitude of the reported error for the F_z and M_z axes in table A.3 is at most $0.07\,\%$. In order to account for non-ideal experimental conditions such as vibration due to the operation of the motor or rotor, $0.1\,\%$ was chosen as a more conservative estimate of the actual measurement error likely to be observed during the experiments.

Case No.	F_x	F_y	F_z	M_x	M_y	M_z
1	0.000	200.170	0.000	-22.864	0.000	0.000
2	-200.170	0.000	0.000	0.000	-22.864	0.000
3	0.000	-200.170	0.000	22.864	0.000	0.000
4	200.170	0.000	0.000	0.000	22.864	0.000
5	0.000	289.134	0.000	-10.997	0.000	0.000
6	-289.134	0.000	0.000	0.000	-10.997	0.000
7	0.000	-289.134	0.000	10.997	0.000	0.000
8	289.134	0.000	0.000	0.000	10.997	0.000
9	0.000	173.481	0.000	-2.203	0.000	-19.829
10	0.000	173.481	0.000	-2.203	0.000	19.829
11	-173.481	0.000	0.000	0.000	-2.203	-19.832
12	-173.481	0.000	0.000	0.000	-2.203	19.840
13	0.000	-173.481	0.000	2.203	0.000	-19.829
14	0.000	-173.481	0.000	2.203	0.000	19.829
15	173.481	0.000	0.000	0.000	2.203	-19.840
16	173.481	0.000	0.000	0.000	2.203	19.832
17	0.000	0.000	266.893	-20.337	0.000	0.000
18	0.000	0.000	266.893	0.000	-20.337	0.000
19	0.000	0.000	266.893	20.337	0.000	0.000
20	0.000	0.000	266.893	0.000	20.337	0.000
21	0.000	0.000	889.644	0.000	0.000	0.000
22	0.000	0.000	-889.644	0.000	0.000	0.000
23	0.000	0.000	-266.893	20.337	0.000	0.000
24	0.000	0.000	-266.893	0.000	20.337	0.000
25	0.000	0.000	-266.893	-20.337	0.000	0.000
26	0.000	0.000	-266.893	0.000	-20.337	0.000

Table A.2. The calibration test matrix for the ATI Delta load cell used in this experimental study.

Case No.	F_x	F_y	F_z	M_x	M_y	M_z
1	0.00%	0.00%	0.06%	0.04%	0.11%	0.12%
2	0.07%	-0.04%	0.10%	0.00%	0.00%	0.03%
3	-0.03%	0.00%	0.08%	0.03%	0.10%	0.01%
4	0.11%	-0.03%	0.06%	-0.11%	-0.01%	0.03%
5	-0.06%	0.06%	0.08%	-0.05%	0.01%	0.05%
6	0.04%	0.00%	0.07%	-0.02%	-0.05%	0.11%
7	-0.07%	0.03%	0.08%	0.07%	0.02%	0.14%
8	0.06%	-0.03%	0.09%	-0.01%	0.03%	0.13%
9	-0.02%	-0.01%	0.04%	-0.02%	0.13%	0.02%
10	-0.02%	0.03%	0.04%	0.08%	-0.11%	0.02%
11	0.02%	-0.01%	0.03%	-0.12%	0.09%	0.01%
12	0.02%	-0.03%	0.02%	0.08%	0.03%	0.01%
13	-0.01%	0.04%	0.03%	-0.04%	-0.12%	0.00%
14	0.02%	0.04%	0.03%	-0.08%	0.15%	0.01%
15	-0.01%	0.00%	0.03%	0.17%	-0.01%	0.01%
16	-0.04%	-0.02%	0.03%	-0.10%	0.01%	0.00%
17	-0.04%	-0.01%	-0.02%	0.06%	-0.04%	-0.02%
18	0.09%	-0.02%	-0.03%	-0.03%	0.17%	-0.01%
19	-0.04%	-0.02%	0.00%	-0.03%	0.03%	0.04%
20	-0.04%	-0.05%	0.01%	0.01%	0.11%	0.07%
21	0.06%	-0.15%	0.02%	-0.05%	-0.39%	-0.04%
22	0.05%	-0.14%	-0.04%	-0.02%	-0.24%	-0.03%
23	0.00%	-0.03%	0.02%	0.03%	0.04%	0.01%
24	0.06%	-0.03%	0.04%	-0.01%	-0.17%	-0.02%
25	-0.03%	-0.04%	0.06%	-0.04%	0.10%	0.00%
26	-0.03%	-0.05%	0.04%	-0.08%	-0.20%	0.05%

Table A.3. Measurement error values for the ATI Delta load cell used in the experimental study, corresponding to the calibration test matrix in table A.2. Values are expressed as a percentage of the maximum rated load for the specific axis being referenced.

Appendix B
Rotor Models

For the sake of completeness and to facilitate the use of the results of this thesis in future studies, a detailed description of the rotor geometry will be provided in this appendix. This includes both the blade geometry and airfoil sections used, as well as the design of the rotor models used in the experiments. The author hopes that this information will be of use to future researchers who may seek to compare their own data to the results presented in chapter 4.
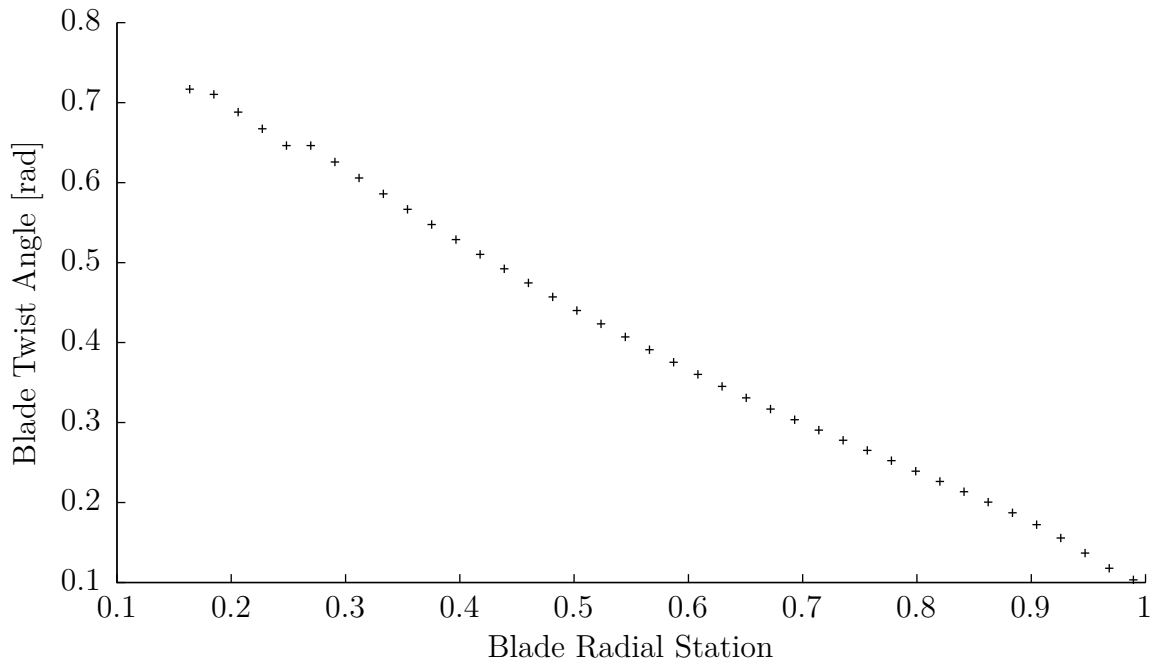
B.1 Rotor Blade Geometry

The airfoil sections vary along the blade span, maintaining a similar camber profile but changing in thickness. The section at the root has a thickness of approximately 23% of the chord length, while near the tip, the airfoil the geometry tapers to a thickness of 9% of the chord length. The chord length is also a function of the spanwise coordinate, and is plotted alongside the twist in Fig. B.1(a). Much of the outboard section of the blade is similar in thickness, with most of the variation taking place near the root of the blade. Selected airfoil sections are plotted in Fig. B.2 to provide a representative overview of the geometry.

Parameter	Value
Material	Stainless-Steel (17-4PH)
Radius	$0.18\,\mathrm{m}$
Max. chord	$2.04 \times 10^{-2}\,\mathrm{m}$
Number of blades	3
Twist angle	$35.15°$

Table B.1. Key parameters of the rotor model used for the high-pressure experiments.
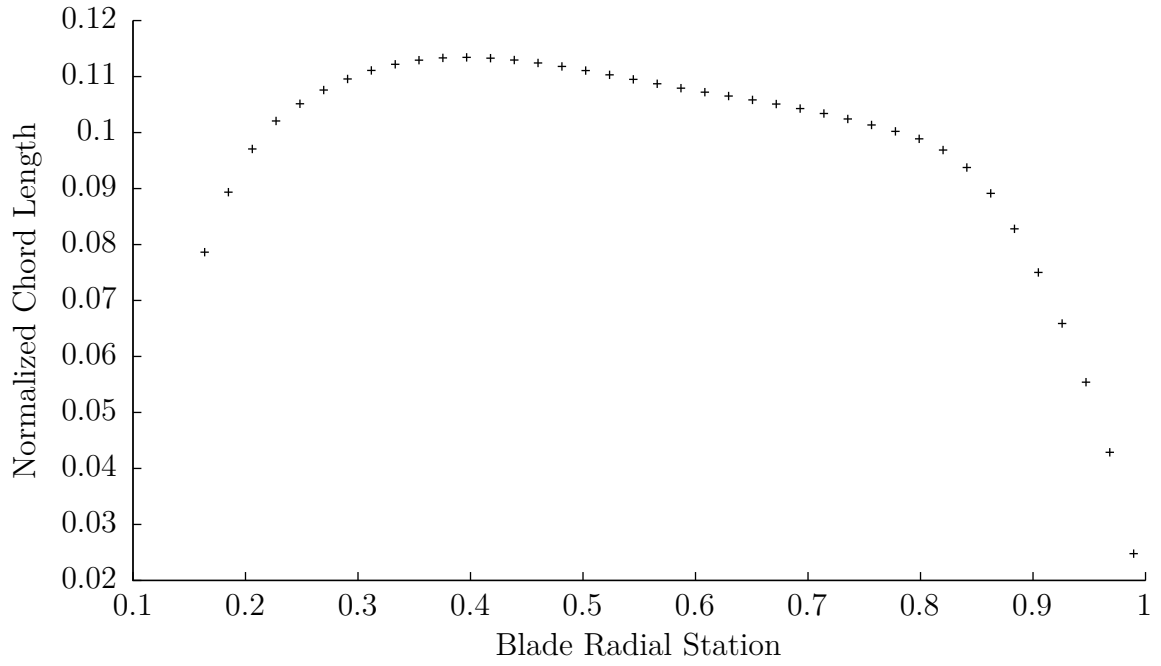
(a) Chord distribution along the blade span, normalized as a fraction of the rotor radius.

(b) Twist distribution along the blade span, expressed in radians.

Figure B.1. Geometric properties of the rotor blades including chord length (a) and twist (b) as a function of the radial station.
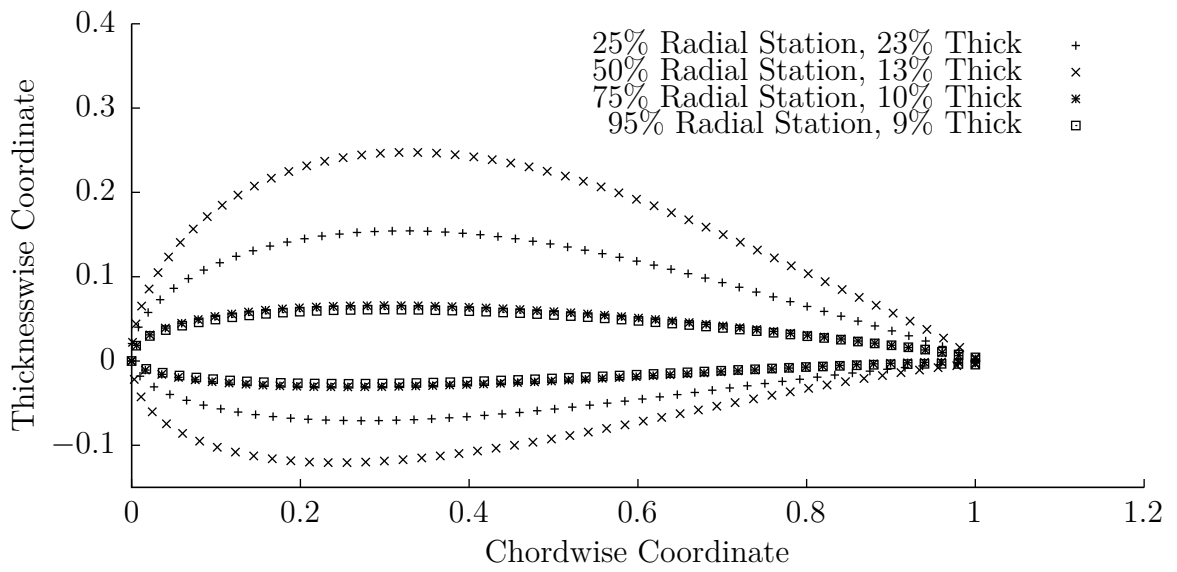
Figure B.2. Airfoil geometry at select radial stations along the blade, normalized to unit chord length.

B.2 Experimental Model Design

Two different rotor models were used in this study, a model consisting of 3D-printed blades mounted on a variable-pitch hub machined from aluminum, and a stainless-steel, fixed pitch rotor model. The 3D-printed rotor was used primarily for early exploration of the operating space of the rotor, and for comparison between several different facilities, while the stainless-steel rotor was used for the compressed-air experiments. Both rotors were based on the same blade design, and fabricated at the same scale to allow for direct comparison between the results. The design details of both of these rotors will be outlined here, and the differences in the two hub geometries will be highlighted.

The 3D-printed rotor blades were designed to interface with an existing variable-pitch hub which has been used for previous studies involving similarly sized rotors. The variable-pitch hub is modular, allowing for up to six blades to be attached through a number of removable blade-grips. The blade-grips interface with the hub through a series of threaded holes with a split on one end as shown in Fig. B.3. A screw is fed through the tab shown in the detail view in Fig. B.3, causing the hashed area to deform to clamp onto the threads of the blade grip. The friction due to the clamping force locks the pitch angle during operation.

The blades were 3D-printed using Rigid 10K resin, a proprietary formula produced by Formlabs. This material was chosen due to its improved stiffness and strength in comparison to alternative resin options. Each blade was printed as a single piece with a through-hole at the root, through which a pin would be driven to secure the blade to the blade-grip, allowing it to resist centrifugal loads. A steel bushing was press-fit into the hole to better distribute the centrifugal load over a larger area in order to avoid fracturing the plastic. A detailed drawing of the blade is shown in Fig. B.4. Given the rotor diameter of $0.36\,\mathrm{m}$ and the dimensions of the hub, the 3D printed blades were designed with a root-cutout of $56.92\,\mathrm{mm}$, or 32% of the rotor radius. In order to avoid stress concentrations due to the thin trailing edge or potential sharp corners at the root, the airfoil geometry was truncated at the root cutout location, and tapers to an elliptical cross section at the surface of the rectangular block which interfaces with the blade-grip. A fillet was also added to the elliptical edge at the mounting block.

The entire rotor assembly is shown in Fig. B.5, with the blades set to a collective pitch of 15°, as used in the experiments.

The rotor used for the compressed-air experiments was fabricated out of stainless-steel in order to withstand the greater loads due to the increased density of the air. In order
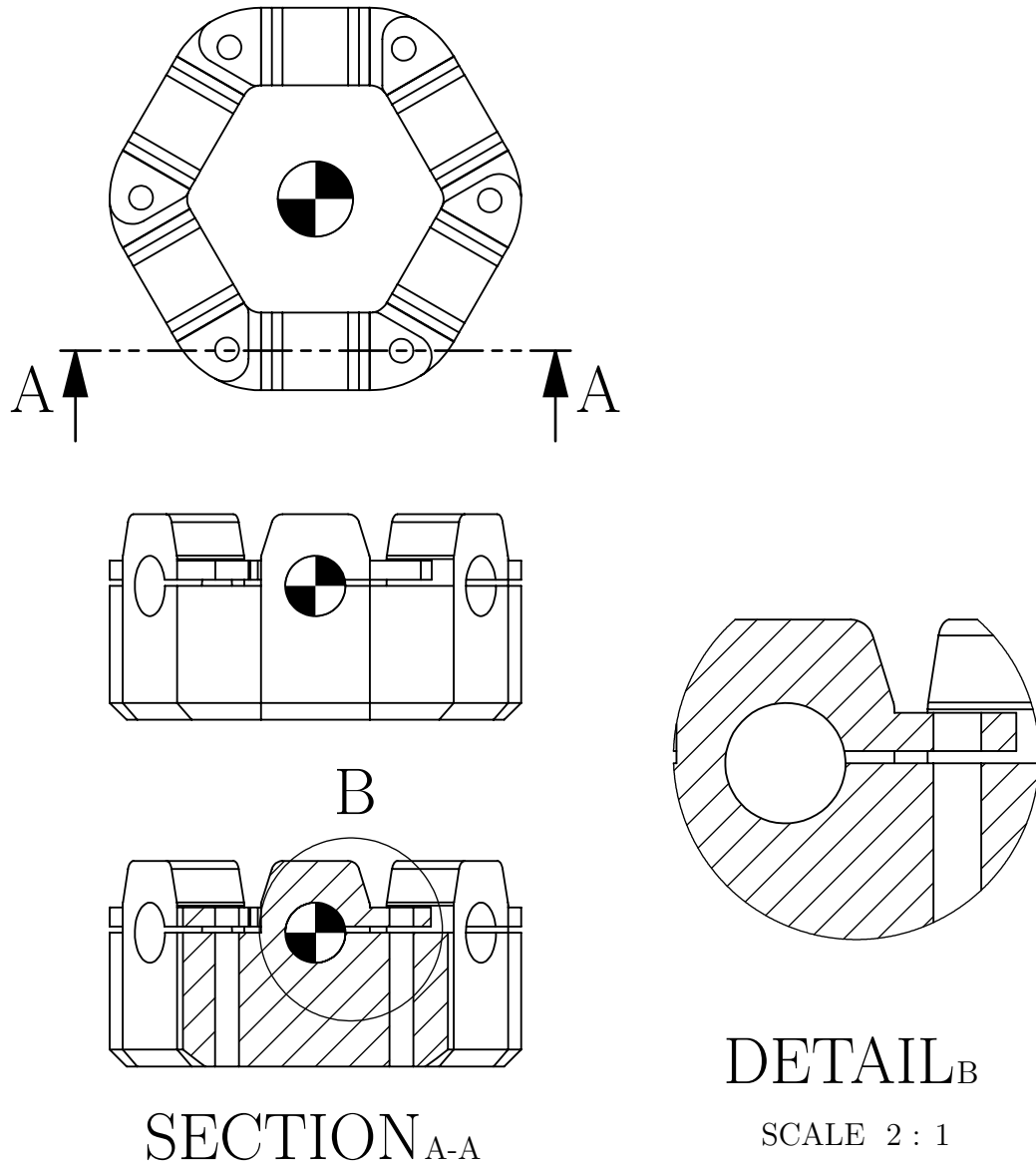
Figure B.3. CAD drawing of the variable-pitch rotor hub used with the 3D-printed blades, outlining the mechanism for pitch adjustment.

to simplify the design of the model and prevent failure due to the stresses at the blade root, the rotor was designed to be machined from a single piece of material. The blades therefore had to be set at a fixed pitch. The rotor was machined using a 5-axis CNC mill, allowing for the complex geometry to be accurately recreated to within a tolerance of $\pm\,0.08$ mm.

The hub was designed to attach to the motor through an adapter in order to improve compatibility with different motors which may be used in the future. The cost and complexity of designing and fabricating a new adapter would be far less than making an
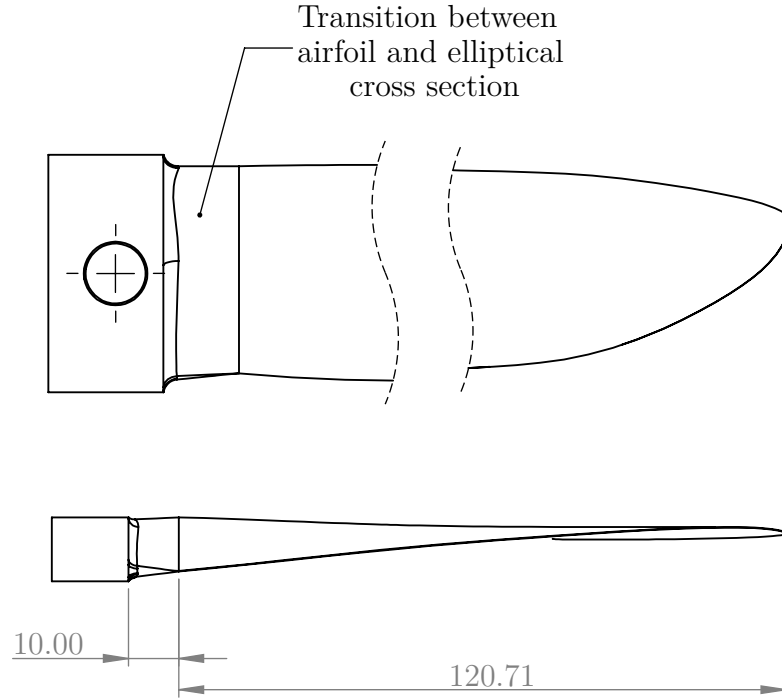
Figure B.4. CAD drawing of the 3D-printed rotor blade, highlighting the geometry at the blade root. All dimensions are in mm.

entirely new rotor with a mounting interface specific to a given motor. The two-piece hub assembly is shown in Fig. B.6. Due to the more simplified design, this hub could be made smaller than that used for the 3D-printed blades, and the blades consequently had a slightly smaller root-cutout of 41.22 mm, or 23% of the rotor radius. This allowed more of the original blade geometry to be replicated, which was desired for future comparisons with the full-scale rotor. Details of the full-scale rotor performance are not given in this study. The blade geometry is truncated at the root-cutout location and tapers to an elliptical cross section before intersecting with the hub, similar to the geometry of the 3D printed rotor shown in Fig. B.4. Since the stainless-steel rotor blades blend directly into the cylindrical hub rather than a rectangular block, the elliptical cross section is extruded outward from the hub in order to provide enough room for a suitable fillet before transitioning into the airfoil cross-section.

B.3 Airfoil Geometry

As mentioned previously, the airfoil section geometry varies along the blade. Airfoil geometry at discrete radial locations is shown in Fig. B.2 normalized to unit chord length.

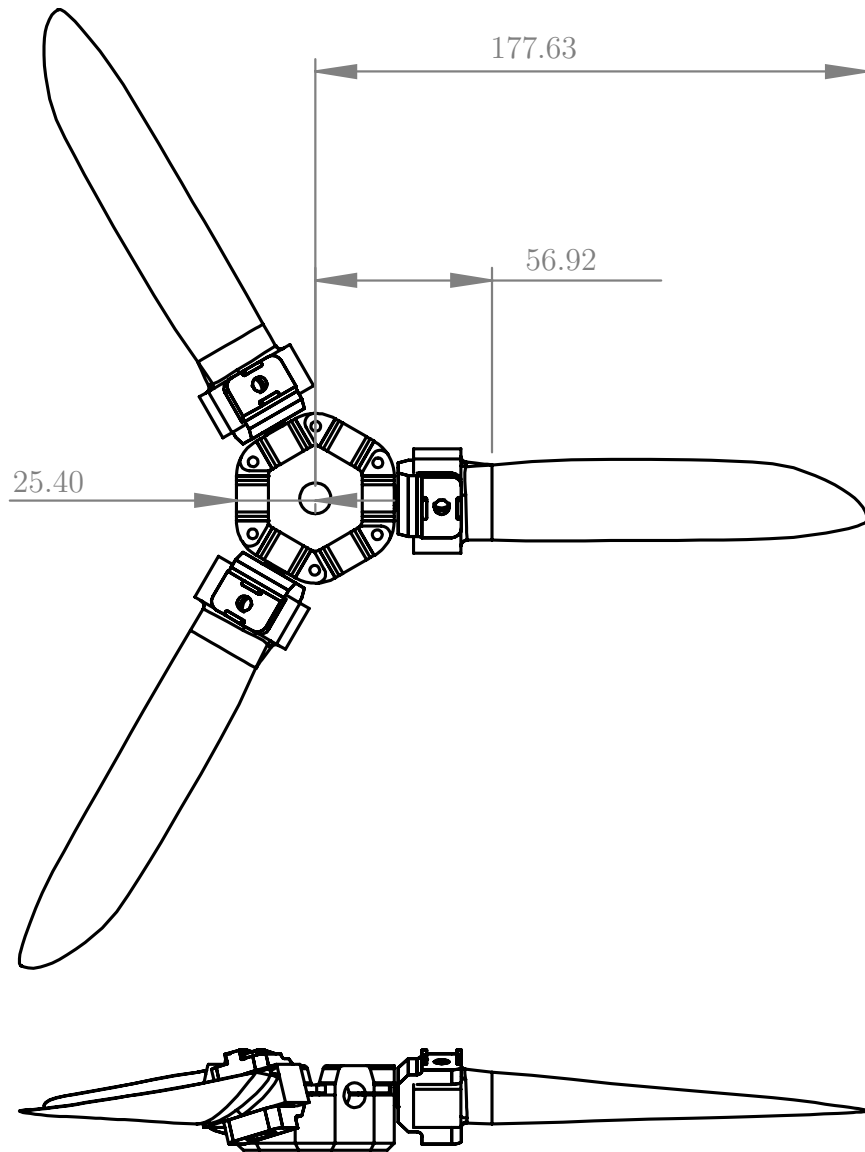**Figure B.5.** CAD drawing of the variable pitch rotor assembly showing axial and edgewise views, including the 3D-printed blades, and the aluminium blade grips and hub. All dimensions are in mm.
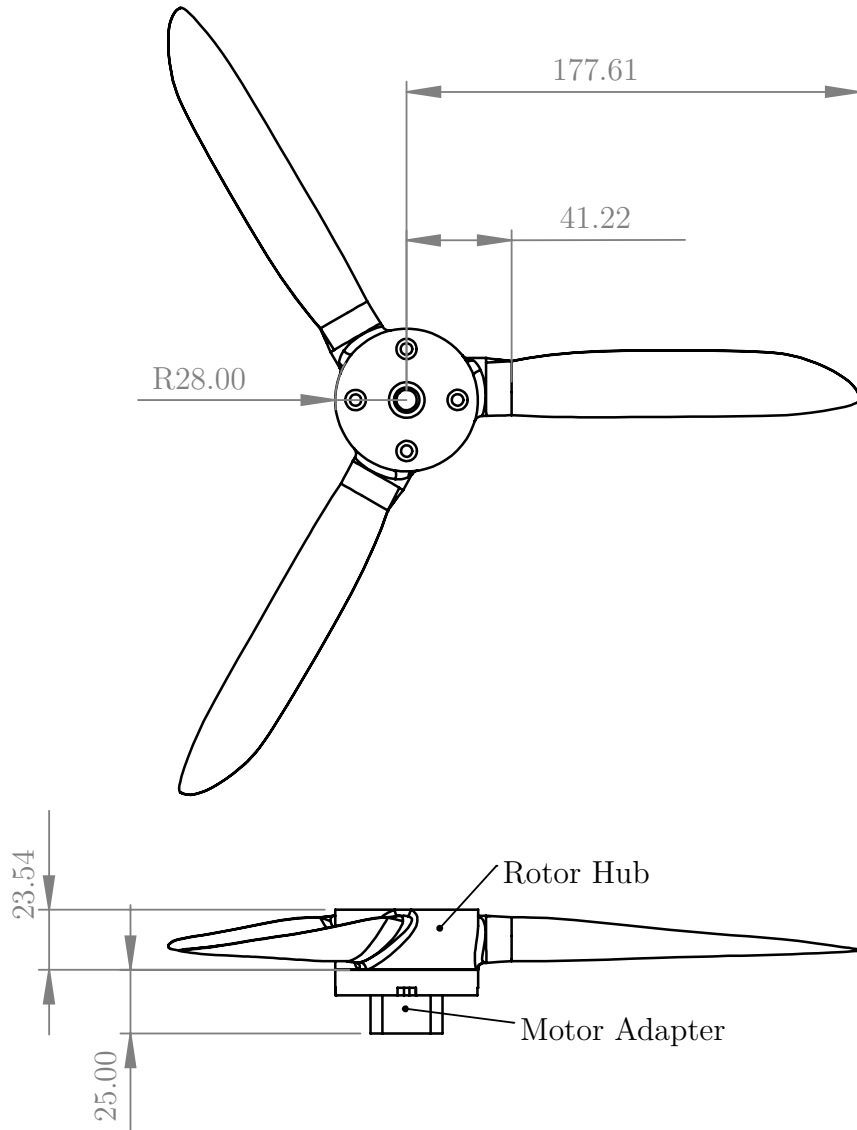
Figure B.6. CAD drawing of the stainless-steel rotor assembly showing axial and edgewise views, including the motor mounting adapter used for the compressed-air experiments. All dimensions are in mm.

Appendix C
Data Reduction and Post-Processing

This appendix will outline the methods used to analyze the experimental data, and produce the plots shown in chapter 4. The data was processed using GNU Octave [63].

C.1 Real Gas Relations

The density and the viscosity of the air were determined from measurements of the temperature and pressure, and an empirically derived virial model developed by Zagarola [57]. This model is a third order polynomial fit of the compressibility factor Z, in both temperature and pressure. The coefficients of this fit were calculated from a least-squares fit of data published in volume 2 of *Thermodynamic Functions of Gases* [64], which in turn was interpolated from data published in a paper by Michels et al. [65]. The resulting model is described by Eqn. C.1a.

$$Z = 1 + Z_1(p_a - 1) + Z_2(p_a - 1)^2 + Z_3(p_a - 1)^3 \tag{C.1a}$$

Where p_a is the absolute pressure in units of atmospheres, and the values of Z_i are defined in Eqn. C.1b.

$$
\begin{aligned}
Z_1 &= B_{1,1} + B_{2,1}T + B_{3,1}T^2 + B_{4,1}T^3 \\
Z_2 &= B_{1,2} + B_{2,2}T + B_{3,2}T^2 + B_{4,2}T^3 \\
Z_3 &= B_{1,3} + B_{2,3}T + B_{3,3}T^2 + B_{4,3}T^3
\end{aligned}
\tag{C.1b}
$$

Where T is the absolute temperature in units of Kelvin, and $B_{i,j}$ are the empirically

derived coefficients, whose values are listed in table C.1 [57].

	$B_{1,j}$ atm^{-n}	$B_{2,j}$ atm^{-n}K^{-1}	$B_{3,j}$ atm^{-n}K^{-2}	$B_{4,j}$ atm^{-n}K^{-3}
Z_1	-9.8378×10^{-3}	5.1986×10^{-5}	-7.0621×10^{-8}	0
Z_2	3.1753×10^{-5}	-1.7155×10^{-7}	2.4630×10^{-10}	0
Z_3	6.3764×10^{-7}	-6.4678×10^{-9}	2.1880×10^{-11}	-2.4691×10^{-14}

Table C.1. Empirical coefficients for the virial model of real gas compressibility. Units of each coefficient are described in terms of n, the subscript on Z in the corresponding equation, and row of the table.

C.2 Performance Coefficient Calculation and Interpolation

The plots of thrust and power coefficients shown in chapter 4 display data which was interpolated in Mach number from the experimental results. A suitable series of Mach numbers was chosen based on the uncertainty criteria discussed in § 2.4. The Mach number of each test point was calculated using the rotational speed measurements. The thrust and power coefficients were calculated using Eqn. 2.6 and Eqn. 2.7 respectively. This produced a different set of discrete thrust and power coefficient measurements as a function of Mach number for each ambient pressure condition. These datasets were then linearly interpolated to obtain thrust and power coefficients at the same set of Mach numbers for each ambient pressure. The result is a set of data for which the Mach number can more directly be used as an independent variable, allowing for potential trends in performance with varying Mach number to be observed.

Estimates of the uncertainty of the thrust and power coefficients were calculated for each measurement point based on the sensitivity coefficients in table 2.4. The uncertainty values were then interpolated in Mach number using the same linear scheme described for the performance coefficients.

Bibliography

[1] SINGLETON, J. D. and YEAGER JR., W. T. (2000) "Important Scaling Parameters for Testing Model-Scale Helicopter Rotors," *Journal of Aircraft*, **37**(3), pp. 396–402.

[2] SPLETTSTOESSER, W. R., KUBE, R., WAGNER, W., SEELHORST, U., BOUTIER, A., MICHELIL, F., MERCKER, E., and PENGEL, K. (1997) "Key Results From a Higher Harmonic Control Aeroacoustic Rotor Test (HART)," *Journal of the American Helicopter Society*, **42**(1), pp. 58–78.

[3] VAN DER WALL, B. G., BURLEY, C. L., YU, Y., RICHARD, H., PENGEL, K., and BEAUMIER, P. (2004) "The HART II Test - Measurement of Helicopter Rotor Wakes," *Aerospace Science and Technology*, **8**, pp. 273–284.

[4] YAMAUCHI, G. K. and JOHNSON, W. (1983) *Trends of Reynolds Number Effects on Two-Dimensional Airfoil Characteristics for Helicopter Rotor Analyses*, *Tech. Rep. NASA Technical Memorandum 84363*, NASA Ames Research center, Moffett Field, California.

[5] YEAGER JR., W. T. and MANTAY, W. R. (1976) *Correlation of Full-Scale Helicopter Rotor Performance in Air With Model Scale Freon Data*, *Tech. rep.*, NASA Langley Research Center.

[6] VON DOENHOFF, A. E., BRASLOW, A. L., and SCHWARTZBERG, M. A. (1953) *Studies of the Use of Freon-12 as a Wind-Tunnel Testing Medium*, *Tech. Rep. NACA Technical Note 3000*, National Advisory Committee for Aeronautics.

[7] LEISHMAN, J. G. and JOHNSON, B. (2008) "Engineering Analysis of the 1907 Cornu Helicopter," in *64th Annual Forum of the American Helicoper Society*.

[8] CLARKE, A. E. and S, B. A. R. (1968) "Selected Aspects of the Aerodynamics of Rotorcraft," *The Aeronautical Journal*, **72**, pp. 178–186.

[9] STEPNIEWSKI, W. Z. and KEYS, C. N. (1984) *Rotary-Wing Aerodynamics: Two Volumes Bound as One*, Dover Publications, Inc.

[10] LEISHMAN, J. G. (2016) *Principles of Helicopter Aerodynamics*, 2 ed., Cambridge University Press.

[11] FROUDE, W. (1878) "On the Elementary Relation Between Pitch, Slip, and Propulsive Efficiency," *Transaction of the Institute of Naval Architects*, **19**, pp. 22–33.

[12] MANGLER, K. W. and SQUIRE, H. B. (1950) *The Induced Velocity Field of a Rotor*, *Tech. Rep. Reports and Memoranda No. 2642*, Aeronautical Research Council.

[13] CONLISK, A. T. (1997) "Modern Helicopter Aerodynamics," *Annual Review of Fluid Mechanics*, **29**, pp. 515–567.

[14] BOYNE, W. J. and LOPEZ, D. S. (1984) *Vertical Flight: The Age of the Helicopter*, Smithsonian Institution Press.

[15] KADHIRESAN, A. R. and DUFFY, M. J. (2019) "Conceptual Design and Mission Analysis for eVTOL Urban Air Mobility Flight Vehicle Configurations," in *AIAA AVIATION Forum*, AIAA.

[16] GARROW, L. A., GERMAN, B. J., and LEONARD, C. E. (2021) "Urban Air Mobility: A Comprehensive Review and Comparative Analysis With Autonomous and Electric Ground Transportation for Informing Future Research," *Transportation Research Part C: Emerging Technologies*, **132**.
URL https://www.sciencedirect.com/science/article/pii/S0968090X21003788

[17] SILVA, C. and JOHNSON, W. (2018) "VTOL Urban Air Mobility Concept Vehicles for Technology Development," in *AIAA AVIATION Forum*, AIAA.

[18] JOHNSON, W., SILVA, C., and SOLIS, E. (2018) "Concept Vehicles for VTOL Air Taxi Operations," in *American Helicopter Society Technical Conference on Aeromechanics Design for Transformative Vertical Flight*, American Helicopter Society.

[19] JOHNSON, W. and SILVA, C. (2021) "NASA Concept Vehicles and the Engineering of Advanced Air Mobility Aircraft," *The Aeronautical Journal*, **126**(1295), pp. 59–91.

[20] KOSTEK, A. A., BRAUKMANN, J. N., LÖSSLE, F., MIENSER, S., VISINGARDI, A., BOISARD, R., RIZIOTIS, V., KESSLER, M., and GARDNER, A. D. (2023) "Experimental Investigation of Quadrotor Aerodynamics with Computational Cross-Validation," in *Vertical Flight Society's 79th Annual Forum & Technology Display*, Vertical Flight Society.

[21] HEALY, R. and GANDHI, F. (2023) "A Computational Investigation of Canted Side-by-Side Rotors in Ground Effect," in *Vertical Flight Society's 79th Annual Forum & Technology Display*, Vertical Flight Society.

[22] SILVA, M., HROMISIN, S., CORBETT, M., GRAYBEAL, N., CATO, S., RALSTON, J., PREVOST, R., and GRAY, C. (2023) "Model-Scale Investigation of Tiltrotor Low-Speed Obstacle-Induced Downwash Recirculation," in *Vertical Flight Society's 79th Annual Form & Technology Display*, Vertical Flight Society.

[23] BROWN, G. E. and AHUJA, V. (2023) "The Stopped Rotor Concept - A New Look at an Old Idea," in *Vertical Flight Society's 79th Annual Forum & Technology Display*, Vertical Flight Society.

[24] NORTH, D. D., BUSAN, R. C., and HOWLAND, G. (2021) "Design and Fabrication of the LA-8 Distributed Electric Propulsion VTOL Testbed," in *AIAA SciTech Forum*, AIAA.

[25] JACKLIN, S. A., HABER, A., DE SIMONE, G., NORMAN, T. R., KITAPLIOGLU, C., and SHINODA, P. (2002) "Full-Scale Wind Tunnel Test of an Individual Blade Control System for a UH-60 Helicopter," in *American Helicopter Society 58th Annual Forum*.

[26] KEYS, C. N., MCVEIGH, M. A., DADONE, L., and MCHUGH, F. J. (1985) "Estimation of Full-Scale Rotor Performance From Model Rotor Test Data," *Journal of the American Helicopter Society*, **30**(4), pp. 22–29.

[27] JEPSON, D., MOFFITT, R., HILZINGER, H., and BISSEL, J. (1983) *Analysis and Correlation of Test Data From an Advanced Technology Rotor System, Tech. Rep. NASA CR 3714*, NASA.

[28] KINDLER, K., GOLDHAHN, E., LEOPOLD, F., and RAFFEL, M. (2007) "Recent Developments in Background Oriented Schlieren Methods for Rotor Blade Tip Vortex Measurements," *Experiments in Fluids*, pp. 233–240.

[29] BRAUKMANN, J. N., SCHWARZ, C., WOLF, C. C., BURON, E., KOCH, S., BUSKE, G., and GARDNER, A. D. (2023) "BOS and Hot-Film Analysis of a CH-53G Helicopter Wake in Ground Effect," in *Vertical Flight Society's 79th Annual Forum & Technology Display*.

[30] RAFFEL, M., HEINECK, J. T., SCHAIRER, E., LEOPOLD, F., and KINDLER, K. (2014) "Background-Oriented Schlieren Imaging for Full-Scale and In-Flight Testing," *Journal of the American Helicopter Society*, (1), pp. 1–9.

[31] SCHWARZ, C., BAUKNECHT, A., WOLF, C. C., COYLE, A., and RAFFEL, M. (2020) "Full-Scale Rotor-Wake Investigation of a Free-Flying Helicopter in Ground Effect Using BOS and PIV," *Journal of the American Helicopter Society*, (3), pp. 1–20.

[32] BRAUKMANN, J. N., WOLF, C. C., GOERTTLER, A., and RAFFEL, M. (2019) "Blade Tip Vortex Characterization of a Rotor under Cyclic Pitch Conditions Using BOS and PIV," in *AIAA SciTech 2019 Forum*.

[33] DETERS, R. W., ANANDA, G. K., and SELIG, M. S. (2014) "Reynolds Number Effects on the Performance of Small-Scale Propellers," in *AIAA AVIATION Forum*, AIAA.

[34] BOYD, D. D., JR, BURLEY, C. L., and CONNER, D. A. (2004) "Full Scale Rotor Aeroacoustic Predictions and the Link to Model Scale Rotor Data," in *American Helicopter Society 4th Decennial Specialists' Conference on Aeromechanics*, American Helicopter Society.

[35] CARADONNA, F. X. and C, T. (1981) *Experimental and Analytical Studies of a Model Helicopter Rotor in Hover*, Tech. Rep. NASA-TM-81232, NASA.

[36] SCHWARZ, C., BAUKNECHT, A., MAILÄNDER, S., and RAFFEL, M. (2019) "Wake Characterization of a Free-Flying Model Helicopter in Ground Effect," *Journal of the American Helicopter Society*, (1), pp. 1–16.

[37] LANDGREBE, A. J. (1972) "The Wake Geometry of a Hovering Helicopter Rotor and Its Influence on Rotor Performance," in *28th Annual National Forum of the American Helicopter Society*, American Helicopter Society.

[38] BOXWELL, D. A., SCHMITZ, F. H., SPLETTSTOESSER, W. R., and SCHULTZ, K. J. (1987) "Helicopter Model Rotor-Blade Vortex Interaction Impulsive Noise: Scalability and Parametric Variations," *Journal of the American Helicopter Society*.

[39] HARRIS, F. D. (2020) *Model Rotor Hover Performance at Low Reynolds Number*, Tech. Rep. NASA CR 20205001147, NASA Ames Research Center.

[40] SCHLICHTING, H. and TRUCKENBRODT, E. (1979) *Aerodynamics of the Airplane*, McGraw-Hill International Book Company.

[41] HUBER, P. T. (1946) *Use of Freon-12 as a Fluid for Aerodynamic Testing*, Tech. Rep. NACA Technical Note No. 1024, National Advisory Committee for Aeronautics.

[42] ZUCKERWAR, A. J. (2002) *Handbook of the Speed of Sound in Real Gases: Speed of Sound in Air*, vol. 3, Academic Press.

[43] KITAPLIOGLU, C. (1990) *Analysis of Small-Scale Rotor Hover Performance Data*, Tech. Rep. NASA Technical Memorandum 102271, NASA Ames Research Center, Moffett Field, California.

[44] SCHLICHTING, H. and GERSTEN, K. (2017) *Boundary Layer Theory*, 9 ed., Springer-Verlag Berlin Heidelberg.

[45] THOMAS, F. (1999) *Fundamentals of Sailplane Design: Grundlagen für den Entwurf von Segelflugzeugen*, 3 ed., College Park Press, College Park, Maryland 20741, USA.

[46] ABBOT, I. H. and VON DOENHOFF, A. E. (1959) *Theory of Wing Sections: Including a Summary of Airfoil Data*, Dover Publications, Inc.

[47] DINI, P. and MAUGHMER, M. D. (1994) "Locally Interactive Laminar Separation Bubble Model," *Journal of aircraft*, **31**(4), pp. 802–810.

[48] O'MEARA, M. and MUELLER, T. J. (1987) "Laminar Separation Bubble Characteristics on an Airfoil at Low Reynolds Numbers," *AIAA journal*, **25**(8), pp. 1033–1041.

[49] WARD, J. W. (1963) "The Behavior and Effects of Laminar Separation Bubbles on Aerofoils in Incompressible Flow," *Journal of the Royal Aeronautical Society*, **67**, pp. 783–790.

[50] GASTER, M. (1967) *The Structure and Behavior of Laminar Separation Bubbles*, Tech. Rep. Reports and Memoranda No. 3595, National Physical Laboratory.

[51] SCHMIDT, G. S. and MUELLER, T. J. (1989) "Analysis of Low Reynolds Number Separation Bubbles Using Semiempirical Methods," *AIAA journal*, **27**(8), pp. 993–1001.

[52] GLAUERT, H. (1947) *The Elements of Aerofoil and Airscrew Theory*, 2 ed., Cambridge University Press.

[53] MUSE, T. C. (1943) *Some Effects of Reynolds and Mach Numbers on the Lift of an NACA 0012 Rectangular Wing in the NACA 19-Foot Pressure Tunnel*, Tech. Rep. CB No. 3E29, National Advisory Committee for Aeronautics, Langley Field, Virginia.

[54] SPREITER, J. R. and STEFFEN, P. J. (1946) *Effect of Mach and Reynolds Numbers on Maximum Lift Coefficient*, Tech. Rep. NACA Technical Note No. 1044, National Advisory Committee for Aeronautics.

[55] RACISZ, S. F. (1952) *Effects of Independent Variations of Mach Number and Reynolds Number on the Maximum Lift Coefficients of Four NACA 6-Series Airfoil Sections*, Tech. Rep. NACA Technical Note No. 2824, National Advisory Committee for Aeronautics.

[56] MILLER, M. A., KIEFER, J., WESTERGAARD, C., HANSEN, M. O. L., and HULTMARK, M. (2019) "Horizontal Axis Wind Turbine Testing at High Reynolds Numbers," *Phys. Rev. Fluids*, **4**.

[57] ZAGAROLA, M. V. (1996) *Mean-Flow Scaling of Turbulent Pipe Flow*, Ph.D. thesis, Princeton University.

[58] ZAHIRUDIN, R. A. R., GREENWOOD, E., WEITSMAN, D., and PALACIOS, J. (2021) "The Development of a Coaxial Acoustics Test System for Rotor Noise," *Vertical Flight Society Forum*.

[59] (2022) "IEC 60751: Industrial Platinum Resistance Thermometers and Platinum Temperature Sensors," *International Electromechanical Commission*.

[60] FIGLIOLA, R. S. and BEASLEY, D. E. (1991) *Theory and Design for Mechanical Measurements*, John Wiley & Sons, Inc.

[61] Russel, J. M. (1979) "Length and Bursting of Separation Bubbles: A Physical Interpretation," in *Science and Technology of Low Speed and Motorless Flight, Part 1*, NASA.

[62] van Ingen, J. L. (2008) "The e^N Method for Transition Prediction. Historical Review of Work at TU Delft," in *38th Fluid Dynamics Conference and Exhibit*, American Institute of Aeronautics and Astronautics.

[63] Eaton, J. W., Bateman, D., Hauberg, S., and Wehbring, R. (2022) *GNU Octave Version 7.3.0 Manual: A High-Level Interactive Language for Numerical Computations.*
URL https://www.gnu.org/software/octave/doc/v7.3.0/

[64] Din, F. (1956) *Thermodynamic Functions of Gases*, vol. 2, Butterworths, London.

[65] Michels, A., Wassenaar, T., and van Seventer, W. (1953) "Isotherms of Air Between 0 °C and 75 °C and at Pressures up to 2200 atm," *Applied Scientific Research, Section A*, **4**, pp. 52–56.